UNIVERSITA' DEGLI STUDI DI CAGLIARI

FACOLTA' DI INGEGNERIA

DIPARTIMENTO DI INGEGNERIA ELETTRICA ED ELETTRONICA

Correlation between interface-dependent properties and electrical performances in OFETs

Ing. Piero Cosseddu

Tesi per il conseguimento del Dottorato di Ricerca

In Ingegneria Elettronica ed Informatica

Relatore: Prof. Annalisa Bonfiglio

Corso di Dottorato di Ricerca in Ingegneria Elettronica ed Informatica

XIX Ciclo

Outline of the thesis

The interest for Organic Electronics has dramatically increased over these past years, not only in academic research, but also in an industrial perspective. The main reasons for focused interest in the field of "plastic electronics" is the opportunity to produce low cost devices on plastic substrates on large areas, opening, indeed, an entire new market segment. One of the fundamental points in determining the electrical performances in organic devices is that, even though they are usually thought as macroscopic devices, their behaviour is strongly driven by interfacial phenomena taking place in the nano scale.

The focus of this thesis is the realization and characterization of Organic Field effect Transistors (OFETs) with a particular interest for investigating the influence of the interfaces on the electrical performances of the devices. Indeed, the parameters which mostly influence the electrical behaviour can be divided into to groups:

i) Intrinsic parameters of the material, as molecular packing and island nucleation, where the interfacial phenomena are taking place in the inter-molecular and inter-island scale.
ii) Structural properties of the device, where the role of the triple interface metal electrode/organic semiconductor/gate dielectric can, in fact, significantly dictate the electrical behaviour of the device.

The first chapter is basically an introduction to organic materials and to the basis of charge transport in organics. The last part of the chapter is focussed on the description of the material employed in this thesis.
The second chapter gives a detailed description of the Organic Field Effect Transistor. It is divided into three sections. The first is dedicated to the introduction of the models generally used for describing OFETs

behaviour; in the second we show the architectures usually employed at the state of the art for OFETs assembly; whereas the last part of the chapter is dedicated to the description of the fabrication technologies we used during this thesis activity.

In the third chapter we introduce the characterization techniques employed in this thesis for investigating the structural and morphological properties of the materials we used and for the electrical characterization of the assembled devices.

The last four chapters are more focussed on the main results obtained in different dedicated experiments.

Chapter four is dedicated to the investigation of FETs; here we show a detailed comparison between Bottom Contact and Top Contact devices, focussing in particular on the role played by the interfaces in their electrical behaviour.

In chapter five and six we show two examples in which the modulation and engineering of interfaces in organic bulk heterojunctions can dramatically influence the electrical performances of the devices. In particular in chapter five it will be shown the first example reported (as far as we know) of all-organic ambipolar FETs realized by means of double layer organic heterojunctions. In chapter 6 we have analysed the behaviour of devices obtained from bulk heterojunctions of two similar materials that differs only for a side alkyl susbstituent. Again, the interface between these materials plays a key role in determining the device performances.

In the last chapter we introduce the structure of the Organic Light Emitting Transistor and we show that, changing the electrode/semiconductor interface by employing a new technology for the patterning of the electrodes, it is possible to dramatically improve the optoelectronic performances of the assembled devices.

A final short chapter is dedicated to conclusions.

Sommario

L'interesse nei confronti dell'Elettronica Organica è enormemente cresciuto negli ultimi anni sia a livello di ricerca accademica che industriale. Il vantaggio dell'elettronica organica sta nella possibilità di realizzare dispositivi su film sottili e flessibili, su larga area e a bassi costi di realizzazione e produzione, sfruttando quelle che sono le caratteristiche chimiche e meccaniche dei materiali utilizzati, oligomeri e polimeri organici coniugati. Uno degli aspetti fondamentali nel determinare le prestazioni elettriche nei dispositivi organici è che, nonostante essi siano generalmente pensati come dei dispositivi macroscopici, il loro comportamento è fortemente dettato da fenomeni di interfaccia che hanno luogo a livello nanoscopico.

In questa tesi ci si è occupati prevalentemente della realizzazione e caratterizzazione di transistor organici ad effetto di campo (OFETs) focalizzandosi in modo particolare sull'influenza delle interfacce nelle prestazioni elettriche dei dispositivi realizzati. I parametri che possono incidere sulle performance elettriche possono, infatti, essere molteplici e fondamentalmente possono essere racchiusi in due grandi categorie:

i) Parametri intrinseci del materiale, come la struttura molecolare e il meccanismo di crescita del film, in cui i fenomeni di interfaccia che hanno più peso sono a livello intermolecolare.
ii) Parametri intrinseci del dispositivo, in cui il ruolo della tripla interfaccia metallo/semiconduttore organico/dielettrico di gate può, in effetti, determinare in maniera significativa il comportamento elettrico del dispositivo.

Il primo Capitolo è fondamentalmente un'introduzione ai materiali organici e alle basi del meccanismo di trasporto di carica in questo tipo di materiali. L'ultima parte del capitolo è incentrata sulla descrizione dei materiali utilizzati durante questo lavoro di tesi.

Il secondo capitolo offre una descrizione dettagliata dei transistor organici ad effetto di campo (OFETs). È diviso in tre parti. La prima è dedicata alla trattazione dei modelli tipicamente utilizzati per descrivere il comportamento degli OFETs; nella seconda parte verranno introdotte le architetture più comunemente utilizzate allo stato dell'arte; mentre nell'ultima parte si darà una descrizione delle tecniche di fabbricazione utilizzate durante questa tesi.

Nel terzo capitolo saranno introdotte le tecniche di caratterizzazione utilizzate in questa tesi per l'analisi strutturale e morfologica dei materiali e per la caratterizzazione elettrica dei dispositivi realizzati.

Gli ultimi quattro capitoli verranno descritti i risultati ottenuti in diversi esperimenti dedicati.

Il quarto capitolo è dedicato allo studio delle caratteristiche elettriche di OFETs completamente organici; qui faremo un confronto approfondito tra dispositivi realizzati in configurazione Bottom Contact e Top Contact, focalizzandosi in particolare sul ruolo delle interfacce nel determinare il comportamento e le prestazioni elettriche dei dispositivi.

Nei capitoli cinque e sei mostreremo due esempi in cui l'ingegnerizzazione delle interfacce tramite l'uso di heterogiunzioni può influenzare notevolmente le prestazioni elettriche dei dispositivi. In particolare, nel capitolo cinque verrà mostrato il primo esempio (a nostra conoscenza) di OFET interamente organico e ambipolare, realizzato utilizzando una heterogiunzione a doppio strato. Nel capitolo 6 abbiamo invece analizzato il comportamento di dispositivi ottenuti tramite heterogiunzioni tra due materiali che differiscono tra loro solo per la presenza in uno di essi di catene alchiliche come sostituenti terminali della molecola. Ancora una volta, l'interfaccia tra i due

materiali gioca un ruolo fondamentale nel determinare le prestazioni elettriche del dispositivo.

Nell'ultimo capitolo introdurremo il transistor organico ad emissione di luce (OLETs) e mostreremo come, modificando l'interfaccia metallo/semiconduttore tramite l'uso di una nuova tecnica per il patterning degli elettrodi, sia possibile incrementare significativamente le prestazioni opto-elettroniche dei dispositivi realizzati.

Un ultimo, breve, capitolo finale è dedicato alle conclusioni.

Acknowledgements

First of all I would like to thank my supervisor Prof. Annalisa Bonfiglio for having given me the opportunity to work in her group over these last years. She supervised my activity showing continuous interest in my work, encouraging me with her great patience and her brilliant and fruitful advices. I would like to acknowledge all my colleagues (randomly ordered!), Ileana Manunza, Emanuele Orgiu, Ruggero Pintus, Andrea Morelli, Maurizio Maccioni and Simone Locci for their daily support, and for keeping me company during my uncountable coffee breaks!! A special thank also to Sandro Tedde, and to "The Judge" Mauro Morana. A big hallo to Ornella, you left us too early!

I'm very grateful to Dr. Norbert Koch for having given me the opportunity of joining his group at Humboldt University in Berlin and his support to my activity with fruitful advices and discussions. A very big thank to all the members of the group, in particular to Ingo Salzmann and to Oliver Vogel who had a very important role in this thesis, dealing with the preparation and structural characterization of bulk heterojunction thin films.

I'm also very grateful to Dr. Beatrice Fraboni and Riccardo di Pietro at the University of Bologna, who performed all the PCS measurements that have been very important for this thesis. To Dr. Betty Casu at Tubingen University for the help she gave me in the XPS and NEXAFS characterizations, and, not less important, in the evaluation of the recorded data.

I want to acknowledge Clara Santato and Fabio Cicoira and Dr. Michele Muccini for the very fruitful collaboration in the field of tetracene based OLETs.

A very big thank to all the guys who have been close to me in Berlin, in particular to Rolf Kniprath, and also my very big Turkish friends Kemal

Azun, Cagri Gozen and Ekin Alkan, I will never ever forget what they did for me!!

I would like to thank my parents, without whom I would have never been able to arrive where I am today!!!

And finally, an infinite thank to Laura, for all the love, support and understanding that you have been giving me over these years.

Papers included in this thesis:

An Organic Thin Film Transistor structure for optoelectronic applications

P. Cosseddu, F. Mameli, I. Manunza, O. Sanna, and A. Bonfiglio

Proc. SPIE Photonics Europe, "Organic Optoelctronics and Photonics", edited by P. Heremans, M. Muccini, H. Hofstraat, vol. CDS 122-5464, 74 (2004).

Author's contribution to the paper: AFM morphological characterization.

Tetracene light-emitting transistors on flexible plastic substrates

C. Santato, I. Manunza, A. Bonfiglio, F. Cicoira, P. Cosseddu, R. Zamboni, M. Muccini

Appl. Phys. Lett. 86, 141106 (2005)

Author's contribution to the paper: AFM morphological characterization.

Organic light-emitting transistors using concentric source/drain electrodes on a molecular adhesion layer

C. Santato, F. Cicoira, P. Cosseddu, A. Bonfiglio, P. Bellutti, M. Muccini, R. Zamboni, F. Rosei, A. Mantoux and P. Doppelt

Appl. Phys. Lett. 88, 163511 (2006)

Author's contribution to the paper: Some writings and all the AFM morphological characterization.

Soft Lithography Fabrication of All Organic Bottom contact and Top Contact Field Effect Transistors

P. Cosseddu and A. Bonfiglio

Appl. Phys. Lett. 88, 023506 (2006).

Author's contribution to the paper: Major part of the experimental work and some writing.

A comparison between Bottom Contact and Top Contact all organic FETs assembled by soft lithography

P. Cosseddu, A. Bonfiglio

Accepted for publication in Thin Solid Films

Author's contribution to the paper: Major part of the experimental work and of the writing.

Towards the textile transistor: Assembly and characterization of an organic field effect transistor with a cylindrical geometry

M. Maccioni, E. Orgiu, P. Cosseddu, S. Locci and A. Bonfiglio

Appl. Phys. Lett. 89, 143515 (2006).

Author's contribution to the paper: Some part of the experimental work and all the AFM morphological characterization.

A high-resolution NEXAFS investigation of the molecular orientation in the pentacene/PEDOT:PSS system

M. B. Casu, P. Cosseddu, D. Batchelor, A. Bonfiglio, and E. Umbach

To be submitted

Author's contribution to the paper: Major part of the experimental work and some writing.

Soft Lithography Fabrication of Fully Flexible and Transparent all Organic FETs for Large Area Applications

P. Cosseddu, E. Orgiu and A. Bonfiglio

Mater. Res. Soc. Symp. Proc. Vol. 965 © 2007 Materials Research Society, 0965-S07-02

Author's contribution to the paper: Major part of the experimental work and of the writing.

Ambipolar transport in all-organic heterojunction field effect transistors

P. Cosseddu, and A. Bonfiglio, I. Salzmann, J. P. Rabe and N. Koch

To be submitted

Author's contribution to the paper: Major part of the experimental work and of the writing.

Tuning the electrical properties in OFETs by means of organic bulk heterojunctions

P.Cosseddu, A. Bonfiglio, J. O. Vogel, I. Salzmann, R. Di Pietro, B. Fraboni, A. Cavallini, J. P. Rabe and N. Koch

Manuscript in preparation

Author's contribution to the paper: Major part of the experimental work and of the writing.

Table of contents

Chapter 1

Organic Materials

In the late 70's (1977) a group of researchers, Heeger, MacDiarmid, and Shirakawa [1] discovered the conducting properties of polymers. They demonstrated that it is possible to obtain a conducting polymer by doping polyacetylene with arsenic pentafluoride (AsF_5). This discovery, which earned them the Nobel Prize in chemistry, paved the way for the new field of Organic Electronics. Intrinsic conducting and semiconducting plastic materials, either electrons (n-type) or holes (p-type) transport with band like structure, can now be made. The main advantages of employing this new generation of materials for electronics applications lie in the possibility of being processed with very easy and low cost techniques. Indeed, organic materials, either oligomers or polymers, can be deposited by various methods such as thermal evaporation in vacuum, molecular beam deposition, spin coating, and patterned with very low cost techniques as photolithography, screen printing, inkjet printing and soft lithography suitable for mass production over a very large scale of Plastic Electronics devices [2-9]. Moreover, due to their intrinsic mechanical properties they opened the way for unusual applications. In fact, organic semiconductors, being plastic materials, are very flexible; they can be easily deposited on unusual substrates such as paper, fabric or 3D structures which are

not suitable for the most common inorganic materials as silicon. The possibility of fabricating flexible electronics is now a reality; flexible smart tags, displays, integrated circuits solar cells etc…are now available at the state of the art [10].

1.1 Conjugated polymers

The key element on organic compounds is the Carbon atom, generally bonded to other atoms such as Hydrogen, Nitrogen, Oxygen, Sulphur, Phosphor etc…The carbon atom is characterized by 6 electrons distributed as $1s^1 2s^2 2p^2$. It is very common that one of the two $2s^2$ electrons can jump into the free $2p_z$ orbital, thus leading to four valence electrons, 2s $2p_x$ $2p_y$ $2p_z$. The orbitals of the four valence electrons in the outer shell of the carbon atom can be configured in several ways depending of the overlapping, resulting in the so called hybrid orbitals.

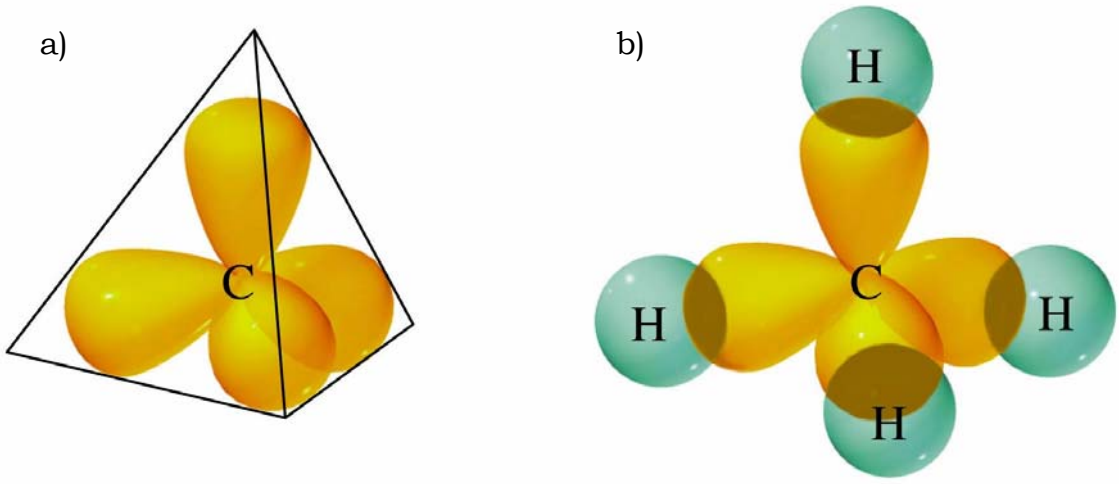

Figure 1.1: Four sp^3 orbitals are directed toward the corners of a tetrahedron (a); the orbital structure of methane, showing the overlap of the four sp^3 orbitals of carbon with the s orbitals of four hydrogen atoms to form four σ (covalent) bonds between carbon and hydrogen (b).

When a carbon atom has four single bonds, the 2s-orbital and the three 2s-orbitals hybridise and form four equivalent sp^3-orbitals, equally shaped and oriented towards the corners of a regular tetrahedron, see Figure 1.1. All bonds between s-orbitals or hybrids of s-orbitals and p-orbitals are called σ-bonds, and the electrons involved are called σ-electrons. When one 2s-orbital combines with two of the three 2p-orbitals, three hybrid sp^2-orbitals will be formed. As a result, there will be three sp^2 orbitals lying on the same plane and one unhybridized one ($2p_z$), that is standing perpendicular, as sketched in Figure 1.2 (a). When two sp^2 hybridized carbon atoms bond each other, the sp^2 orbitals will overlap forming the so called σ-bond. At the same time, the unhybridized p_z orbitals will start interacting too, forming a different kind of bond, called π-bond (see Figure 1.2 (b)).

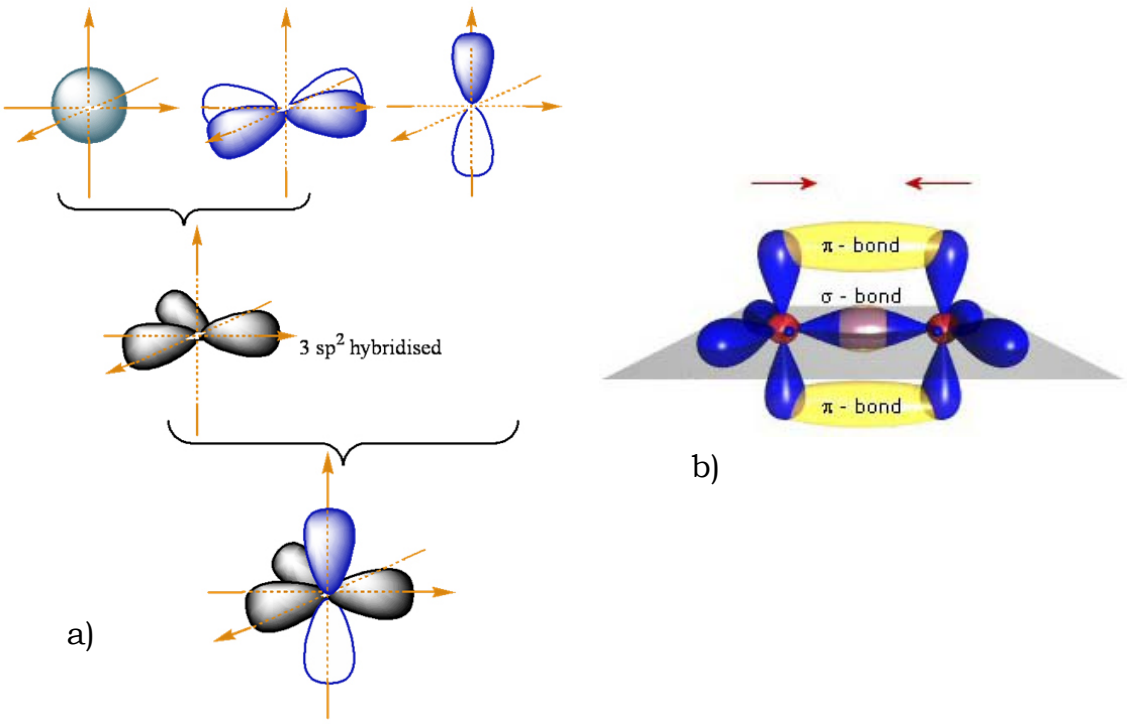

Figure 1.2: one s-orbital and two p-orbitals hybridize to give three sp^2 orbitals and one remaining p orbital perpendicular to plane (a); when 2 carbon atoms approach each other they can form one sigma bond (sp2-sp2 overlap) and one pi (π) bond (b).

σ-bonds are typically very strong bonds and the electrons involved are too localized to be free to move. As a result, σ-electrons are not involved in charge transport mechanism and σ-bonds form the skeleton of the structure, and are responsible for the geometrical properties of the resulting molecule. On the contrary, π-bonds are very weak and the electrons involved are much delocalized so that they can freely move across the molecule, in particular when an electric field is applied.

In such kind of hybridized bonds, π-bonds occur alternatively every 2 molecules. The key structure in a conducting polymer is a linear chain of conjugated units, in which single and double bonds alternate. In these molecules, the p-orbitals of the π-electrons overlap, thus, the arrangement of the electrons is reconfigured concerning the energy levels. A typical example is the benzene ring, that will be introduced in section1.3. We can separate the molecular energy levels into two categories: π and π^* bonding and anti-bonding respectively, forming a band-like structure. The occupied π-levels are the equivalent of the valence band in inorganic semiconductors.

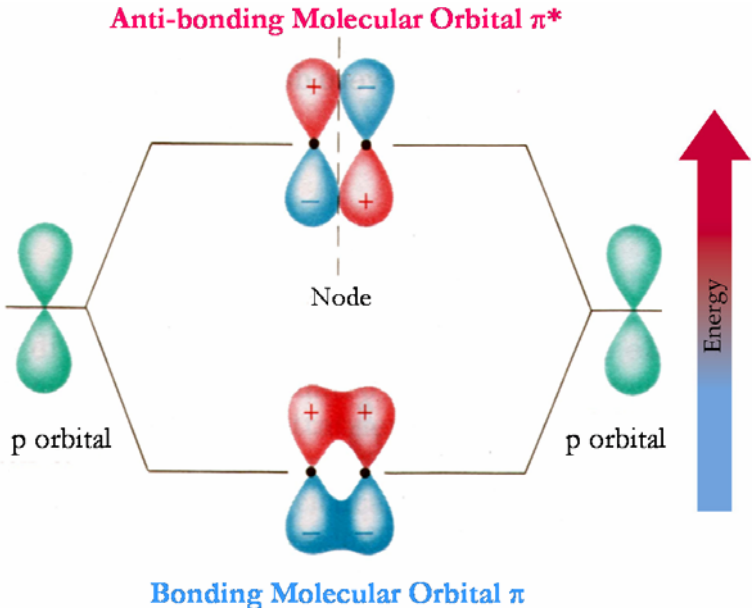

Figure 1.3: bonding and anti-bonding π molecular orbitals.

The electrically active level is the highest one and it is called Highest Occupied Molecular Orbital (HOMO). The unoccupied π*-levels are equivalent to the conduction band. In this case, the electrically active level is the lowest one, called Lowest Unoccupied Molecular Orbital (LUMO). The resulting band gap is given by the difference of the energy between HOMO and LUMO. If we consider a polymer chain with N atoms using the quantum mechanical model for a free electron in a one dimensional box, the wave functions for the electrons of the polymer chain is given by:

$$E_n = \frac{n^2 h^2}{8mL^2} \qquad (1.1)$$

with n=1, 2, 3 etc...and where h is the Plank constant, m the electron mass and L the conjugation length, which, if we consider N atoms separated by a distance d within the polymer chain, is equal to Nd. Therefore, if the π-electrons from the p-orbitals of the N atoms occupy these molecular orbits, with 2 electrons per orbit, then the HOMO should have an energy given by:

$$E(HOMO) = \frac{\left(\frac{N}{2}\right)^2 h^2}{8m(Nd)^2} \qquad (1.2)$$

whereas, the LUMO will have an energy of:

$$E(LUMO) = \frac{\left(\frac{N}{2}+1\right)^2 h^2}{8m(Nd)^2} \qquad (1.3)$$

All energies are supposed to be measured with respect to vacuum energy level as reference. Thus, the energy required to excite an electron from the HOMO to the LUMO is give by their energies difference:

$$E_G = E(LUMO) - E(HOMO) = \frac{(N+1)^2 h^2}{8m(Nd)^2} \approx \frac{h^2}{8md^2 N} \text{ for large N} \qquad (1.4)$$

It is evident that the band gap is inversely proportional to the conjugation length L, and, as a consequence, to the number of atoms N in the polymer chain. If the band gap is high the material is an insulator, if it is low the material is a conductor. Usually the most of the organic semiconductors have a band gap between 1.5 to 3 eV.

1.2 Charge transport in organic materials

Inorganic semiconductors such as Si or Ge, atoms are held together by very strong covalent bonds and charge carriers moves as highly delocalized plane waves in wide bands and usually have very high mobility [11]. In these materials, charge transport is limited by scattering of the carriers, mainly on phonons, that is, thermally induced lattice deformations [12]. This model is no longer valid for low conductivity materials as organic semiconductors. The weak intermolecular interaction forces in these materials, most usually Van der Waals interactions, lead the vibrational energy of the molecules to reach a magnitude close to the intermolecular bond energy at or above room temperature. In this case, the mean free path of charge carriers can be smaller than the mean atomic distance and transport occurs by hopping of charges between localized states. The main difference between the two cases in that in the former charge transport is limited by phonon scattering, whereas in the latter, it is phonon assisted. According to this, charge mobility increases with temperature and is

generally thermal activated. One indubitable point is that charge transport in organics is directly connected to the structural characteristics of the organic film, either in the small scale, such as molecular packing, or in a large scale as grain nucleation within the film. Generally, it can be divided into three levels: i) charge transport within the same molecule (intra-chain); ii) charge transport between two close molecules (inter-chain); iii) charge transport between two close domains, usually called grains (inter-grain). There are several methodologies employed for estimating the electrical properties in organic films, i.e. charge carrier mobility. Many groups use to make Time of Flight (TOF) and Hall Effect measurements, which can give a clear indication of charge transport in the bulk of the material, but the most employed method, which is the one we will use during this thesis, is employing the deposited semiconductor film as active layer in a Field Effect Transistor and measure the channel mobility.

Unfortunately, compared to the tremendous progress that organic electronics has known during the past years, the theory of charge transport has scarcely evolved. However, several models have been developed, but a universal theory which can describe properly charge transport in organic materials does not exist and transport properties are still not fully explained. In the following sections a brief introduction to the most used models will be given.

1.2.1 The small polaron model

A slow moving electron in an organic semiconductor, interacting with lattice ions through long-range forces will permanently be surrounded by a region of lattice polarization and deformation caused by the moving electron. A polaron results from the deformation of a conjugated chain under the action of a charge. In other words, in a conjugated molecule, a charge is self-trapped by the deformation it induces in the chain and it is described by the formation of localized

states in the gap between HOMO and LUMO. One model to describe charge transport in organic materials is the small polaron model introduced by Holstein [13, 14]. The problem generally consists in solving a (low-electron-density) Hamiltonian of the form:

$$H = H_e + H_{pol} + H_{e\text{-}pol} \qquad (1.5)$$

where H_e describes the energy of the charge carriers in the unpolarized molecular material, H_{pol} represents the energy of the induced polarizations in the local environment and $H_{e\text{-}pol}$ describes the interaction energy between the charge carriers and their surrounding polarizations. Besides the different methods that can be used to solve this Hamiltonian [15-17], the main differences between the various reported research works concern the simplifications that are made in the second and third term of the Hamiltonian. For simplicity, most authors choose to focus their calculations on only one of the three polarization processes, i.e. they study the electronic polaron (or Coulomb polaron) [18, 19], or the molecular polaron [14], or the lattice polaron [20-23]. In Holstein model, the lattice energy is given by a sum of N harmonic oscillators that vibrate at a unique frequency ω_0:

$$E_L = \sum_{n=1}^{N} \frac{1}{2M}\left(\frac{\hbar}{i}\frac{\partial}{\partial u_n}\right)^2 + \frac{1}{2}M\omega_0^2 u_n^2 \qquad (1.6)$$

where, u_n is the displacement of the n_{th} molecule from its equilibrium position, and M is the reduced mass of each molecular site. The electron-lattice coupling is given by:

$$E_k = E_0 - 2J\cos(ka) \qquad (1.7)$$

$$\varepsilon_n = -Au_n \qquad (1.8)$$

here J is the electron transfer energy, a is the lattice constant and A is a constant. An important parameter is the polaron binding energy E_b which is defined as the energy gain of an infinitely slow carrier due to the polarization and deformation of the lattice.

$$E_b = A^2/(2M\omega_0^2) \qquad (1.9)$$

The mobility of the small polaron is calculated by solving the time dependent Schroedinger equation. Its upper limit is given by the following equation, where it is worth to point out that the term $ea^2/\hbar$ has the dimension of a mobility and it is very close to 1cm^2/Vs in most molecular crystals [13].

$$\mu = \sqrt{\frac{\pi}{2}}\frac{ea^2}{\hbar}\frac{J^2}{\sqrt{E_b}}(kT)^{-3/2}\exp(-\frac{E_b}{2kT}) \qquad (1.10)$$

1.2.2 Hopping Transport

The absence of an ideal 3D periodic lattice in disordered organic semiconductors does not allow to describe charge carrier transport in terms of band conduction. In this case, charge carriers move between localized states, and charge transfer is generally described in terms of hopping transport, which is a phonon-assisted tunnelling mechanism from site to site [24, 25]. This phonon-induced hopping mechanism was suggested by Conwell [26] and Mott [24]. Later, Miller and Abrahams proposed a hopping model based on a single-phonon jump rate description [25]. The localized states are shallow impurity levels. The energy of these levels stands in a very narrow range so the probability for a charge carrier on one site to find a phonon to jump to the closest site is high. The model predicts that the hopping rate between an

occupied site *i* and an adjacent unoccupied site *j*, which are separated in energy by E_i-E_j and in distance by R_{ij} is given by:

$$W_{i,j} = \upsilon_0 \cdot \exp(-2\Gamma R_{i,j}) \begin{cases} \exp(-\dfrac{\varepsilon_i - \varepsilon_j}{k_B T}) & \varepsilon_i > \varepsilon_j \\ 1 & \varepsilon_i < \varepsilon_j \end{cases} \qquad (1.11)$$

where, Γ^{-1} quantifies the wavefunction overlap between the sites, ν_0 is an empirical pre-factor, and k_B is the Boltzmann constant. Depending on the structural and energetic disorder of the system, it can be possible that a charge carrier finds more favourable to hop over a larger distance with a lower activation energy than over a shorter distance with a high activation energy. This extension to the Miller-Abrahams model is called Variable Range Hopping (VHR). This model was introduced by Vissemberg and Matters [27], and describes the temperature and gate voltage dependence in OFETs introducing a percolation model based on VRH in an exponential density of states.

1.2.3 Multiple Trapping and Thermal Release (MTR)

Another model that is used to describe the temperature dependent transport in polycrystalline organic semiconductors is the so called Multiple Trapping and Thermal Release (MTR). This model was introduced to explain charge transport in amorphous silicon devices and was used by Horowitz et al. [28] to interpret the data obtained on poly-crystalline sexithiophene OFETs. They assumed that traps are not homogeneously distributed within the semiconductor film, but are mostly localized in the grain boundaries. In this model the organic semiconductor film consists of crystallites which are separated from each other by amorphous grain boundaries. In the crystallites charge carriers can move in delocalized bands, whereas in the grain boundaries they become trapped in localized states. The trapping and release of

carriers at these localized states results in a thermal activated behaviour of the field effect mobility, which depends on the gate voltage.

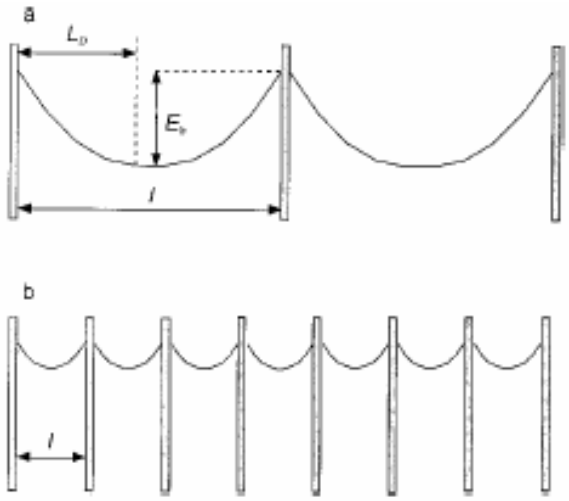

Figure 1.4: Energy scheme of a polycrystalline semiconductor in two limiting cases. a) $l > 2L_D$; b) $l < L_D$. l is the grain size, L_D the Debye length and E_b the barrier height. Because of defect-induced localized levels in the grain boundaries, back-to-back Schottky barriers are assumed to form at the intergrain regions. Note that L_D only depends on temperature and doping level, and has therefore the same magnitude in (a) and (b).

In fact, polycrystalline films can be considered as formed by two different areas, one with high mobility (the crystal grains) and another with a low mobility (the grain boundaries). Since the grains are, under the electrical point of view, connected as resistors in series, the total mobility can be given by:

$$\frac{1}{\mu} = \frac{1}{\mu_g} + \frac{1}{\mu_b} \qquad (1.12)$$

where μ_g and μ_b are the mobility in the crystal grain and in the grain boundary respectively. If the defects are mostly located at the grain boundaries, then $\mu_g >> \mu_b$ and the total mobility is almost equal to the mobility in the grain boundaries. A general assumption is that, due to

the presence of defect states in the grain boundaries, a back-to-back Schottky barrier forms at the intergrain region. The energy scheme of the medium may present two limiting forms, given in Figure 1.4, depending on the respective magnitude of grain size l and Debye length $L_D = \sqrt{\varepsilon_S kT / q^{2N}}$ (where ε_s is the permittivity of the semiconductor, k is Boltzmann's constant, T the absolute temperature, q the electron charge, and N the doping level). Therefore, if $l < L_D$ traps are uniformly distributed in the organic semiconductor film, whereas if $l > 2L_D$ we can consider traps as mostly concentrated at the grain boundaries.

According to the back-to-back Schottky barrier picture, the current flowing through a grain boundary at room temperature is limited by thermionic emission. For large grains (l > 2LD) the mobility is given by Equation 1.13 where v represents the electron mean velocity.

$$\mu = \frac{q\langle v \rangle l}{8kT} \exp\left(-\frac{E_b}{kT}\right) \qquad (1.13)$$

interestingly, the pre-exponential factor is not related to the mobility in the grain, that is, the mobility in a trap-free material. Equation 1.13 suggests that the mobility would increase linearly with grain size, and the activation energy E_b can be easily estimated from the temperature dependence of the mobility [29].

1.2.4 Charge injection into organic semiconductor

Charge transport along the active organic semiconductor film is not the only important subject for describing the physical properties of OFETs. Metal/organic semiconductor interfaces are very important and can strongly influence both the type and the amount of charge carrier injected into the channel. In principle, all organic semiconductors should be able to allow both kinds of charge carriers transport. Therefore, achieving n-type or p-type conduction should only depend on

the metal employed for the electrodes that should be able to efficiently inject one type of charge carriers into the semiconductor layer. Indeed, charge injection strongly depends on the energy level matching between the Fermi level of the metal electrodes and organic semiconductors energy levels, namely, lowest unoccupied molecular orbital (LUMO) and highest occupied molecular orbital (HOMO). One of the fundamental aspects of the metal/semiconductor interface is the Fermi level alignment, described by the Mott-Schottky model [30, 31]. When a neutral metal and a neutral semiconductor are brought in contact, the Mott-Schottky model predicts that their bulk Fermi levels will align, causing band bending in the semiconductor (see Figure 1.5).

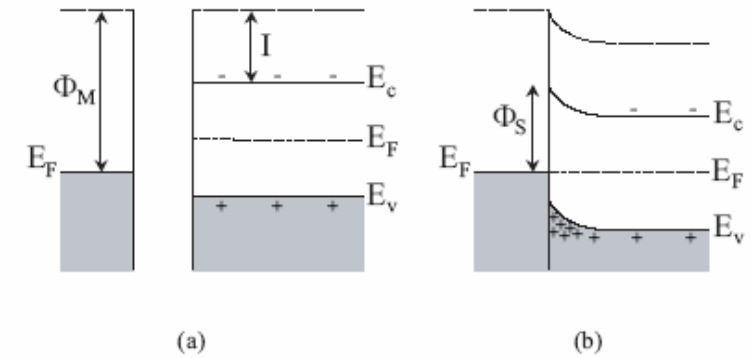

Figure 1.5: Energy-band diagrams under thermal equilibrium for (a) a metal (left) and an intrinsic semiconductor (right) that are not in contact; (b) a metal/semiconductor contact, with a band bending region in the semiconductor, close to the interface with the metal. *Ec* and *Ev* indicate the edge of the conduction band and the edge of the valence band; E_F indicates the position of the Fermi level.

Due to the band bending, a non-Ohmic Schottky barrier can be formed at the interfaces between metal and semiconductor. As a consequence, charge transport can be limited by injection through the Schottky barrier and is characterized by thermal excitation of charge carriers over the barrier, resulting in thermally excited temperature dependence. Mott-Schottky model is generally used as a guideline for choosing the contact metal. The height of the injection barrier will be

given by the difference between the metal Fermi level and the HOMO or LUMO levels of the organic semiconductor for holes and electrons respectively. According to this, gold is generally used for the realization of p-type organic transistors, since its relatively high work function (5.1 eV) forms a low hole injection barrier with the most common organic semiconductors (i.e. pentacene, sexithiophene, dihexylsexithiophene). On the other hand, low work function metals, as calcium (i.e. 2.9 eV) are generally used as electron injectors. There are several aspects that can modify the Mott-Schottky-type of band bending. One of these is the formation of surface dipoles at the interface between the metal and the organic semiconductor. The large interface dipole was explained by the change of the surface dipole of the metal upon adsorption of the molecule. A metal surface is characterized by an electron density tailing from the free surface into vacuum. Adsorbed molecules tend to push back these electrons, thus reducing the surface dipole and decreasing the work function of the metal that can induce a vacuum level shift that can change the barrier height [32, 33] as carefully explained by Kahn et al. [34].

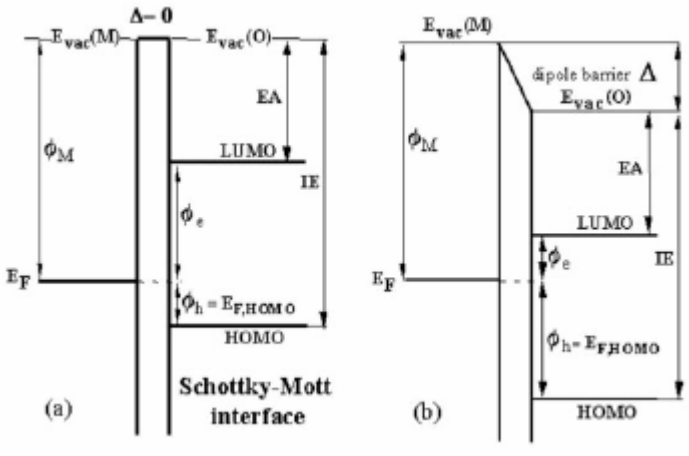

Figure 1.6: Energy diagram of an MO semiconductor interface (a) without and (b) with a dipole barrier (Δ). Φe and Φh are the electron and hole barriers, respectively, and *E*vac(O) and *E*vac(M) are the organic and metal vacuum levels, respectively. Taken from ref. [34].

Another aspect that can have a strong influence in charge injection is the presence of traps at the metal/organic interface that are mostly produced during contact fabrication [35]. The deposition of metal contact over the already deposited organic film can lead to local damages in the crystalline structure of the material due to the diffusion of the deposited specie into the active layer upon deposition. On the other hand, the deposition of the organic material on the top of the pre-patterned electrodes can lead to an accumulation of structural defects at the triple interface between the metal contact, substrate and organic semiconductor. In fact, in this case the organic material is not grown on a bare flat surface and the presence of pre-patterned structures as the electrodes can induce discontinuities in the morphology of the deposited film that acts as trapping sites for charge carrier to be injected into the channel.

1.3 Specific Materials

Most organic materials employed for electronics applications can be classified into two families: i) aromatic compounds; ii) heterocyclic compounds. The core of the aromatic compound family is the benzene ring, reported in Figure 1.7 (a). The benzene ring (C_6H_6) consists of six carbon atoms bonded in a flat or planar hexagon ring. Each carbon atom in the hexagonal cycle has four electrons to share. One goes to the hydrogen atom, and one each to the two neighboring carbons, with an alternation of a single and a double bond. Aromatic compounds are basically formed by a concatenation of several benzene rings that leads to obtain a rodlike conjugated molecule. The core of the heterocyclic compounds is the thiophene ring. Thiophene (C_4H_4S) is a heterocyclic compound consisting of four carbon atoms and one sulfur atom in a five-membered ring, see Figure 1.7 (b). Also in this case carbon atoms are bonded to a hydrogen atom with a single bond and to the neighbour atoms of the ring by one single and one double bond.

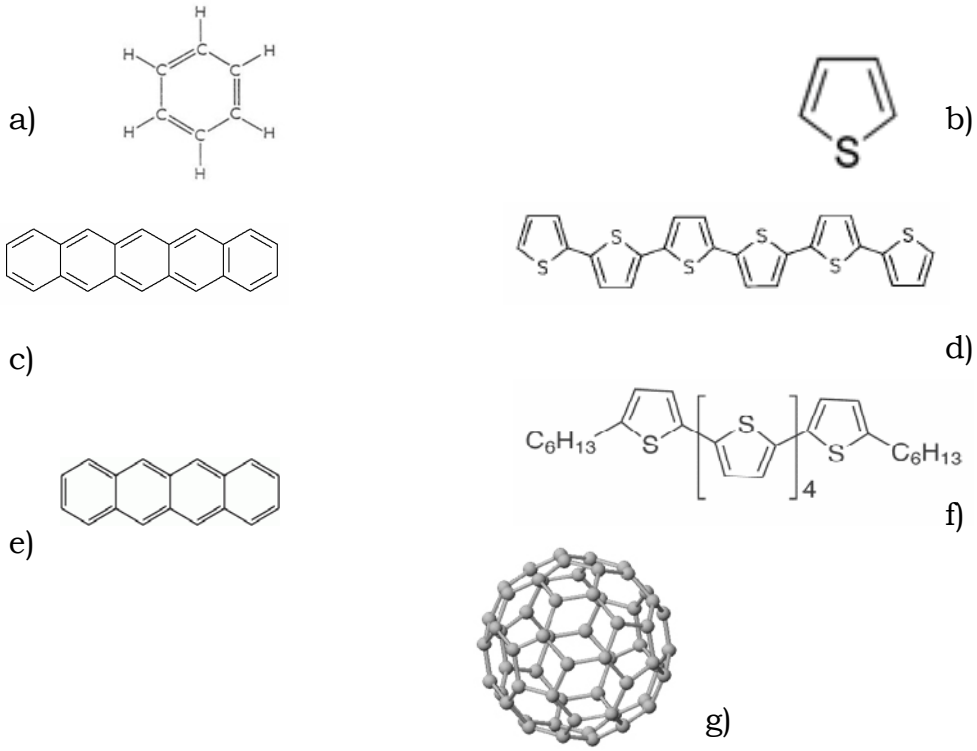

Figure 1.7: chemical structure of benezene ring (a), thiophene ring (b), pentacene (c), α-sexithiophene (d), tetracene (e), α,ω-dihexylsexuthiophene (f) and fullerene C_{60} (g).

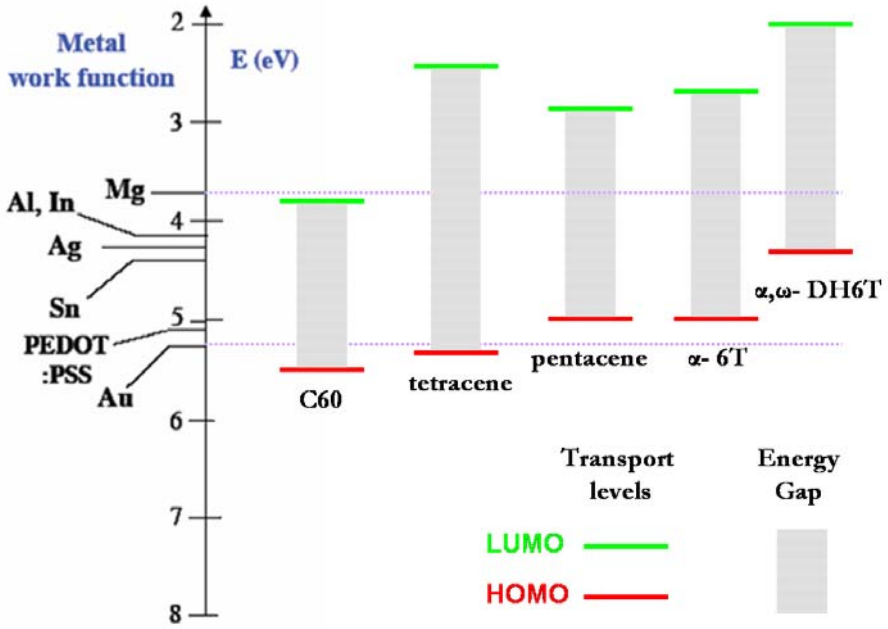

Figure 1.8: Band structure showing LUMO and HOMO energy levels of the employed organic semiconductors.

In the following sections the materials employed during the experimental acivity described in this thesis will be described.

1.3.1 Pentacene

Pentacene is a polycyclic aromatic hydrocarbon molecule consisting of 5 linearly-fused benzene rings, as depicted in Figure 1.7 (c). Pentacene is one of the most used and the most promising organic semiconductors. This is the typical example of a rod-like molecule where one of the three axes is definitely longer than the other two. For a molecule like pentacene, charge transport across the semiconductor film strongly depends not only on the overlapping of the π-orbitals in the direction of the longest axis of the molecule (intra-chain charge transport), but also on the interaction of the π-orbitals between two close molecules (inter-chain charge transport). Therefore, charge carrier transport properties, in particular mobility, are strongly influenced by structural morphological properties of the assembled film. At the state of the art, pentacene is the organic semiconductor that showed the highest performances in terms of stability and also in terms of the measured mobilities. Mobilities up to 1 cm^2/Vs have been recorded for polycrystalline pentacene films, whereas even higher mobilities, up to 30 cm^2/Vs, were measured for pentacene single crystals [36, 37]. It is characterized by a wide band gap (as most organic semiconductors) around 2,2 eV. Pentacene has an Ionization Energy (which correspond to the HOMO energy level) around 5.2 eV and an Electron Affinity (LUMO level) around 3 eV. This means that it forms a very low hole injection barrier but a very high electron injection barrier when using Au as metal electrode. This is the reason why it is typically employed as p-type semiconductor in most organic electronics applications.

1.3.2 Tetracene

Tetracene, also called naphthacene and 2,3-benzanthracene, is a polycyclic aromatic hydrocarbon, see Figure 1.7 (e). The molecule is very similar to pentacene, but it is characterized by four linearly fused benzene rings. If compared to pentacene, tetracene shows lower electronic performances. It is very unstable and quickly degrades upon exposure to light and oxygen. Moreover, the recorded mobilities for this material are in the range of 10^{-2} to 10^{-3} cm^2/Vs up to 0.4 cm^2/Vs for single crystal film, measured by Morpurgo et al. [38]. Nevertheless, this material has been extensively studied for its photoluminescence properties, and has been employed as active material for the realization of Organic Light Emitting Transistors (OLETs) [39, 40].

1.3.3 α-sexithiophene (α-6T)

Sexithiophene is a heterocyclic compound characterized by a concatenation of six thiophene rings as depicted in Figure 1.7 (d). It is one of the most extensively studied oligothiophene compounds, mainly employed as active layer for the realization of OFETs. Several examples have been reported so far in literature with mobilities up to $0.1cm^2/Vs$ and $1x10^{-2}cm^2/Vs$ for single crystal and polycristalline devices respectively [13, 41, 42]. α-6T energy levels are very similar to pentacene ones, with a Ionization Energy close to 5 eV and a energy bad gap around 2.3 eV. Therefore, also this material is generally employed as p-type semiconductor when using a high work function metal.

1.3.4 α,ω-dihexylsexithiophene (α,ω-DH6T)

One of the main advantages of organic electronics is the possibility to use molecular chemistry tailoring in order to tune and modulate the properties of the basic molecule itself. As can be clearly noticed from the picture depicted in Figure 1.7 (f), the α,ω-DH6T molecule is very similar to the 6T one. The only difference is the

presence of two lateral alkyl-chain substituents located at both ends of the molecule, in α,ω position respectively. Mobilities in the range of 1cm^2/Vs and 0.1cm^2/Vs have been reported in literature for single crystal and polycristalline devices respectively [13, 42]. As can be noticed from the energy levels diagram depicted in Figure 1.8, the presence of the alkyl chains sobstituents have a strong influence on the energetics of this system, leading to a reduction of its Electron Affinity to 2 eV. Also in this case, due to the very high electron injection barrier that DH6T forms with the most common metals (even with low work function ones) it is seldom employed as n-type material.

1.3.5 Fullerene - C_{60}

Due to their electronic band structure, nearly all organic semiconductors are able to transport only one kind of charge carrier, either hole or electrons. The reason for that, can be found in the fact that most metals employed for the realization of the electrodes are characterized by a high work function (typically around 4.5 to 5.5 eV), thus leading to have a very high electron injection barrier at the interface between metal electrode/organic semiconductor, since the typical values of the LUMO level for organic semiconductors is around 2.5 to 3eV. The materials introduced before, were mainly employed for the realization of OFETs working in p-type mode.

C_{60} is one of the most interesting organic semiconductors, see Figure 1.7 (g). Due to its high photoluminescence and photoconductivity it has been extensively employed for optoelectronic applications, in particular for the realization of Organic Photovoltaic Solar Cells. Its relatively high LUMO level (3.7-4.1 eV) allows to minimize the electron injection barrier, therefore, it can be used for the realization of n-type OFETs even with high work function metal electrodes.

1.3.6 PEDOT:PSS

One of the most studied and characterised conjugated polymers is the p-doped poly(3,4-ethylenedioxythiophene) (PEDOT). The structure of PEDOT is shown in Figure 1.9 (a). As the previously mentioned sexithiophene and dihexylsexithiophene, also PEDOT is a thiophene derivative. Due to its high conductivity, it is generally employed, not only as active semiconductor material, but also for the realization of conductive electrodes in several applications such as OFETs and OLEDs [43-49]. Some reasons for the popularity of PEDOT is its excellent chemical stability and its high conductivity. Depending on the counterion (which is the ion that accompanies the ionic species in order to maintain electric neutrality), PEDOT can exhibit conductivities around 300 S/cm [50].

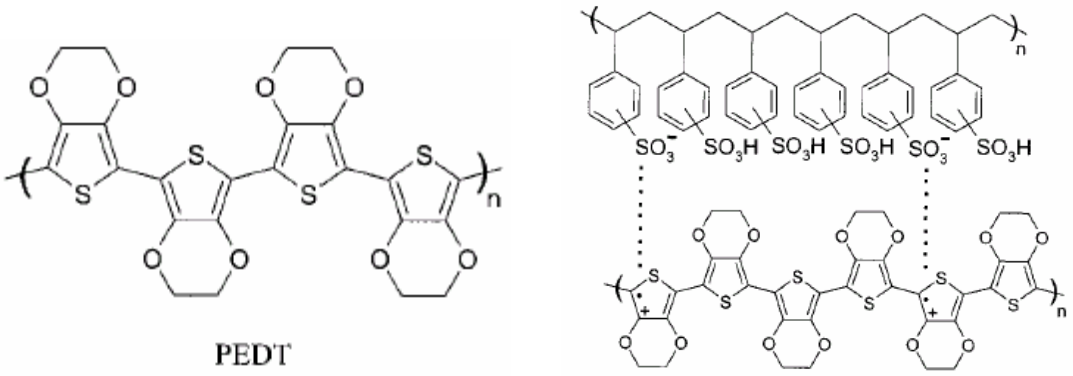

Figure 1.9: chemical structure of PEDOT (a) and PEDOT:PSS (b)

Moreover, it is almost transparent if deposited in thin films. The biggest problem for employing PEDOT in organic electronics applications is its insolubility in most organic solvents. This problem has been overcome by a chemical tailoring of the molecule. When poly(styrene sulphonic acid) (PSS) is used as the counterion, it is possible to obtain a soluble compound, with the same stability and transparency properties, but with a lower conductivity that typically reaches 10 S/cm in solid state thin films [51]. One key factor for the

conductivity of the film is the morphology. By mixing PEDOT:PSS with sorbitol, Nmethylpyrrolidone (NMP) or isopropanol the morphology of the resulting film is controlled in a favourable manner. Such treatment gives an increase in the conductivity [52]. Ouyang et al. [53] have shown that solvents with more than two polar groups, in particular ethylene glycol, increases the conductivity even more. They suggest that increased interchain interaction and conformational change is the mechanism behind this. The morphology of a PEDOT film is a phase segregation with grains consisting of conductive PEDOT:PSS in a matrix of insulating PSS. The thickness of the grain boundary is about 40Å [54]. The grains show metallic-like electron conductivity while the grain boundary layer consists of PSSH that is an ion conductor having low electronic conductivity. Therefore, electric current in a PEDOT:PSS film is easily transported within the grains while the main obstacle is to transport electric current between the grains. In its doped form, PEDOT shows excellent properties as a transparent charge injection layer in light emitting diodes as well as the conducting electrodes/contacts in field effect transistors.

References

[1] C. K. Chiang, C. R. Fincher, Jr., Y. W. Park, and A. J. Heeger, H. Shirakawa, E. J. Louis, S. C. Gau, and Alan G. MacDiarmid Phys. Rev. Lett. 39, 1098 - 1101 (1977)

[2] S. R. Forrest, Nature 428, 911 (2004).

[3] T. Tsujimura, SID 2003 Tech. Dig. XXXIV, 6 (2003).

[4] T. N. Jackson, Y. Y. Lin, D. J. Gundlach, and H. Klauk, IEEE J. Sel. Top. Quantum Electron. 4, 100 (1998).

[5] F. Garnier, R. Hajlaoui, A. Yassar, and P. Srivastava, Science 265, 1684 (1994).

[6] A. Bonfiglio, F. Mameli, and O. Sanna, Appl. Phys. Lett. 82, 3550 (2002).

[7] Y. Kato, S. Iba, R. Teramoto, T. Sekitani, T. Someya, H. Kawaguchi, and T. Sakuray, Appl. Phys. Lett. 84, 3789 (2004).

[8] J. A. Rogers, MRS Bulletin 530 (2001).

[9] G. Gustafsson, Y. Cao, G. M. Treacy, F. Klavetter, N. Colaneri, and A. J. Heeger, Nature 357, 477 (1992).

[10] R. H. Reuss, B. R. Chalamala, A. Moussessian, M. G. Kane, A. Kumar, D. C. Zhang, J. A. Rogers, M. Hatalis, D. Temple, G. Moddel, B. J. Eliasson, M. J. Estes, J. Kunze, E. S. Handy, E. S. Harmon, D. B. Salzman, J. M. Woodall, M. Ashraf Alam, J. Y. Murthy, S. C. Jacobsen, M. Olivier, D. Markus, P. M. Campbell, And E. Snow, Proceeding of IEEE, Special issue on Flexible Electronics Technology, Part1: Systems & Applications, 93, (2005).

[11] C. D. Dimitrakopoulos, P. R. L. Malenfant, Adv. Mat. 14, 99 (2002).

[12] G. Horowitz, J. Mater. Res., 19, (2004).

[13] G. Horowitz, Adv. Mater. 10, 365, (1998).

[14] T. Holstein, Ann. Phys. (NY) 8, 343, (1959).

[15] R. M. Glaeser, and R. S. Berry, J. Chem. Phys. 44, 3797 (1966).

[16] V. M. Kenkre, J. D. Andersen, D. H. Dunlap, and C. B. Duke, Phys. Rev. Lett. 62, 1165 (1989).

[17] J. Sinova, J. Schliemann, A. S. Nunez, and A. H. MacDonald, Phys. Rev. Lett. 87, 226802 (2001).

[18] E. V. Tsiper, and Z. G. Soos, Phys. Rev. B 64, 195124 (2001).

[19] M. N. Bussac, J. D. Picon, and L. Zuppiroli, Europhys. Lett. 66, 392 (2004).

[20] R. W. Munn, and R. Silbey, J. Chem. Phys. 83, 1843 (1985)

[21] A. J. Millis, R. Mueller, and B. I. Shraiman, Phys. Rev. B 54, 5389 (1996).

[22] A. Girlando, M. Masino, A. Brillante, R. G. Della Valle, E. Venuti, Phys. Rev. B 66, 100507 (2002).

[23] K. Hannewald, and P. A. Bobbert, Appl. Phys. Lett. 85, 1535 (2004); K. Hannewald, V. M. Stojanovic, J. M. T. Schellekens, P. A. Bobbert, G. Kresse, and J. Hafner, Phys. Rev. B 69, 075211 (2004)

[24] N.F. Mott, Canadian J. Phys. 34, 1356 (1956).

[25] A. Miller and E. Abrahams, Phys. Rev. 120, 745 (1960).

[26] E. M. Conwell, Phys. Rev. 103, 51 (1956).

[27] M.C.J.M. Vissenberg and M. Matters, Phys. Rev. B 57, 12964 (1998).

[28] G. Horowitz, R. Hajlaoui and P. Delannoy, J. Phys. III 5, 355 (1995).

[29] G. Horowitz and M. E. Ajhlaoui, Adv. Mater. 12, 1047 (2000).

[30] R. W. I. De Boer, Ph. D. Thesis, Technische Universiteit Delft.

[31] S. M. Sze, Physics of Semiconductor Devices (Wiley, New York, 1981).

[32] H. Ishii, K. Sugiyama, E. Ito, and K. Seki, Adv. Mater. 11, 605 (1999).

[33] H. Peisert, M. Knupfer, T. Schwieger, J. M. Auerhammer, M. S. Golden, J. Fink, J. Appl. Phys. 91, 4872 (2002).

[34] A. Kahn, N. Koch, W. Gao, Journal of Polymer Science: Part B: Polymer Physics, 41, 2529 (2003).

[35] C. D. Dimitrakopoulos, and D. J. Mascaro, IBM J. Res. & Dev. 45,11 (2001).

[36] H Klauk, D. Gundlach, J. A. Nichols, T. N. Jackson, IEEE Transaction on Electron Devices 46, 6 (1999).

[37] R. G. Endres, C. Y. Fong, L. H. Yang, G. Witte and Ch. Wölle, Comput. Mater. Science 29, 362 (2004).

[38] R. W. I. de Boer, T. M. Klapwijk and A. F. Morpurgo, Appl. Phys. Lett. 83, 4345 (2003).

[39] Hepp, A., H. Heil, W. Weise, M. Ahles, R. Schmechel, and H. von Seggern, Phys. Rev. Lett., 91, 157406 (2003).

[40] C. Santato, I. Manunza, A. Bonfiglio, F. Cicoira, P. Cosseddu, R. Zamboni and M. Muccini, Appl. Phys. Lett. 86, 141106 (2005).

[41] P. Stallinga, H. L. Gomes, F. Biscarini, M. Murgia, D. M. de Leeuw, 96, 5277 (2004).

[42] G. Horowitz, R. Hajlaoui and F. Kouki, Eur. Phys. J. AP, 1, 361 (1998).

[43] D. Nilsson, Ph. D. Thesis, Linkoping Studies in Science and Technology, Dissertation N° 921.

[44] T. Kawase, T. Shimoda, C. Newsome, H. Sirringhaus and R. H. Friend Thin Solid Films 438, 279 (2003).

[45] G. Blanchet, J. Rogers, Journ. of Imag. Sc. and Techn. 47, 303 (2003).

[46] C. J. Drury, C. M. J. Mutsaers, C. M. Hart, M. Matters, and D. M. de Leeuw, Appl. Phys. Lett 73, 108 (1998).

[47] M. Matters, D. M. de Leeuw, M. J. C. M. Vissemberg, C. M. Hart, P. T. Herwig, T. Geuns, C. M. J. Mutsaers and C. J. Drury, Opt Mater 12, 189 (1999).

[48] A. Dodabalapur, Solid State Commun., 102, 259 (1997).

[49] Y. Cao, G. Yu, C. Zhang, R. Menon and A.J. Heeger, Synth. Met. 87, 171, (1997).

[50] A. Aleshin, R. Kiebooms, Reghu Menon, F. Wudl, and A. J. Heeger, Phys. Rev. B 56, 3659 (1997).

[51] A. N. Aleshin, S. R. Williams and A. J. Heeger, Synth. Met. 94, 173 (1998).

[52] S.K.M. Jönsson, J. Birgerson, X. Crispin, G. Greczynski, W. Osikowicz,. A.W. Denier van der Gon, W.R. Salaneck, M. Fahlman, Synth. Met. 139, 1(2003).

[53] J. Ouyang, Q.F. Xu, C.W. Chu, Y. Yang, G. Li and J. Shinar, Polymer 45, 8443 (2004).

[54] G. Greczynski , T. Kugler , M. Keil , W. Osikowicz , M. Fahlman, and W.R. Salaneck, J. Electron. Spectrosc. Relat. Phenom. 121, 1 (2001).

Chapter 2

Organic Field Effect Transistors (OFETs)

This chapter is completely dedicated to the description of the Organic Field Effect Transistor. It is basically divided into three parts. In the first part we give a detailed description of the working principles and of the models developed to describe it. Afterwards, there will be an introduction to the most common architectures employed for the realization of OFETs. We will take this a starting point for the description of the structures we employed during this thesis. Finally, we will focus our attention on the fabrication techniques generally used for the device assembly.

2.1 OFET Model

The interest for Organic Field Effect Transistors (OFETs) has drastically increased over the past few years, and they have been intensively studied for many applications such as displays, smart tags and sensors. The reason for focused research interest in the field of "plastic electronics" is the opportunity to produce low cost devices on plastic substrates on large areas, opening, indeed, an entire new market

segment. So far, field effect mobilities up to 30cm^2/Vs have been reported for thin film and single crystal OFETs. However, this value is usually lowered by at least one order of magnitude for organic transistors made on plastic substrates. OFETs are close relatives of the classic Metal Oxide Semiconductor Field Effect Transistors (MOSFETs); typically, since the organic semiconductors are characterized by a low conductivity if compared to inorganic ones, Thin Film Transistor (TFT) architecture is preferred in this case. The core of an OFET is a Metal-Insulator-Semiconductor structure (MIS), which can in principle be considered as a parallel plate capacitor: the two capacitor plates are formed by a metal electrode, called gate electrode, and a semiconductor, which are separated by a thin insulating film, called gate dielectric (see Figure 2.1). Two additional electrodes, called Source and Drain electrodes are patterned in order to contact the organic semiconductor allowing to probe the conduction across the organic film.

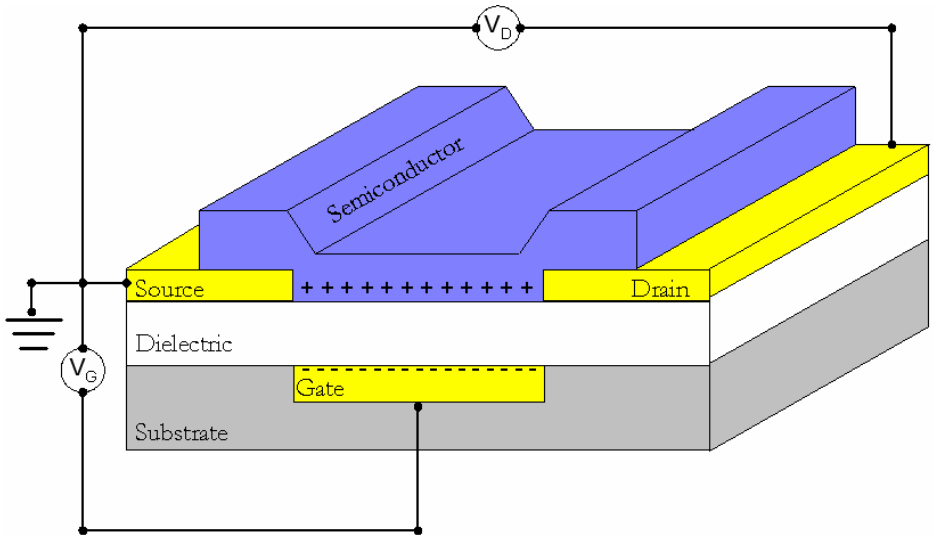

Figure 2.1: Schematic of the OFETs geometry.

One of the main differences between an OFET and the classic MOSFET is that while the latter typically works in inversion mode, OFETs usually work in accumulation mode. When a negative (positive)

voltage is applied between the gate and the source electrodes, an electric field is induced in the semiconductor that attracts positive (negative) charge carriers at the semiconductor/insulator interface between source and drain electrode and overlapping with the gate. Applying a negative (positive) voltage between source and drain electrodes, it is possible to drive the positive (negative) charge carriers across the channel area. Charge transport in OFETs is substantially two-dimensional. Charge carrier accumulation is highly localized at the interface between the organic semiconductor and the gate dielectric, and the bulk of the material is hardly or not affected by gate induced field, see Figure 2.2 [1]. Upon increasing gate voltage to positive (negative) values, the number of charge carriers accumulated in the channel will reduce until the channel is fully depleted of free carriers. From this point on, negative (positive) charges are induced in the channel and the device should in principle work in inversion regime. In practice, the flowing current detectable in inversion regime is negligible because the number of charge carriers injected into the channel is low due to the high injection barrier at the interface between metal electrodes/semiconductor.

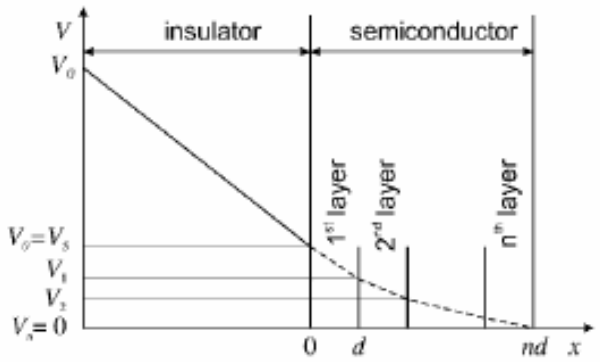

Figure 2.2: potential distribution across the insulator/semiconductor structure in a multilayer structure.

The boundary between accumulation and inversion regime is called threshold voltage V_t of the device. Below the threshold voltage the

device is in its off state, no free charge carriers are present in the channel and no current will flow across it. The equations that govern the OFET working principle are substantially the same of the classic MOSFET. When a gate voltage larger than the threshold voltage is applied, with a small applied source drain voltage ($V_G<V_{DS} << -(V_G-V_T)$), the gate induced field is almost uniformly distributed along the conducting channel, thus a uniform charge distribution is induced in the channel. The device is operating in the linear region, where the current increases linearly in dependence to the applied source drain voltage:

$$I_d = \frac{Z}{L}\mu C_i\left[\left(V_g - V_t\right)V_d - \frac{V_d^2}{2}\right] \qquad (2.1)$$

where, Z is the channel width, L is the channel length, C_i is the gate dielectric capacitance and μ is the charge carrier mobility. For larger drain voltages ($V_G \geq (V_G-V_T)$) the gate field at the drain contact is zero. As a result, a depleted area with no induced free charge carriers is present. This phenomenon is called pinch-off. Beyond this point the current flowing across the channel saturates and a further increase in the applied source/drain voltage will produce no significant effects on the measured current. The channel current in this regime is given by:

$$I_{dsat} = \frac{Z}{2L}\mu C_i\left(V_g - V_t\right)^2 \qquad (2.2)$$

The typical output characteristic of an OFET working in accumulation mode is depicted in Figure 2.3, where the two typical working regimes, linear and saturation regime, are indicated [2].

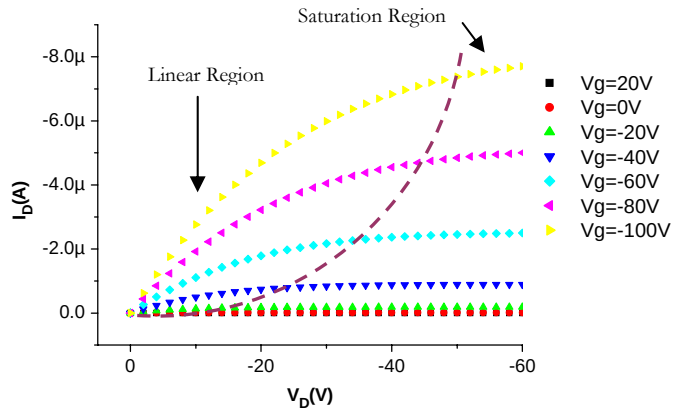

Figure 2.3: Typical output characteristic of an OFETs showing both the linear and saturation regions.

The first examples of OFETs were hybrid structures, where the only "organic" part in the device, was the semiconductor. Typically, the first OFETs were assembled on a highly doped silicon wafer, acting at the same time as substrate and as gate electrode. A thin SiO_2 layer was employed as gate dielectric, whereas metals (i.e. Au, Al) were used for the fabrication of the source and drain electrodes. Nowadays, several examples have been reported concerning the realization of all organic FETs, where a flexible plastic foil is generally used as flexible substrate, a polymeric gate dielectric (PVA or PVP or PMMA) is used instead of SiO_2 [3-5], and conductive polymers are employed as alternative to metals for the patterning of the electrodes [6, 7].

Even though the MOSFET laws are taken as representative also for OFETs, it is well known that, in most cases, the typical behaviour strongly differs from the ideal case. The main reason for such discrepancy is generally ascribed to the intrinsic structural properties of the organic semiconductors. Usually, when we grow an organic semiconductor film, we do not obtain a crystal structure; a single organic crystal can be obtained only under strict deposition conditions. Therefore, when we talk about organic semiconductors, we suppose to discuss about polycrystalline thin film, with a very high concentration

of structural defects which is the main reason for the non-linearity usually observed in such devices. Every defect acts as scattering site for charge carriers, causing the distortion in the, ideally, periodic lattice potential. Therefore, a band-like transport is usually impeded by such scattering process. The effect of defects is even stronger if the defects themselves act as trapping sites for charge carriers. Trapping is relevant when the defect induces one or more energy levels in the band gap of the organic "crystal". A charge carrier will prefer to occupy this lower energy level and the trap localizes the charge carrier in its site. Typically, traps can be divided into two categories, depending on the activation energy that is needed to free the charge carrier: i) shallow traps when the activation energy is in the order of k_BT; ii) deep traps, when the activation energy is outside the range of thermal excitation. Deep traps are often caused by chemical impurities, such as oxidized molecules or molecules that are side products of the main compound synthesis process. The presence of traps within the semiconductor layer can cause a decrease in the density of mobile charges, since trapped carriers are localized at the defect sites. In some cases, when the density of defects is high and they strongly localize charge carriers, their influence can completely dominate charge transport across the semiconductor. This feature usually manifests a thermal activation dependence of the mobility, meaning that charge transport is dominated by defects that in the case of OFETs made of small molecules, are often grain boundaries, and defects at the organic/dielectric interface. Several experiments have been performed on OFETs and several models have been introduced to study charge transport of both polycrystalline and crystalline active layers and its dependence to charge trapping. However, a universal theory which can properly describe charge transport in organic materials does not exist and transport properties are still not fully explained. In the following sections a brief introduction to the most used models will be given. From a structural point of view

we can consider three different charge trapping mechanisms, bulk trapping, interface state trapping and grain boundaries effects.

2.1.1 Charge trapping in the bulk

Usually charge trapping in the bulk of the material leads to space charge limited effects. In order to achieve transistor action these trap levels need to be filled by carriers induced by gate voltage. The field effect mobility is then determined by the ratio between free carriers n_f to the total number of charge carriers n_{tot} , $\theta = n_f /(n_t + n_f)$ and the intrinsic μ_0 mobility of the material is given by:

$$\mu_{FET} = \mu_0 \cdot \theta \qquad (2.3)$$

$$V_{TFL} = \frac{2ed^2 N_t}{3\varepsilon_r \varepsilon_0} \qquad (2.4)$$

where, N_t is charge traps concentration, ε_r and ε_0 are the dielctric constant of the semiconductor and of the vacuum respectively and V_{TFL} is the trap filling voltage. In other words it is the voltage the system needs in order to fill all the bulk traps in the material. It is worth to mention that in this case we are considering a vertical electric field induced by the gate voltage.

2.1.2 Charge trapping at the dielectric/semiconductor interface

Device performance can be strongly influenced also by the insulator/semiconductor interface. The maximum number of interface traps can be estimated using equation 2.5, assuming that densities of deep bulk states and interface states are independent of energy [8]:

$$N_{SS}^{\max} = \left[\frac{S \cdot \log(e)}{kT/q} - 1 \right] \frac{C_i}{q} \qquad (2.5)$$

$$S = \left[\frac{d \log(I_d)}{dV_g} \right]^{-1} = \frac{kT}{q} \cdot \ln 10 \cdot \left(1 + \frac{C_d + C_{it}}{C_i} \right) \qquad (2.6)$$

where $N_{SS}^{\max}$ is the maximum number of interface traps states, k is the Boltzmann's constant, T the absolute temperature, q the electronic charge, C_d and C_{ox} are the capacitances of the depletion region in the semiconductor and the gate dielectric one respectively, whereas C_{it} is the capacitance associated to charges trapped at the interface [2]. S is the inverse sub-threshold slope which can be directly estimated from the transfer characteristics of the device.

2.1.3 Trapping at the grain boundaries

In many cases, in particular for polycrystalline materials the currents instead of being controlled by traps, can be governed by grain boundaries. It is often very complicated to decide between a grain-boundary-barrier model and a trap model on the basis of the experimental results. As discussed by Street et al., the evidence for the barrier model can be found in the linearity of the so called Levinson plot of $ln(I_D/V_G)$ *vs* $1/V_G$ [9, 10]. This model is based on the predicted OFET drain current in the linear regime given by:

$$\begin{aligned} I_D &= \mu_0 V_D C_G (W/L) V_G \exp(-E_B/kT) \\ &\equiv \mu_0 V_D C_G (W/L) V_G \exp(-s/V_G) \end{aligned} \qquad (2.7)$$

where C_G is the gate dielectric capacitance, W/L the width to length ratio, E_B is the energy barrier, and the mobility is thermal activated as:

$$\mu = \mu_0 \exp(-E_B / kT) \equiv_0 \exp(-s / V_G)$$
$$s = \frac{q^3 N_t^2 t}{8\varepsilon kTC_G} \qquad (2.8)$$

where q is the electronic charge, N_t is the density of traps at the grain boundaries, t is the semiconductor thickness, and ε is the dielectric constant of the semiconductor (usually taken as 4 for most of the organic semiconductors). The parameter s is the slope of the Levinson plot, and provides an estimate of the grain boundary charge, and of the density of charge traps at the grain boundaries.

2.1.4 Poole-Frenkel

The influence of charge trapping can be neutralized by increasing the charge carrier density. When a trap state is filled by a charge carrier, it becomes no longer active for another charge carrier; therefore, it can freely flow. This phenomenon generally leads to obtain a field effect dependent mobility and was described by Pool-Frenkel model. Considering the longitudinal field caused by the source/drain voltage $(E_L=V_{DS}/L)$ we obtain:

$$\mu(E) = \mu(0) \exp\left(\frac{-q(\phi_B - \sqrt{qE_L / \pi\varepsilon})}{kT} \right) \qquad (2.9)$$

where, $\mu(0)$ is the mobility when the applied field zero, q is the elementary charge (1.602 x 10^{-19}C), Φ_B is the trap depth, and ε is the semiconductor permittivity. This causes a non linear dependence of the current flowing from source to drain in the linear region. The ionization energy $q\Phi_B$ can be found by studying the activation energy $E_A=q[\Phi_B-(qE_L/\pi\varepsilon)^{1/2}]$ as a function of temperature and voltage [2, 11].

2.1.5 Contact Resistance

Measuring semiconductor mobility in a FET is a common way to derive conductivity properties of organics. Nevertheless, it should never be neglected that material properties strongly influence but do not coincide indeed with the device properties. In other words, the structural effect of the device itself, meant as e.g. parasitic effects that can be recorded on the electrical curves, should be carefully studied and possibly eliminated.

Recently a lot of efforts have been addressed towards the estimation and the reduction of the contact resistance for OFETs. Until some years ago this issue was underestimated since the OFETs performances were mostly limited by channel resistance effects. Nowadays, the performance of OFETs transistors has dramatically improved and the constant increase in the measured field effect mobilities led contact resistance effects to be a limiting factor for OFETs performances. Several methods have been developed for the extraction of the contact resistance in OFETs. In Figure 2.4 some possible equivalent circuits are depicted. One is composed only by the device, in the second case, series resistances have been added at the source and drain electrodes.

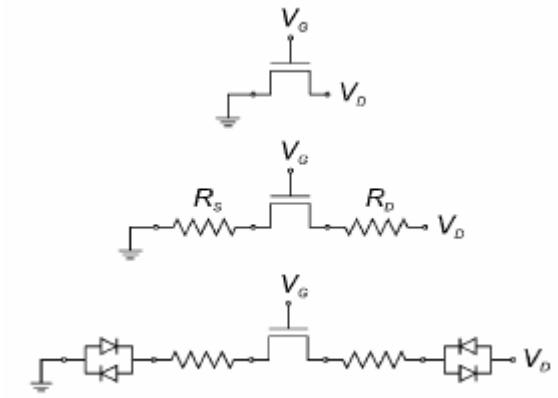

Figure 2.4: Equivalent circuit of the TFT without (top) and with (middle) contact resistances. The bottom circuit includes diode to account for non-linearity in the contact resistance [1].

A more complicated equivalent circuit was introduced by Necliudov et al., see the bottom circuit depicted in Figure 2.4, where also two diodes, which should take account of non linearities, are added [1, 12, 13]. The model introduced by Necliudov et al. takes also account of charge trapping within the organic semiconductor film, which is modelled by considering gate voltage dependent field effect mobility:

$$\mu=\mu_0(V_G-V_T)^{\gamma} \qquad (2.10)$$

where, V_T is the threshold voltage and μ_0 and γ are two empirical parameters. The contact resistance is accounted by introducing a voltage drop $R_S I_D$, where R_S is the contact resistance; therefore, the drain voltage will be replaced by $(V_D-R_S I_D)$

$$I_D = Z/L\mu C_{ins}(V_G - V_{th})(V_D - R_S I_D) \qquad (2.11)$$

$$g_D = \left(\frac{1}{\mu(W/L)C_{ins}(V_{GS} - V_T)} + R_S \right)^{-1} \qquad (2.12)$$

$$R_{total} = R_s + \frac{L}{W\mu C_{ins}\left| (V_{GS} - V_T) \right|} \qquad (2.13)$$

if we consider the model introduced by Necliudov described in eq. 2.10 we obtain a more complicated model given by:

$$g_D = \left(\frac{1}{\mu(W/L)C_G(V_{GS} - V_T)^{1+\gamma}} + R_S \right)^{-1}$$
$$\frac{1}{g_D} = R_D = \frac{L}{W\mu_0 C_{ins}(V_{GS} - V_T)^{1+\gamma}} + R_S \qquad (2.14)$$

More recently, several groups employed a different technique to estimate the Contact Resistance. One of the most used methods is called Trasmission Line Method (TLM) [14-16]. This method, which was

firstly developed for amorphous thin film transistors, consists in measuring the channel length dependence of the total resistance of the device. In fact, the total resistance of a FET (namely, R_T) is given by the sum of the contact resistance plus the channel resistance:

$$R_T=R_S+R_{Ch} \qquad (2.15)$$

If several devices, with different channel length are realized on the same substrate and with the same active layer, it can be assumed that the contact resistance for all these devices is constant, since it is independent from the channel length of the device. As a result, if we plot the total device resistance as a function of the channel length, its extrapolation to zero channel length (where the channel resistance is equal to zero) should give the value of the Contact Resistance.

This method is highly diffused but it has also some problems. While measuring several devices we cannot be sure that the contact resistance or the channel resistance does not vary from sample to sample. Therefore, when plotting the total resistance as a function of the channel length, scattering can appear and data can be not strictly aligned. An alternative method, called four probe measurements, would avoid these problems. This method consists of introducing in the conducting channel two additional electrodes. Since the current through the channel is imposed by the source and drain voltage, the voltage drop between these two electrodes should not be affected by contact resistance and the real channel resistance can be then estimated by the ratio between the voltage drop, estimated between the two additional electrodes, and the current flowing from source to drain.

2.2 OFETs architectures

For more than a decade now, organic field effect transistors (OFETs) based on conjugated polymers, oligomers, or other molecules

have been envisioned as a viable alternative to more traditional, mainstream thin-film transistors (TFTs) based on inorganic materials. Because of the relatively low mobility of the organic semiconductor layers, OFETs cannot rival the performance of field-effect transistors based on single-crystalline inorganic semiconductors, such as Si and Ge, which have charge carrier mobilities (μ) about three orders of magnitude higher [1]. Consequently, OFETs are not suitable for use in applications requiring very high switching speeds. However, the processing characteristics and demonstrated performance of OFETs suggest that they can be competitive for existing or novel thin-film-transistor applications requiring large-area coverage, structural flexibility, low-temperature processing, and, especially, low cost. The first examples of OFETs were assembled on silicon. In fact, the only organic part of such devices was the active layer, which was realized employing an organic semiconductor instead of an inorganic one. The basic structures consist in the typical TFT configuration largely employed for the realization of field effect transistors with amorphous silicon. A highly doped silicon wafer was used both as mechanical substrate and as gate electrode. On the top of it a thin SiO_2 layer (typically from 50 to 500 nm. thick) is grown in order to obtain the gate dielectric. From this point we can then start for assembling the final device.

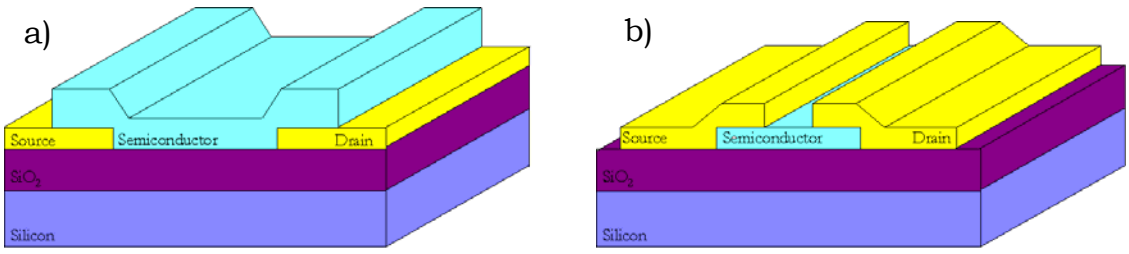

Figure 2.5: Schematic of OFETs in bottom contact (a) and top contact (b) configuration.

For this purpose two electrodes and a semiconductor layer are needed. In Figure 2.5 we show the two most common configurations: namely, bottom contact (BC) and top contact (TC). The difference between these two architectures is that in the BC transistors the organic semiconductor layer is deposited after the patterning of the source and drain electrodes. In the TC configuration the active layer is deposited in advance on the bare silicon dioxide surface and the source and drain electrodes are patterned afterwards onto the organic semiconductor film.

2.2.1 OFETs on Mylar®

As already mentioned in the previous sections, the first examples of OFETs were assembled on a highly doped silicon wafer, acting as gate electrode, with a thin silicon dioxide layer employed as gate dielectric. Nevertheless, over the past few years, several examples of OFETs assembled on plastic substrates were developed. In our lab we developed a different structure that allowed to obtain fully flexible and transparent OFETs. The core of the structure is a poly(ethyleneterephtalate) foil (namely, Mylar®, DuPont) with thicknesses ranging from 0.9 to 1.6 μm, which acts at the same time as gate dielectric and as mechanical support for the final device. This material is characterised by a dielectric constant similar to that of SiO_2 ($k_e \approx 3.0$), high resistivity (surface resistivity 10^{16} Ohm/sq) and low permeability to oxygen, hydrogen, water and CO_2 [17]. Moreover, due to its mechanical properties, it can be used as a flexible mechanical support for the realization of completely flexible electronic devices. After the assembly, such patterned film can be applied to any kind of substrate allowing, on one hand, to access to unusual applications (substrates as soft as paper or fabric or 3D surfaces can be used) and, on the other hand, to protect the organic semiconductor from the contact with atmosphere, without the constraints of top gate structures.

Completely flexible and transparent devices, such as organic field effect transistors, light emitting transistors and field effect chemosensors can be realized by employing this kind of structure [18-20].

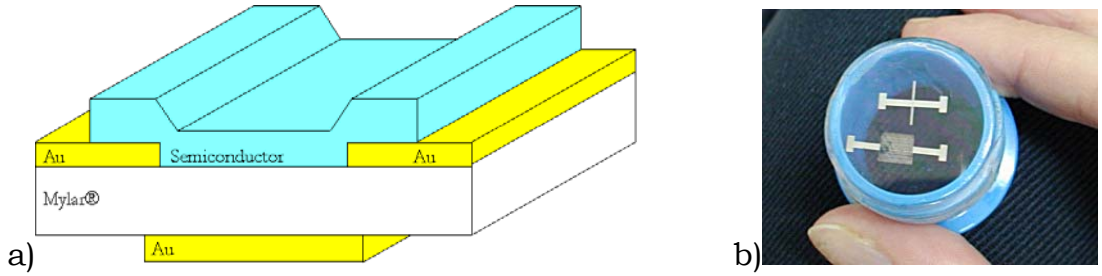

Figure 2.6: structure of a OFET assembled on Mylar® (a); picture of the final device showing the transparency of the structure (b).

The first step for the realization of an OFET on Mylar® is the assembly of the plastic foil on a circular frame in order to obtain a flat surface. Before patterning the electrodes and depositing the organic semiconductor, the structure is cleaned with acetone, isopropanol and deionised water and dried with a nitrogen flux. Source and drain electrodes are usually realized in Au and patterned, either by shadow mask deposition or by photolithography, on the upper side of the Mylar® foil; whereas the gate electrode is realized on the opposite side of the foil by depositing a thin Au layer evaporated through a shadow mask. All details concerning these patterning procedures will be given in the following sections. All the organic semiconductors employed in this thesis were deposited via thermal evaporation from resistively heated Al_2O_3 or W crucibles in a custom-made vacuum chamber (base pressure from $5x10^{-5}$ to 5×10^{-8} mbar). The amount of deposit and the evaporation rate were monitored by a quartz crystal microbalance placed next to the substrate, see Figure 2.8.

Most work developed in this thesis concerns the realization of all organic FETs. For these devices, all the electrodes were realized employing a conductive polymer (PEDOT:PSS, introduced in Chapter 1)

instead of Au. To this aim, a different patterning technique was employed, namely Soft Lithography MicroContact Printing. In the following sections of this chapter a detailed description of the basic principles of such technique will be given, while all the procedural steps for the assembling of an all organic FETs on Mylar® will be introduced in details in Chapter 4.

2.3 Fabrication techniques

The following sections are dedicated to the description of the technologies usually employed for the fabrication of OFETs. In particular the organic semiconductor deposition and the patterning of the metal electrodes will be described.

2.3.1 Organic Semiconductor deposition

The technique employed for depositing the organic active layer usually depends on the solubility of the material we are using. If the material is soluble, it is generally deposited in thin films by a spin coating process, otherwise, it is deposited by means of thermal evaporation.

2.3.1.1 Spin Coating

Spin coating is a procedure used to apply uniform thin films to flat substrates. A certain amount of the material in solution is placed on the substrate, which is then rotated at high speed in order to spread the fluid by centrifugal force. A machine used for spin coating is called spin coater, or simply spinner. Rotation is continued while the fluid spins off the edges of the substrate, until the desired thickness of the film is achieved. The applied solvent is usually volatile, and simultaneously evaporates. So, the higher the angular speed of spinning, the thinner the film. The thickness of the film also depends on the concentration of the solution and the employed solvent.

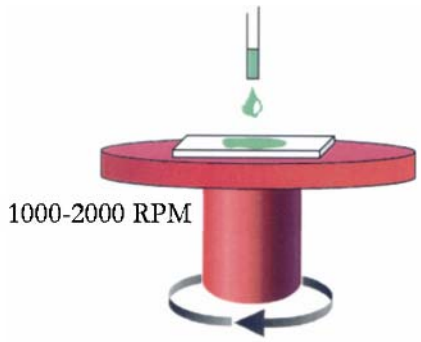

Figure 2.7: Schematic representation of the spin coating process.

2.3.1.2 Thermal Evaporation

This technique is generally used when the employed organic material is not soluble. In this thesis, we used small molecules that are characterized by a very low degree of solubility, therefore, in all our experiments the organic active layers were deposited by means of thermal evaporation. This deposition takes place inside a High Vacuum Chamber, with a nominal pressure ranging form $5x10^{-5}$ to $5x10^{-8}$ mbar.

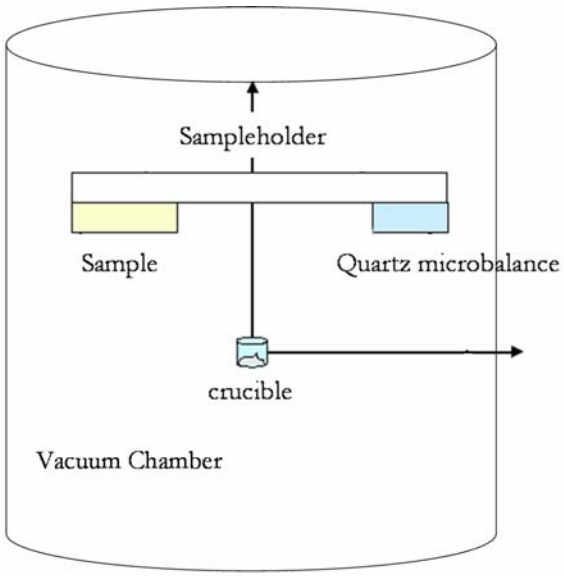

Figure 2.8: Schematic representation of the thermal evaporation system.

The organic material is located inside a crucible wrapped by a high resistive wire, usually made out of tungsten, connected to two electrodes. The crucible can be resistively heated up by applying a bias to the two electrodes until the temperature needed to let the organic material start evaporating. The evaporator system is usually provided with a Crystal Quartz Microbalance used to measure the nominal thickness of the deposited film. In this way it is possible to control in a very efficient way the deposition rate and the final thickness, two parameters which are very important for the optimization of the electrical behaviour of the final assembled devices.

2.3.2 Patterning of the electrodes

In most cases, the source and drain electrodes are realized with metals (i.e. Au, Al, Ag etc…), and are usually patterned by means of a photolithographic process followed by an etching procedure, which will be described in details in the next section. These procedural steps are not suitable for the realization of top contact devices, since the organic materials are very sensible to external agents and the solvents and the etchant can pollute it. For the patterning of the source and drain electrodes a shadow mask is generally used. The procedure consists in interposing a shadow mask between the sample and the source of the metal flux, as depicted in Figure 2.9. As a consequence, the regions where the metal is deposited are selected by the shadow realized by the mask. The limit of such technique consists in the poor highest reachable resolution. It is not possible to realize high resolution shadow masks and the typical features are in the range of 100μm, therefore, this technique is not suitable for the realization of devices with channel length in the order of the micrometer.

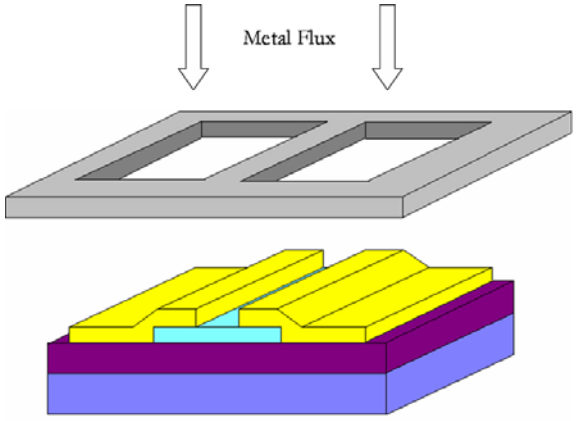

Figure 2.9: Schematic illustration of the procedure for the realization of top contact electrodes by means of a shadow mask.

2.3.3 Photolithography

Photolithography is a very common technique widely used in the Semiconductor industry for the patterning of the devices. The goal of this technique is to transfer a certain pattern on a substrate. For this purpose two elements are required: i) a mask which reproduces the image to transfer on the substrate and it must be opaque to ultraviolet light; ii) a photosensitive material, called photoresist, which is exposed to ultraviolet light during the process by interposing the mask between the UV source and the surface. There are two types of resists, namely, positive and negative photoresist. Positive resist is 'softened' by exposure to the Ultra-Violet (UV) light and the exposed areas are subsequently removed in the development process, the resist image will be identical to the opaque image on the mask. Negative resist is 'hardened' by exposure to ultra-violet light and therefore it is the unexposed areas that are removed by the development process, the resist image will be a negative image of the mask. Photoresists are sensitive to a wide range of wavelengths of light, typically 200 - 500 nm, this range of wavelengths includes the visible blue and violet contained in normal white light. For this reason, photolithography fabrication

areas use a special filtered light to remove all of the wavelengths to which the resist is sensitive.

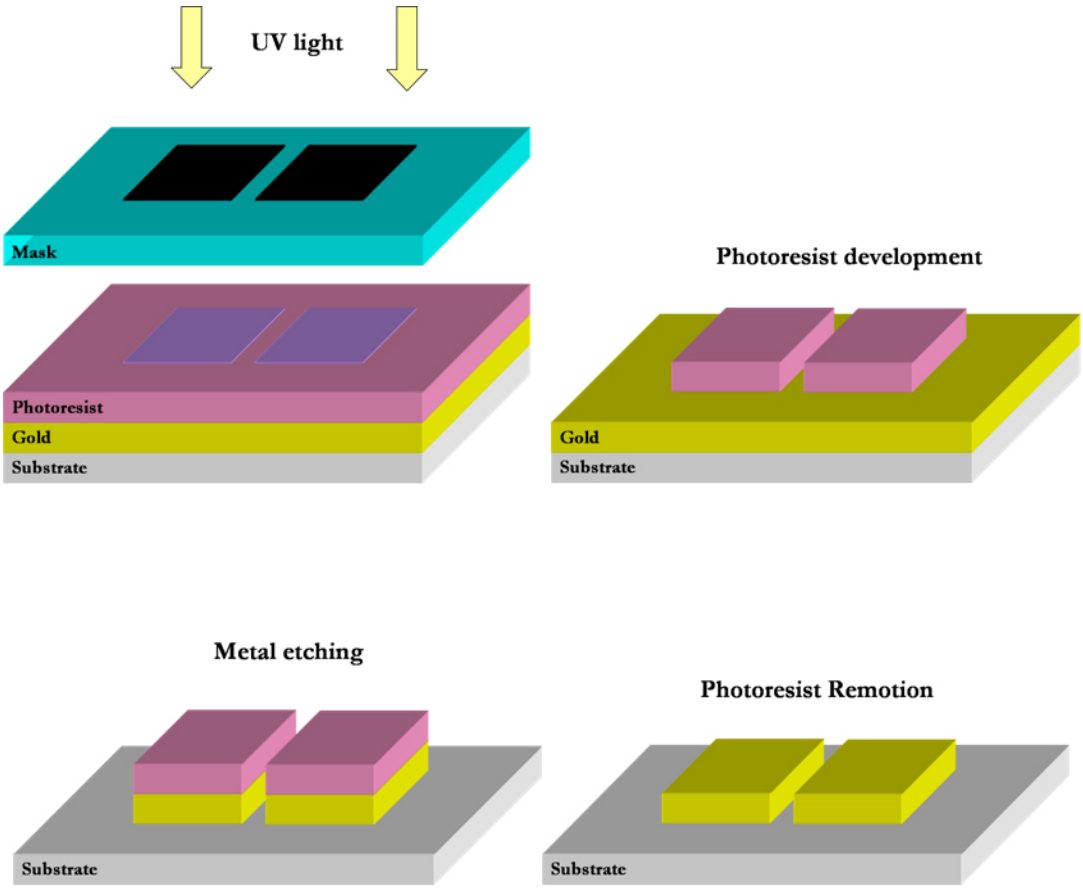

Figure 2.10: Schematic representation of the main steps required in a photolithographic process.

In Figure 2.10 we show the main steps required in a photolithographic process. In particular, we show the steps required for the patterning of the OFET structures we employed during this thesis. First of all, a thin metal film is deposited over the surface. In our case, we deposited a thin gold film, deposited by thermal evaporation, over the Mylar® surface. Afterwards, a thin positive photoresist film is deposited onto the sample surface; generally this process is made by spin coating. Before the exposure process, a soft baking process of the sample is usually required in order to dry the deposited photoresist

film. During the exposure process, the photoresist layer is exposed to UV light through the opaque mask; in this way it is possible to define the pattern on the resist film. After exposure, the sample is developed in order to remove the unwanted resist, thus leaving only the define pattern on the substrate. Usually, a post baking step is made to increase resist adherence with the substrate and in particular to increase its resistance to etch process. Taking advantage of the presence of the patterned resist film, it is then possible to etch the metal in the undesired areas. Once the etching process is performed we can remove the photoresist by using an organic solvent, generally acetone, and the basic structure for the realization of the final device is assembled [21].

2.3.4 Soft Lithography: Overview

"Soft lithography represents a non-photolithographic strategy based on selfassembly and replica molding for carrying out micro- and nanofabrication. It provides a convenient, effective, and low-cost method for the formation and manufacturing of micro- and nanostructures. In soft lithography, an elastomeric stamp with patterned relief structures on its surface is used to generate patterns and structures with feature sizes ranging from 30 nm to 100 μm." [22]

"Soft lithography" is a new high resolution patterning techinque developed at Harvard by Prof. George Whitesides. The key element in Soft Lithography is an elastomeric stamp with patterned relief structures on its surface. Usually the stamp is made out of elastomeric polymers, as polyurethane, polyimide, and cross linked Novolac™ resin [23], but the most used material is poly(dimethylsiloxane) (PDMS). This material has very low glass transition temperature and it is liquid at room temperature, moreover, it can be easily and quickly convert into solid upon a cross-linking process [24]. In this thesis Sylgard™ 184 obtained from Dow Corning was used. The provided kit consists in two

part: a liquid silicon rubber base (i.e. a vinyl-terminated PDMS) and a catalyst or curing agent i.e. a mixture of a platinum complex and copolymers of methylhydrosiloxane and dimethylsiloxane). Once mixed, poured over a certain master, and heated to elevated temperatures, the liquid mixture becomes a solid, cross-linked elastomer in a few hours via the hydrosilylation reaction between vinyl ($SiCH=CH_2$) groups and hydrosilane (SiH) groups [24]. In Figure 2.11 the main steps for the realization of PDMS rubber stamp are shown. The starting point is the realization of a master, typically made on silicon. The master is fabricated using microlithographic techniques such as photolithography, micromachining, e-beam writing [25, 26], and should reproduce the negative of the pattern desired to be transferred.

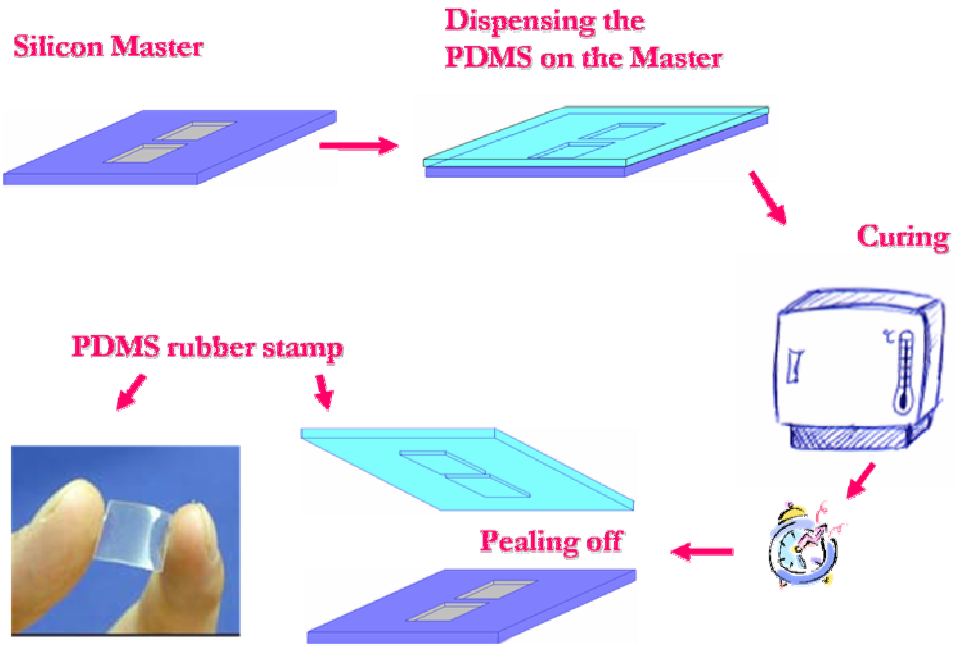

Figure 2.11: Main steps required for the realization of a PDMS rubber stamp. The final stamp reproduces the features of the electrodes to be transferred onto the substrate.

The procedural steps for the realization of an elastomeric stamp are very easy; once the PDMS is mixed with its curing agent, the mixture is dispensed over the master. The following step is a thermal

curing procedure that will lead the blend film to become a solid, cross-linked elastomer via the hydrosilylation reaction between vinyl ($SiCH=CH_2$) groups and hydrosilane (SiH) groups.

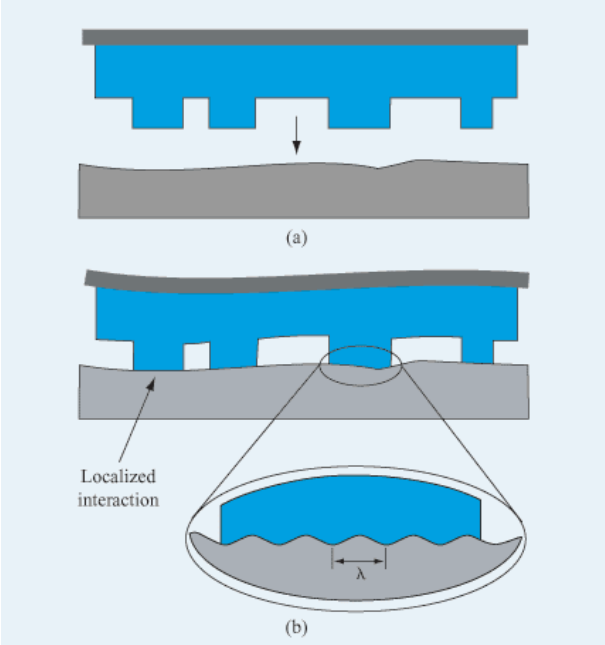

Figure 2.12: Conformal contact between a hybrid stamp and a hard substrate. (a) Stamp composed of a patterned elastomer and a flexible backplane adapts its protruding zones to (b) the macroscopically uneven substrate and (b, inset) its microscopic roughness, whereas recessed zones do not touch the substrate.

After thermal processing, the PDMS stamp can be pealed off and will consist of a fully flexible and transparent elastic stamp reproducing the negative of the master pattern. The possibility to realize micro and nano-structures by means of this technique relies in the intrinsic property of PDMS elastomer to form a conformal contact with the surface which it has been brought into contact to.

"Conformal contact comprises 1) the macroscopic adaptation to the overall shape of the substrate and 2) the microscopic adaptation of a soft polymer layer to a rough surface, leading to an intimate contact without voids, see Figure xx. Adhesion forces mediate this elastic adaptation, and even without the application of external pressure, an elastomer can

spontaneously compensate for some degree of substrate roughness, depending on the materials properties ".[27, 28]

Several different techniques are known collectively as soft lithography. We report below the most important:

- *Near-Field Phase Shift Lithography*. A transparent PDMS phase mask with relief on its surface is placed in conformal contact with a layer of photoresist. Light passing through the stamp is modulated in the near-field. If the relief on the surface of the stamp shifts the phase of light by an odd multiple of λ, a node in the intensity is produced. Features with dimensions between 40 and 100 nm are produced in photoresist at each phase edge.
- *Replica Molding*. A PDMS stamp is cast against a conventionally patterned master. Polyurethane is then molded against the secondary PDMS master. In this way, multiple copies can be made without damaging the original master. The technique can replicate features as small as 30 nm.
- *Micromolding in Capillaries (MIMIC)*. Continuous channels are formed when a PDMS stamp is brought into conformal contact with a solid substrate. Capillary action fills the channels with a polymer precursor. The polymer is cured and the stamp is removed. MIMIC is able to generate features down to 1 μm in size.
- *Microtransfer Molding*. A PDMS stamp is filled with a prepolymer or ceramic precursor and placed on a substrate. The material is cured and the stamp is removed. The technique generates features as small as 250 nm and is able to generate multilayer systems.
- *Solvent-assisted Microcontact Molding (SAMIM)*. A small amount of solvent is spread on a patterned PDMS stamp and the stamp is placed on a polymer, such as photoresist. The solvent swells the

polymer and causes it to expand to fill the surface relief of the stamp. Features as small as 60 nm have been produced [29].

2.3.5 MicroContact Printing (μCP)

It is probably the most known and used soft lithographic technique. In this section we describe it more in details, since it has been widely employed during this thesis for the patterning of all organic FETs. The basic application or at least the most used one, of μCP concerns using as "ink" Self Assembled Monolayers (SAMs) to be transferred onto the surface of a substrate by contact. In details, an "ink" of alkanethiols is spread on a patterned PDMS stamp. The stamp is then brought into contact with the substrate, which can range from coinage metals to oxide layers. The thiol ink is transferred to the substrate where it forms a self-assembled monolayer that can act as a resist against etching.

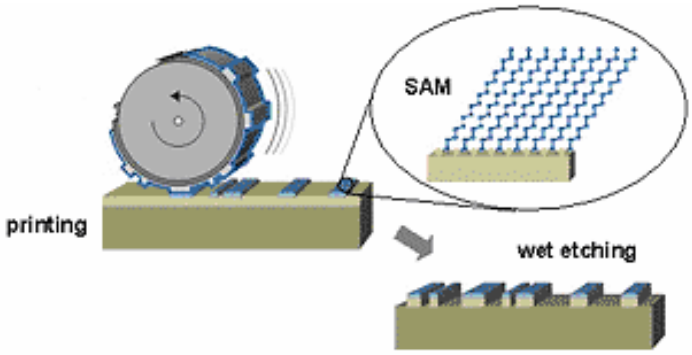

Figure 2.13: μC printing of alkanethiols employed as protective mask during the wet etching procedure for the patterning of the metal electrodes.

Features as small as 300 nm have been made in this way [23]. Although these *mono*layers do only have a *thickness* corresponding to the length of just *one ink molecule*, which typically has a longer axis of about 2-3 nm, they are very stable and resistant against chemical and physical stresses during processing. This makes them ideal as etch resists in a photo-mask-free process. In the same way it is possible to

use also other molecular “inks” instead of alkanethiols. As will be describe in details in Chapter 4, we used μCP to pattern Source and Drain electrodes by employing the conducting polymer PEDOT:PSS as “ink” to be transferred onto the gate dielectric surface. With this technique it was possible to realized all organic FETs either in Bottom Contact and Top Contact configurations with very good performances.

References

[1] G. Horowitz, J. Mater. Res., 1946 (2004).

[2] S. M. Sze, Physics of Semiconductor Devices (Wiley, New York, 1981).

[3] T. B. Singh, F. Meghdadi, S. Günes, N. Marjanovic, G. Horowitz, P. Lang, S. Bauer, N. S. Sariciftci, 17, 2315 (2005).

[4] Y. Sun, Y. Liu, Y. Ma, C. Di, Y. Wang, W. Wu, G. Yu, W. Hu, and D. Zhu, Appl. Phys. Lett., 88,242113 (2006).

[5] J. Puigdollers, C. Voz, A. Orpella, R. Quidant, I. Martin, M. Vetter, R. Alcubilla, Org. Electr. 5, 67 (2004).

[6] Y. Jang, Y. D. Park, J. A. Lim, H. S. Lee, W. H. Lee, and Ki. Cho, Appl. Phys. Lett., 89, 183501 (2006).

[7] H. Sirringhaus, T. Kawase, R. H. Friend, T. Shimoda, M. Inbasekaran, W. Wu, E. P. Woo, Science, 290, 2123 (2000).

[8] A. Rolland, J. Richard, J. P. Kleider and D. Mencaraglia, J. Electrochem. Soc. 140, 3679 (1993).

[9] R. A. Street, D. Knipp and A. R. Volkel, Appl. Phys. Lett., 80, 1658 (2002).

[10] J. Levinson, F. R. Sheperd, P. J. Scanion, W. D. Weswood, G. Este, and M. Rider, J. Appl. Phys. 53, 1193 (1982).

[11] P. Stallinga, H. L. Gomes, F. Biscarini and M. Murgia, D. M. de Leeuw, J. Appl. Phys., 96, 5277 (2004).

[12] G. Horowitz, P. Lang, M. Mottaghi, and H. Aubin, Adv. Funct. Mater. 14, 1069 (2004).

[13] P.V. Necliudov, M.S. Shur, D.J. Gundlach, and T.N. Jackson, J. Appl. Phys. 88, 6594 (2000).

[14] P. V. Necliudov, M. S. Shur, D.J. Gundlach, and T.N. Jackson, Solid State Electron. 47, 259 (2003)

[15] H. Klauk, G. Schmid, W. Radlik, W. Weber, L. Zhou, C. D. Sheraw, J. A. Nichols, and T. N. Jackson, Solid State Electron 47, 297 (2003).

[16] J. Zaumseil, K. W. Baldwin, J. A. Rogers, J. Appl. Phys. 93, 6117 (2003).

[17] http://www.dupontteijinfilms.com.

[18] A. Bonfiglio, F. Mameli and O. Sanna, Appl. Phys. Lett. 82, 3550 (2002).

[19] C. Santato, I. Manunza, A. Bonfiglio, F. Cicoria, P. Cosseddu, R. Zamboni and M. Muccini Appl. Phys. Lett. 86, 141106 (2005).

[20] A. Loi, I. Manunza and A. Bonfiglio, Appl. Phys. Lett. 82, 103512 (2005).

[21] http://eserver.bell.ac.uk.

[22] Y.n Xia and G. M. Whitesides, Annu. Rev. Mater. Sci. 28, 153 (1998).

[23] A. Kumar, G. M. Whitesides, Appl. Phys. Lett. 63, :2002 (1993).

[24] Clarson SJ, Semlyen JA, (eds. 1993) Siloxane Polymers. Englewood Cliffs, NJ: Prentice Hall.

[25] R. F. W. Pease, J. Vac. Sci. Technol. B, 10, 278 (1992).

[26] F. Cerrina , C. Marrian , Mater. Res. Soc. Bull. XXI, 12, 56 (1996).

[27] A. Bietsch and B. Michel, J. Appl. Phys. 88, 4310 (2000).

[28] B. Michel, A. Bernard, A. Bietsch, E. Delamarche, M. Geissler, D. Juncker, H. Kind, J.-P. Renault, H. Rothuizen, H. Schmid, P. Schmidt-Winkel, R. Stutz, H. Wolf, IBM J. RES. & DEV. 45, 697 (2001).

[29] http://www.wtec.org/loyola/nano/US.Review.

Chapter 3

Characterization techniques

The most important problems that strongly influence electrical performances in organic transistors are charge carriers accumulation and transport across the channel and, not less important, charge carrier injection into the channel. The first problem is generally correlated to the morphological and structural properties of the deposited organic film. Organic films are generally characterized by very poor degree of crystallinity, and charge transport is dramatically limited by charge carrier scattering at the grain boundaries. For this issue it is useful to investigate, on one side, the topographical properties of the film showing how the film is assembled in a large scale, and, on the other side, the way the molecules are packed and oriented on a very small scale. Charge carrier injection into the channel is more correlated to the interfacing between metal electrodes and the organic semiconductor. In fact, it should strongly depends on the energy level matching between the Fermi-level of the source and drain electrodes and the organic semiconductor energy levels, i.e, the transport levels derived from the lowest unoccupied molecular orbital (LUMO) and highest occupied molecular orbital (HOMO). One of the fundamental aspects of the metal/semiconductor interface is the Fermi level alignment, described by the Mott-Schottky model, nevertheless, there

are several aspects that can modify the Mott-Schottky-type of band bending and, as a consequence, cause a drift from the ideal behaviour. For these reasons, this chapter is focussed on the description of the characterization techniques we used during this thesis in order to correlate structural and morphological properties of materials to device performance. In the first part, we describe the techniques employed for the structural and morphological characterization of materials, whereas the second part is dedicated to the description of the techniques we used for the electrical characterization of the assembled devices.

3.1 Materials characterization

As already mentioned, the electrical performances can be strongly influenced by several factors as, molecular packing and island nucleation within the organic film, and, not less important, interfacial phenomena which can take place at the metal/semiconductor interface. For these reasons, a set of techniques that allow to investigate structural and morphological properties of the materials on different size scale are required. The following sections are dedicated to the techniques employed during this thesis, namely, Atomic Force Microscopy, X-Ray Diffraction, X-Ray Photoemission spectroscopy, Photocurrent Spectroscopy and Electrical Characterization of OFETs by means of a semiconductor parameter analyzer.

3.1.1 Atomic Force Microscopy (AFM)

Within the past decades, a family of powerful surface imaging techniques, known collectively as scanned probe microscopy (SPM), has developed in the wake of the invention of the scanning tunneling microscope (STM). Scanning probe microscopes include a very broad range of instruments used to image and measure properties of material surfaces. The first two examples of SPMs are Scanning Tunneling Microscope (STM) and Atomic Force Microscope (AFM). STM was first

developed in1982 at IBM labs by Binning et al. [1], and the invention of this technique (for which Binning and Rohrer were awarded with the Nobel Prize in Physics in 1986) has had a great impact on the scientific community by providing a new tool to advance fundamental science and technology [2]. SPMs techniques basically consist in using a very sharp tip positioned within a few nanometers above the surface of interest to investigate the properties of such surface by analysing the interaction between this one and the tip. The main differences among the different kinds of SPMs technique relies in the different physical phenomenon monitored through tip and sample interaction. AFM employs a sharp probe moving over the surface of a sample in a raster scan; the probe is a tip on the end of a cantilever which bends in response to the force between the tip and the sample. Since the cantilever obeys Hooke's law (F = - kx where F is the force, k is the cantilever elastic constant and x is the cantilever deflection) for small displacements, the interaction force between the tip and the sample can be easily measured by detecting the deflection of the cantilever. The motion of the probe across the sample surface is generated by piezoelectric ceramics.

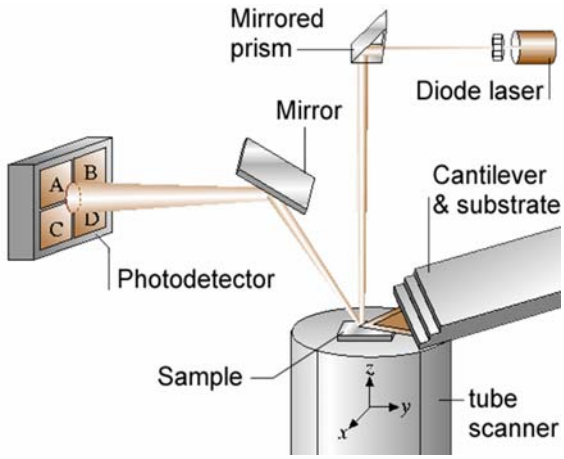

Figure 3.1: Atomic Force Microscope schematic.

3.1.1.1 Probe/Surface interactions

The strongest forces between probe and surface are mechanical; these are the forces that occur when the atoms on the probe physically interact with the atoms on a surface. However, other forces between the probe and surface can have an impact on an AFM image. These other forces include surface contamination, electrostatic forces, and surface material properties.

In ideal experimental conditions (e.g. in ultrahigh vacuum) when the cantilever tip approaches the sample surface, Van der Waals forces start acting upon it. They are sufficiently far-ranging and are felt at the distance of a few tens of angstroms. At the distance of several angstroms repulsive force starts acting. In real conditions (in ambient air) usually some humidity is present in air and a water layer is adsorbed on the sample and tip surfaces. When cantilever approaches sample surface the capillary force arises (Fig. 3.2) holding the tip in contact with the surface and increasing the minimum achievable interaction force. In addition, electrostatic interaction between the probe and the sample may appear rather often. This can be both attraction and repulsion.

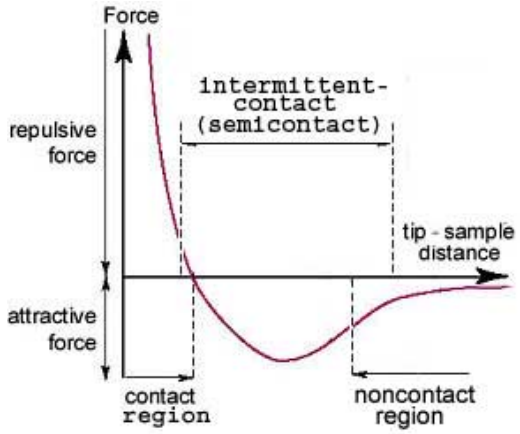

Figure 3.2: Interaction graph, showing the Force as function of tip-sample distance.

3.1.1.2 Interaction detection

Since the interaction between tip and surface can be measured by the bending of the cantilever upon the raster scan point by point, an efficient method to detect such phenomenon is required. Several techniques have been employed over the past years as for example *Tunnelling sensor* or *Interferometer sensor*. Nowadays, the most efficient and used one is the *Optical lever.* In this case, a laser beam is focused on the back surface of the cantilever, and the reflected beam is sent to a photodiode that is divided into four sections, as depicted in Figure 3.3. Due to the macroscopic length of the reflected light path, any deflection of the cantilever causes a magnified lateral displacement of the reflected laser spot on the photodiode. The relative amplitudes of the signals from the four segments of the photodiode change in response to the motion of the spot. Detection of deflections and torsions of less than 0.1 nm can be achieved.

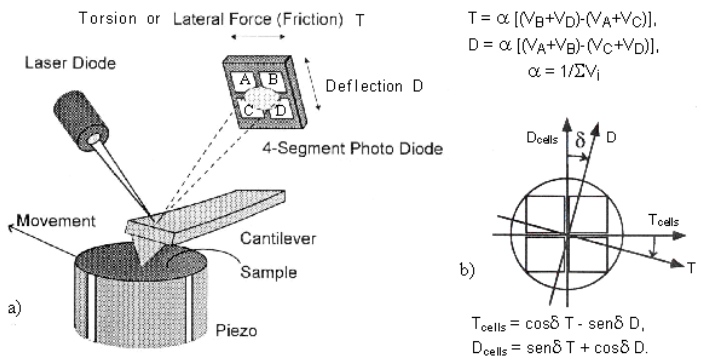

Figure 3.3: As the cantilever bends, the light from the laser is reflected onto the split photo-diode. By measuring the difference signal detected in the four segment, changes in the bending and torsion of the cantilever can be measured.

3.1.1.3 Working techniques: Contact mode

AFM can be used in different configuration; in particular, it can be used in *"contact"*, *"non-contact"* and *"semi-contact"* modes. In this section we introduced the most employed techniques in detail.

In Contact mode the cantilever deflection during scanning process reflects repulsive force and is used to detect the sample surface profile. Simultaneously with topography acquisition it is possible to detect some other characteristics of the investigated sample. If cantilever and tip are conductive one can detect the spreading resistance of the sample. If scanning is carried out in direction perpendicular to the longitudinal axis of cantilever (lateral direction) the friction force causes cantilever twisting. By measuring this twisting using position-sensitive four-sectional detector it is possible, simultaneously with topography, to imagine the friction forces distribution throughout sample surface. Typically, while working in contact mode, AFM can be used in two different configurations: *"constant height"* and *"constant force"*.

Constant Height Mode.

In this configuration the tip is brought and kept in direct physical contact with the sample surface during the raster scan. The tip is attached to the end of a cantilever with a low spring constant, lower than the effective spring constant holding the atoms of the sample together. As the scanner traces the tip across the sample (or the sample under the tip), the contact force leads the cantilever to bend to accommodate changes in topography. The cantilever deflection reflects, therefore, repulsive forces acting upon the tip. As the atoms are gradually brought together, they first weakly attract each other. This attraction increases until the atoms are so close together that their electron clouds begin to repel each other electrostatically. This electrostatic repulsion progressively weakens the attractive force as the inter-atomic separation continues to decrease. The force goes to zero

when the distance between the atoms reaches a couple of angstroms, about the length of a chemical bond. When the total Van der Waals force becomes positive (repulsive), the atoms are in contact. In AFM this means that when the cantilever pushes the tip against the sample, the cantilever bends rather than forcing the tip atoms closer to the sample atoms.

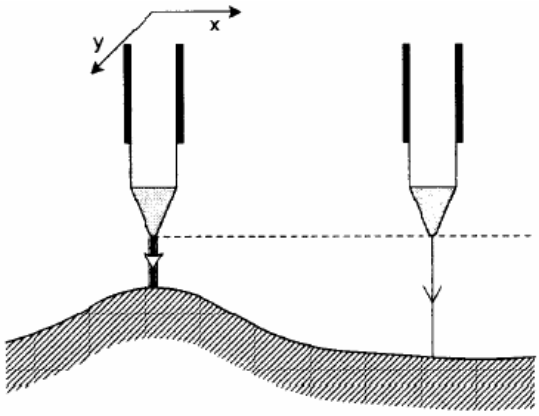

Figure 3.4: AFM working in constant height mode.

In this operation mode, after the tip has engaged the sample surface, the piezo-tube is left in the same z position (set point) over the entire scan across the selected area of interest. During the raster scan the interaction forces between tip and sample will locally change and lead the cantilever to bend due to the changes in the interaction forces. The image is formed by analysing the deflections of the cantilever detected in the four segment photodiode.

Constant Force Mode.

In this operative mode, the piezo-tube is free to move vertically during the scan over the sample. In this case it is the interaction force between tip and sample which is kept constant (set point); this means that the deflection of the cantilever during the scan shouldn't change. The constant position of the cantilever is kept constant thanks to a feedback circuitry which detect point by point the cantilever deflection and gives the required commands to the piezo-tube which will change is

vertical position (along z axis) in order to bring the cantilever deflection back to the imposed initial value. In this operative configuration the image is formed by analysing the changes, along its z axis, of the piezo-tube driven by the feedback system.

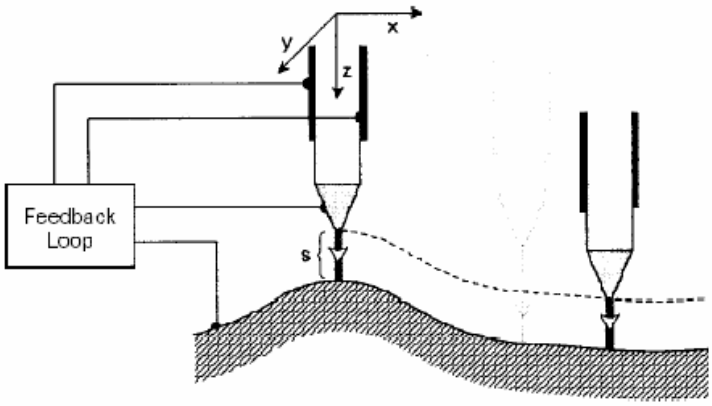

Figure 3.5: AFM working in constant force mode.

3.1.1.4 Non Contact Mode

The Non-Contact AFM (NC AFM), invented in 1987, offers unique advantages over other contemporary scanning probe techniques such as contact AFM and STM. The absence of repulsive forces (presenting in Contact AFM) in NC AFM allows to use it to investigate "soft" samples and, unlike the STM, the NC AFM does not require conducting samples. The NC AFM works via the principle "amplitude modulation" detection. The corresponding detection scheme exploits the change in the amplitude, A, of the oscillation of a cantilever due to the interaction of a tip with a sample. In the limit of small A, a cantilever approaching a sample undergoes a shift, Δf, in its natural frequency, f_o, towards a new value given by:

$$f_{eff} = f_o (1 - F'(z)/k_o)^{1/2} \qquad (3.1)$$

where f_{eff} is the new, effective resonance frequency of the cantilever of nominal stiffness k_o in the presence of a force gradient F'(z) due to the sample. The quantity *z* represents an effective tip-sample separation while $\Delta f = f_{eff} - f_o$ is typically negative, for the case of attractive forces. If cantilever is initially forced to vibrate at $f_{set} > f_o$, then the shift in the resonance spectrum of the cantilever towards lower frequencies will cause a decrease in the oscillation amplitude at f_{set} as the tip approaches the sample.

This change in *A* is used as the input to the NC-AFM feedback. To obtain a NC AFM image the user initially chooses a value A_{set} as the set-point such that $A_{set} < A(f_{set})$ when the cantilever is far away from the sample. The NC AFM feedback then moves the cantilever closer to the sample until its instantaneous oscillation amplitude, *A*, drops to A_{set} at the user-defined driving frequency f_{set}. At this point the sample can be scanned in the *x*–*y* plane with the feedback keeping $A = A_{set}$ = constant in order to obtain a NC AFM image. The NC AFM feedback brings the cantilever closer (on average) to the sample if A_{set} is decreased at any point, and moves the cantilever farther away from the sample (on average) if A_{set} is increased.

3.1.1.5 Semicontact Mode

Usage of Scanning Force Microscopy with oscillating cantilever was firstly anticipated by Binnig. Earlier experimental realizations of scanning with oscillated cantilever was realized in works [3, 4] where it was demonstrated the influence of the force gradients on the cantilever frequency shift and the possibility of non-contact scanning sample surface. In [3] was demonstrated also the possibility of materials sensing under abrupt decreasing of cantilever oscillation amplitude. Moreover, it was demonstrated the possibility of scanning sample surface not only in attractive but also in repulsive forces. Relatively small shift of oscillating frequency with sensing repulsive forces means

that contact of cantilever tip with sample surface under oscillation is not constant. Only during small part of oscillating period the tip "feels" contact repulsive force. Especially it concerns to oscillations with relatively high amplitudes. Scanning sample surface with cantilever oscillated in this manner cannot be defined as non-contact, but more exactly as intermittent contact. Corresponding mode of Scanning Force Microscope operation (Intermittent Contact mode or Semicontact mode) is in common practice. Moreover, “feeling” the contact repulsive forces under the scanning leads to the additional phase shift of cantilever oscillations relatively piezo-driver oscillations. This phase shift depends on the material characteristics. Recording the phase shift during scanning (Phase Contrast Imaging mode) is very useful for imaging of nano-structured and heterogeneous materials [5, 6].

3.1.2 X-Ray Diffraction (XRD)

X-ray diffraction is a very widely used crystallographic technique that allows to observe the structural properties of the investigated sample analysing the pattern produced by the diffraction of an incident x-ray radiation through the closely spaced lattice of atoms in a crystal. This generally leads to a detailed understanding of the molecular structure of the investigated material.

The crystal structure is studied using the diffraction of photons, neutrons and electrons. The diffraction depends on the crystal structure and on the wavelength. English physicists Sir W.H. Bragg and his son Sir W.L. Bragg developed a relationship in 1913 to explain why the cleavage faces of crystals appear to reflect X-ray beams at certain angles of incidence (theta, θ).

$$N\lambda=2d\sin(\theta) \qquad (3.2)$$

Where the variable *d* is the distance between atomic layers in a crystal, and *λ* is the wavelength of the incident X-ray beam; n is an integer. This observation is an example of X-ray wave interference, commonly known as X-ray diffraction (XRD), and was direct evidence for the periodic atomic structure of crystals postulated for several centuries.

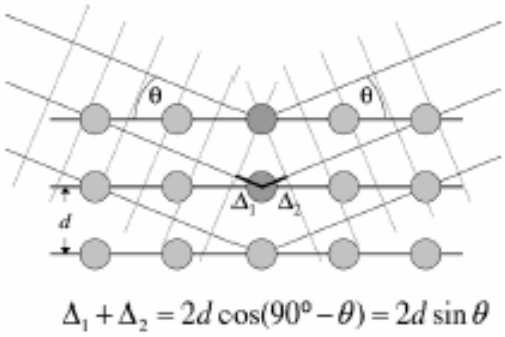

Figure 3.6: Visualization of the Bragg equation. Maximum scattered intensity is only observed when the phase shifts add to a multiple of the incident wavelength λ [7].

Therefore, when a monochromatic X-ray beam with wavelength λ is incident on lattice plane in a crystal at an angle θ, diffraction occurs only when the distance travelled by the rays reflected from successive planes differs by a complete number n of wavelengths. By varying the angle θ, the condition of Bragg law is satisfied by different d-spacing in polycrystalline materials. Plotting the angular position and intensities of the resultant diffraction peaks produces a pattern that is characteristic of the sample: this graph is called diffractogram. When a mixture of different phases is present, the diffraction is formed by the superposition of the individual patterns.

An often used instrument for measuring the Bragg reflection of a thin film is the θ/2 θ diffractometer. Since the scattering of x-rays depends sensitively on the orientation of the crystal with respect to the scattering vector, we must carefully define the various coordinate systems with which we are dealing. A sample reference frame { s_i} is

introduced for this purpose that is oriented with s_1 and s_2 in the plane of the thin film, while s_3 is equivalent to the surface normal.

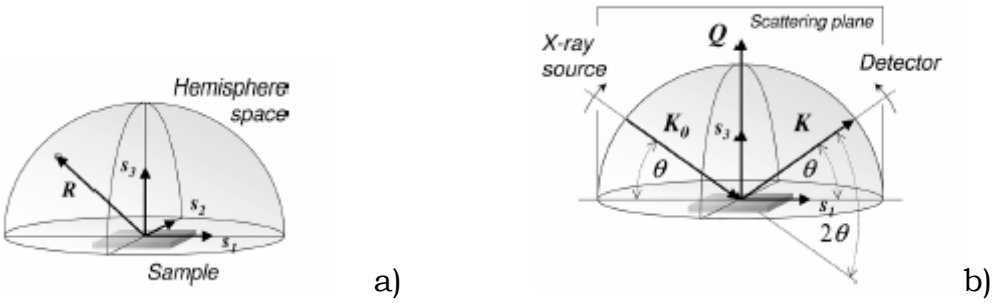

Figure 3.7: Sample reference frame $\{s_i\}$ and hemisphere above it (a); schematic representation of a θ/2θ scan from the viewpoint of the sample reference frame $\{s_i\}$ (b).

The working principle of a θ/2θ scan is visualized in Fig. 3.7 (b) in the hemisphere of the sample reference frame. The sample is positioned in the center of the instrument and the probing x-ray beam is directed to the sample surface at an angle θ. At the same angle the detector monitors the scattered radiation. The sample coordinate vectors s_1 and s_3 lie in the scattering plane defined by K_0 and K. The diffraction pattern is collected by varying the incidence angle of the incoming x ray beam by θ and the scattering angle by 2θ while measuring the scattered intensity I(2θ) as a function of the latter. Two angles have thus to be varied during a θ/2θ scan. Note that the angle convention is different from the one used in optics: in x-ray diffraction the angles of incoming and exiting beam are always specified with respect to the surface plane, while they are related to the surface normal in optics. The θ/2θ scan can also be understood as a variation of the exit angle when this is determined with respect to the extended incoming beam and this angle is 2θ for all points in such a scan. This is the reason for naming the measurement procedure a θ/2θ scan. The quantity measured throughout the scan is the intensity scattered into the detector. The results are typically presented as a function of I(2 θ) type. There exist

several diffractometer configurations. For one set of instruments, the x-ray source remains fixed while the sample is rotated around θ and the detector moves by 2θ. For other systems the sample is fixed while both the x-ray source and the detector rotate by θ simultaneously, but clockwise and anticlockwise, respectively. The rotations are performed by a so-called goniometer, which is the central part of a diffractometer. Typically the sample is mounted on the rotational axis, while the detector and/or x-ray source move along the periphery, but both axes of rotation coincide [7-14].

3.1.3 X-Ray Photoemission Spectroscopy (XPS)

Photoelectron Spectroscopy is a very versatile surface analytical technique with wide range of applications. It utilizes photo-ionization and energy-dispersive analysis of the emitted photoelectrons to study the composition and electronic state of the surface region of a sample. Traditionally, when the technique has been used for surface studies it has been subdivided according to the source of exciting radiation into:

1) X-Ray Photoelectron Spectroscopy (XPS) - using soft x-ray (200-2000 eV) radiation to examine core-levels.

2) UltraViolet Photoelectron Spectroscopy (UPS) - using UV radiation (10-45 eV) to examine valence levels.

XPS was developed in the mid 1960s by K. Siegbahn and his research group. K. Siegbahn was awarded the Nobel Prize for Physics in 1981 for his work in XPS. It is based upon a single photon in/electron out process. In this process, X-ray photons interact with inner shell electrons of an atom and lead transfer of energy from photon to the electron. This energy transfer makes it possible for the electrons to leave the atom and escape. These electrons are known as photoelectrons [15].

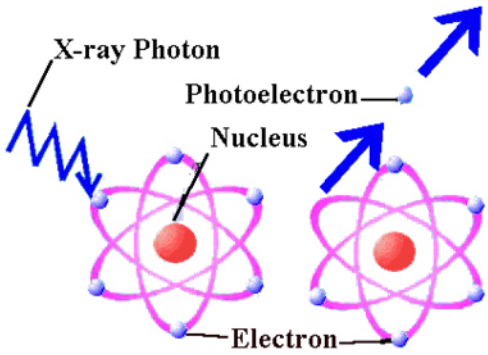

Figure 3.8: Photoelectron emission process.

As the energy of X-ray photon and the kinetic energy of escaped electron are known, binding energy of the inner shell electrons can be determined by the equation:

$$E_{binding} = E_{photon} - E_{kinetic} - \Phi \qquad (3.3)$$

$$E_{photon} = h\nu \qquad (3.4)$$

Where, $E_{binding}$ is the binding energy of the emitted electron, E_{photon} is the energy of the incident X-ray photon, $E_{kinetic}$ is the kinetic energy of the emitted electron, Φ is the work function of the spectrometer, h is Plank constant and ν is the frequency of the incident x-ray photon.

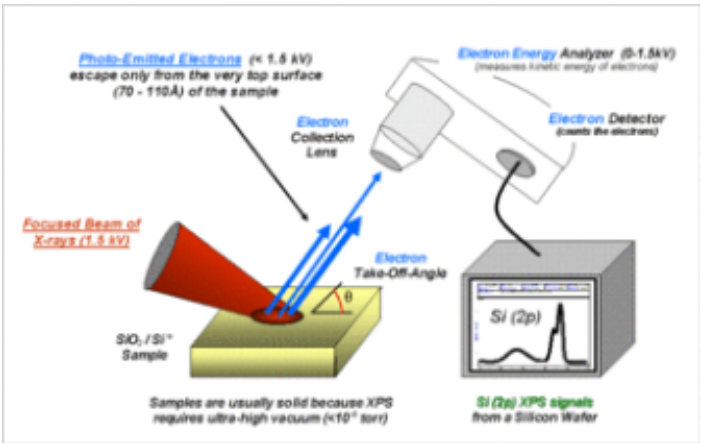

Figure 3.9: Schematic of a typical XPS system.

A typical XPS spectra is a plot of the number of electrons detected (Y axis) versus its binding energy (X axis). For each chemical element, there will be a characteristic binding energy associated with each core atomic orbital. Each element produces a characteristic set of peaks corresponding to the electronic configuration of the electrons within the atoms, e.g. 1s, 2s, 2p, 3s etc... The presence of peaks at particular energies therefore indicates the presence of a specific element in the sample under study. Furthermore, the intensity of the peaks is related to the concentration of the element within the sampled region. Thus, the technique provides a quantitative analysis of the surface composition and therefore is sometimes known with an alternative acronym, ESCA (Electron Spectroscopy for Chemical Analysis).

After a photoelectron has been ejected from inner shell of an atom, the excited atom can relax by two different mechanisms. The hole created by the ejection of photoelectron can be filled by an electron from an outer shell, releasing energy which can be released as a quantum of X-ray or the energy can be given to another electron in same level or a lower level and that can be ejected. These electrons are known as Auger electrons. The process of ejection of photoelectrons is known as X-ray fluorescence and the relaxation of atoms by the emissions of Auger electrons is known as Auger emission. For low atomic number elements ($Z<30$), Auger emission is the dominant process. Thus in a XPS spectrum, Auger electron peaks also appear and sometimes overlap with photoelectron peaks. The kinetic energy of Auger electrons is characteristic of the elemental composition and is independent of the excitation energy, while the kinetic energy of the photoelectrons depends on the X-ray energy [15, 16].

3.2 Devices Characterization

In the last two sections we describe the techniques and the instrumentation used for the electrical characterization of the devices we have investigated during this thesis.

3.2.1 PhotoCurrent Spectroscopy (PCS)

Photoconductivity is an optical and electrical phenomenon in which a material becomes more conductive due to the absorption of electro-magnetic radiation such as visible light, ultraviolet light, or gamma radiation. When light is absorbed by the semiconductor, the configuration of electrons and holes changes and the electrical conductivity of the semiconductor rises. Therefore, the mechanism at the basis of photoconduction is the absorption of a photon by an electron. To cause excitation, the light that strikes the semiconductor must have enough energy to induce electrons across the forbidden bandgap or by exciting the impurities within the bandgap. When a bias voltage and a load resistor are used in series with the semiconductor, a voltage drop across the load resistors can be measured as the change in electrical conductivity varies the current flowing through the circuit.
If we consider $J=\sigma E$, where J is the current density, and E the applied field we obtain:

$$J=e(n\mu_n + p\mu_p)E \qquad (3.5)$$

Where n and p are the electron and hole concentration respectively, and μ_n, μ_p their mobilities. When a photon is absorbed, an electron-hole pair is generated, as a result, the elecrical conductivity of the material will increase:

$$\Delta\sigma = e(\Delta n\mu_n + \Delta p\mu_p) \rightarrow J = e(\sigma + \Delta\sigma)E = J_{bulk} + J_{ph} \qquad (3.6)$$

Therefore, it can be possible to detect light absorption by measuring the increse in the sample current [17].

3.2.1.1 Charge carrier generation

When a photon is absorbed by an organic semiconductor it does not directly generate a hole-electron pair, but rather an excited state. The material can immediately emit the absorbed photon, or an exciton can be generated. An exciton is a bound state of an electron and a hole. In inorganic semiconductors, the binding force between the hole-electron pair is very weak (1 meV to 40 meV), therefore the so formed exciton can easily dissociate thus increasing free charge carrier density. In organic semiconductors, the exciton bonding force is generally higher (100meV to 300meV) therefore generating free charge carriers is not as easy. Two different polaronic states on distinct molecules are generally required. Moreover, every charge carrier is available for charge conduction only for a certain time, therefore, the average life time τ should be long enough to allow charge carrier to be collected by the electrodes. Among several factors that can influence τ, the most important one is charge recombination in the material. The presence of recombination sites (as deep levels T_2 located in the middle of the energetic band gap, depicted in Figure 3.10) can dramatically boost this process, decreasing too much charge carrier life time so that no photocurrent signal can be detected. The presence of traps (shallow states in the band gap as T1 in Figure 3.10) can bond charge carrier only for a certain time (which depends on the energy associated to the trap in the band gap) but also in this case the macroscopic effect will be a decrease in the detectable photocurrent due to charge trapping [17].

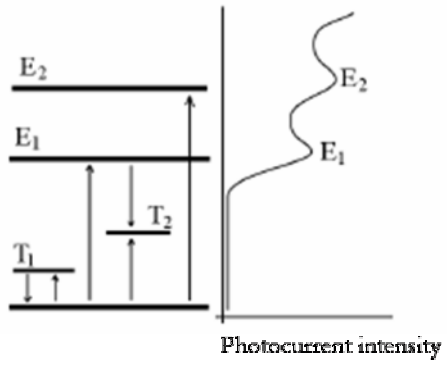

Figure 3.10: Sketch of an energetic diagram and its relative photocurrent spectrum.

As previously reported, in order to promote an electron from HOMO to LUMO, the system should acquire energy equal to the difference between the two levels, namely the energy gap E_G. Therefore, when the energy of the incident radiation is comparable to E_G the absorption signal as a function of the wavelength will rapidly increase (see peak E_1 in Figure 3.10). The other peaks detectable in the spectra can be due to the presence of deep or shallow traps, when the energy of the incident radiation is lower than E_G, or to transition between higher energy levels when it is higher than E_G. In fact, in an organic molecule several anti-bonding orbitals are present (LUMO representing the lowest one) and the higher energetic peaks can be explained with higher energetic transitions.

3.2.1.2 Measurement set up

The basic component of the measurement system employed by us is a Stanford Research 530 lock-in amplifier. It basically makes the sampling of an alternate signal which has a known frequency, in order to separate the signal from the noise generated by the measuring system. The reference frequency is set by the user in the TTL wave forms generator which controls the step motor of the chopper (basically a disk with periodic holes in order to chop the incident light beam), and gives the reference signal to the lock-in.

The light is produced by a halogenous lamp QTH (24V, 150W), and after passing through the chopper it is collected in the monochromator allowing to select the output wavelength which will irradiate the sample.

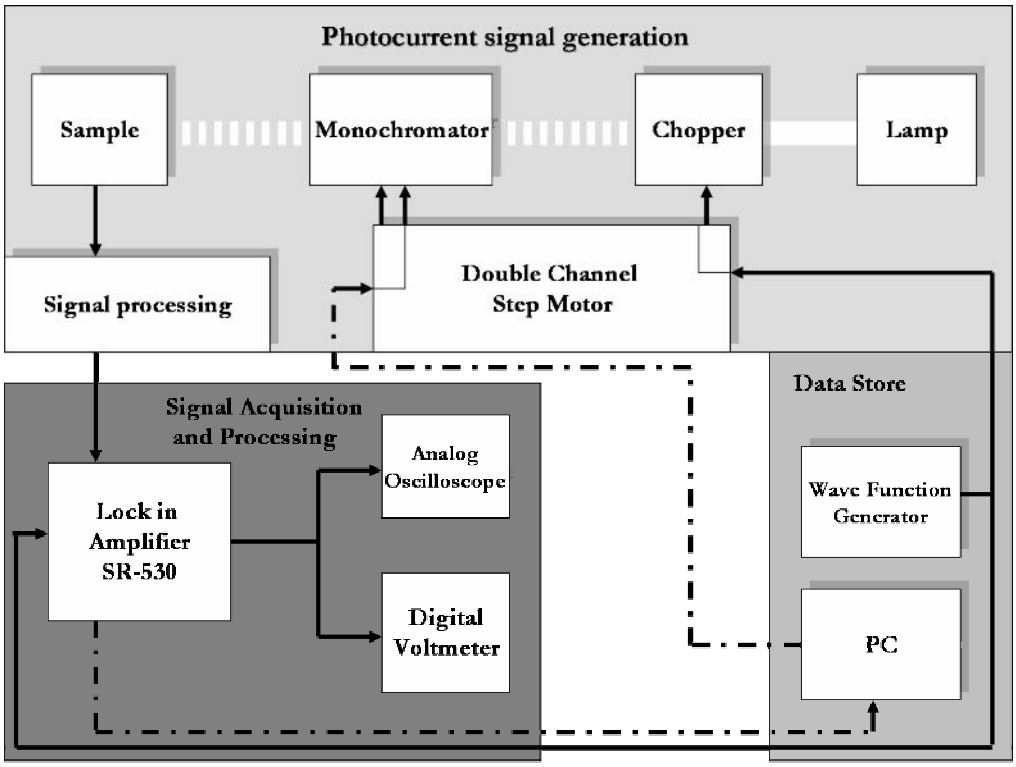

Figure 3.11: Block diagram of the measurement system.

In order to detect the current variation induced by the incident monochromatic beam striking the sample, it is necessary to manipulate the signal coming out from the sample and adapt it to the lock-in amplifier. In Figure 3.12 the circuital scheme employed for this issue is reported. The circuit is biased by a chemical battery (9V) and a resistance is put in series with the sample.

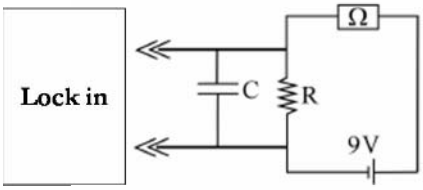

Figure 3.12: Circuital scheme employed to manipulate the signal entering the lock-in amplifier.

The detected signal is the voltage drop in the load resistance at the entrance of the lock-in amplifier. As can be seen from Figure 3.12, a capacitance is put is parallel with the load resistance. This was made to realize a low pass filter in order to cut the high frequencies and do not let them enter the lock n amplifier.

3.2.2 Electrical characterization

The electrical characteristics of the assembled OFETs were measured by employing a semiconductor parameter analyzer HP4155 provided by Hewlett Packard. HP4155 is an electronic instrument for measuring and analyzing the characteristics of semiconductor devices. This one instrument allows you to perform both measurement and data analysis. In the following its main features are summarised:

- *Measurement Capabilities*

  The 4155 has four highly accurate source/monitor units (SMUs), two voltage source units (VSUs), and two voltage measurement units (VMUs). It can perform three types of measurements, sweep measurement, sampling measurement, and quasi-static C-V measurement, and also provides knob sweep measurement function for quick sweep measurements executed by rotating the rotary knob on the front panel. Moreover, it is provided with a pulse generator unit (PGU), which is installed in Agilent 41501A/B SMU/Pulse Generator Expander.

- *Analysis Function*

  The 4155 provides a marker and two lines for analyzing the measurement results. The 4155 also provides the automatic analysis function which moves marker and lines at desired location and displays desired calculation results automatically after measurement is completed.
- *Data storing*

  The 4155 allows to store measurement setup information, measurement data, and instrument setting information on a 3.5-inch diskette using the built-in flexible disk drive.

The instrument is generally provided with:

- *Keyboard*

  It is possible to connect the keyboard directly to the 4155 in order to use the instrument by using a keyboard or the front-panel keys.
- *Agilent 41501A/B SMU/Pulse Generator Expander*

  The 41501A/B SMU and Pulse Generator Expander contains pulse generator units (PGUs) and additional SMUs. The 41501A/B is attached to and controlled by the 4155C.
- *Test Fixture*

  Agilent 16442A is the test fixture for the 4155. You can mount your device under test (DUT) on the 16442A, and measure the device characteristics.
- *SMU/PGU Selector*

  Agilent 16440A SMU/Pulse Generator Selector contains two switching circuits to connect the DUT to either an SMU or PGU. You can attach another 16440A to add two more switching circuits [18].

Figure 3.13: HP4155.

The access to the device electrodes is given by a microprobe station provided with sharp gold tips.

References

[1] Binnig, G.; Rohrer, H.; Gerber, Ch.; Weibel, E. Phys. Rev. Lett., 49, 57 (1982).

[2] Binnig, G.; Quate, C. F.; Gerber, Ch. Phys. Rev. Lett., 56, 930 (1986).

[3] Y. Martin, C. C. Williams, and H. K. Wickramasinghe, J. Appl. Phys. 61, 4723 (1987).

[4] G. Meyer and N. M. Amer, Appl. Phys. Lett. 53, 2400 (1988).

[5] C. R. Blanchard, The Chemical Ed., (1 9 9 6 SPRI NGER- VERLAG NEW YORK, I NC.), Vol. 1.

[6] http://www.ntmdt.ru.

[7] M. Birkholz, Thin Film Analysis by X-Ray Scattering. Copyright © 2006 WILEY-VCH Verlag GmbH & Co. KGaA, Weinheim.

[8] http://www.physics.pdx.edu.

[9] http://www.physics.upenn.edu.

[10] epswww.unm.edu/xrd/xrdbasics.pdf.

[11] www.wiley-vch.de/templates/pdf/3527310525_c01.pdf.

[12] B. E. Warren, X-Ray Diffraction, Addison-Wesley, Reading, MA, 1969.

[13] B. D. Cullity, Elements of X-Ray Diffraction, Addison-Wesley, Reading, MA, 1967.

[14] E. N. Maslen, A. G. Fox, M. A. O'Keefe, X-ray Scattering, in: E. Prince (Ed), International Tables for Crystallography, Vol. C (Kluwer Academic, Dordrecht, 2004), p. 554.

[15] C.-M. Chan, Polymer Surface Modification and Characterization, Hanser Publishers, New York, 1994, Chapter 3.

[16] http://en.wikipedia.org.

[17] R. H. Bube, Photoconductivity of Solids. John Wiley & Sons, New York (1960).

[18] http://www.agilent.com.

Chapter 4

Soft Lithography Fabrication of All Organic Field Effect

Organic materials, based on conjugated organic small molecules and polymers, offer the opportunity to produce devices on large-area low-cost plastic substrates [1]. A fundamental issue in device fabrication concerns the availability of suitable materials not only for the active semiconductor layer but also for contacts that so far, have been mainly fabricated with metals. Metals show several problems: first, though deposited in very thin layers, they are not mechanically flexible, and this could compromise the overall robustness of devices; secondly, organic semiconductors offer the possibility of employing very simple and low cost techniques [2] for device assembly, as printing, spin coating, etc., that cannot be applied to metals. Therefore, in an industrial perspective, it would be desirable to employ a unique, easy technique to obtain each layer of the device. Printing contacts with conductive polymers [3, 4] is one possibility, but it has several limits, as the spatial resolution of the printed pattern, and the compatibility between the employed “ink” and the printing hardware [5]. Furthermore, the realization of top-contact devices is very critical, as the solvents employed for contact printing may affect the underlying semiconductor.

Soft lithography [6] represents a step forward to obtain low dimension structures through a reliable, low cost, easy, and reproducible method. It has been successfully applied to organic materials and devices, with very interesting results concerning the lamination of metal contacts [7] or the transfer of metal contacts mediated by surface chemistry treatments [8]. In this chapter, we introduce Soft Lithography (μCP) as a valuable technique for patterning all organic FETs. For this purpose, we employed PEDOT:PSS as conductive polymer.

The first part of the chapter is dedicated to investigate the morphological and structural properties of PEDOT:PSS thin films deposited by spin coating and to study the interface between PEDOT:PSS/pentacene thin films deposited by thermal evaporation. The second part is fully dedicated to the characterization of all organic FETs fabricated by means of μCP and to investigate the dependence of the electrical performances of such devices from their structural and morphological properties.

4.1 A high-resolution NEXAFS investigation of the molecular orientation in the pentacene/PEDOT:PSS system

In the following sections we present an x-ray photoemission spectroscopy (XPS) and highly-resolved near-edge x-ray absorption fine structure (NEXAFS) spectroscopy measurements taken on pentacene thin films of different thickness deposited on a spin coated PEDOT:PSS substrate. Our investigation is focused on the determination of the pentacene molecular orientation, from which we can draw several conclusions about the structural order of the investigated films. In addition, by using the XPS results, we also gain relevant information about the interface PEDOT:PSS/pentacene in terms of film growth and

morphology. Poly(3,4-ethylenedioxythiophene):poly(styrenesulfonate) (PEDOT:PSS) is commonly used as electrode in various organic devices [9, 10]. Its electronic structure, morphology and structural properties have been extensively investigated by using a wide range of experimental techniques like cyclic voltammetry [11], ultraviolet photoelectron spectroscopy (UPS) [12], x-ray photoemission (XPS) [13], optical spectroscopy [14], atomic force microscopy (AFM) [15]. It has excellent conducting and electro-optical properties, very high conductivity, very good stability, and good film-forming properties. Moreover, it has the great advantage of being soluble. This is very important from a technological point of view, since it allows to employ such conducting polymer for the patterning of the electrodes in the realization of all organic electronic devices by employing very easy and low cost techniques, as thermal imaging, inkjet printing or soft lithography [16-18]. On the other hand, Pentacene ($C_{22}H_{14}$) is one of the most widely used organic active media due to its physical, chemical and morphological properties. In particular its high mobility and the possibility to grow highly oriented thin films lead to a strong improvement of the device performances [19]. It is easily understandable that the coupling of two such materials, with excellent properties, especially toward the realisation of “all plastic” electronics, can be considered an important step in device engineering. Therefore, an accurate analysis not only of the single materials structure but also of their interface is very important.

4.1.1 Experimental set up

The measurements were performed at the beamline UE52-PGM at BESSY. This beamline is characterized by a plane grating monochromator. The photon energy ranges from 100 to 1500 eV, with an energy resolving power of $E/\Delta E$= 10500 at 401 eV (c_{ff}=10, 10 μm exit slit). The main chamber (base pressure $2x10^{-10}$ mbar) is equipped with a

standard twin anode x-ray source, a SCIENTA SES200 electron energy analyser, and a home-made partial electron yield detector. PEDOT:PSS thin films (~ 50-100 nm) were spin-coated on Si wafers from a commercial available aqueous solution (Baytron P, 1:20). Thin films of pentacene were prepared by organic molecular beam deposition (OMBD) in-situ using strictly controlled evaporation conditions. The deposition (deposition rate: ~3 Å/min) was monitored with a quadrupole mass spectrometer. The nominal thickness was determined having previously calibrated the evaporator by using the attenuation of the x-ray photoemission spectroscopy (XPS) substrate signal, after pentacene deposition, measured on a Ag(111) single crystal. We carried out NEXAFS measurements in the total electron yield (TEY) mode in grazing incidence (60°). In order to investigate the molecular orientation in the films we took advantage of the dependence of the NEXAFS spectra on the polarisation of the incident radiation [20]. Hence, we measured the spectra by using both in plane (s-pol) and out of plane (p-pol) polarised synchrotron radiation, tuning the polarisation by means of the undulator. Finally, the spectra were normalised using the I_0 current and the substrate signal [21]. The energies have been carefully calibrated according to reference 21. All organic thin films were carefully checked for radiation damage during beam exposure.

4.1.2 XPS and NEXAFS on PEDOT:PSS

In Figure 4.1 we show the S 2p and O 1s XPS edges obtained form the PEDOT:PSS substrate. The pictures reported on the left part were taken by investigating the sample using synchrotron radiation, whereas on the right side were taken using a MgKα excitation. This is particularly interesting because it allows to compare the spectra due to emitted photoelectron with different inelastic free path. In particular, in the first case the experiment is more surface sensitive than in the latter. As can be clearly noticed, the S 2p edge is characterised by two main

features (upper panels), the first, occurring at lower binding energy (A), at around 163 eV, is weak if compared to the feature at higher binding energy (B), around 168 eV. As also reported in previous works in literature, these peaks are attributed transitions from sulphur atoms located in PEDOT and PSS molecules [12]. It is worth to note that the relative intensities are in good agreement with the nominal ratio of the two blended materials. Moreover if we compare the two spectra taken by using different radiation sources, it can be noticed a clear difference in the intensity of the features, in particular concerning the intensity of peak A at lower binding energy due to the sulphur atoms located in the PEDOT. When probing the surface, peak A intensity is higher than when probing the bulk, A' peak intensity, giving the clear indication of a higher concentration of PEDOT in the surface than in the bulk. This results are in good agreement with the ones reported in refs [12, 13], meaning the even employing this deposition procedure we can obtain the same typical texture of PEDOT:PSS with PEDOT at the surface and PSS in the bulk. In the lower part of Figure 4.1 the O 1s spectra are shown. The spectra are characterised by a large feature, in which several contributions can be individuated by fitting the experimental curve. In particular, in Figure 4.1(c)) the spectrum for the incident photon energy of 700 eV is shown together with its fit. The fit analysis results in the presence of four contributions. Accordingly to previous work [12] they are attributed to PSS^{-}-Na^{+}, PSSH, and PSS^{-}, in the lower binding energy range, while the contribution at 533.6 eV is due to PEDOT. Note that the ratio of the relative intensities for the PEDOT and PSS contributions is 1:19, in good agreement with the nominal concentration of the two blends in the solution, further supporting the fit results.

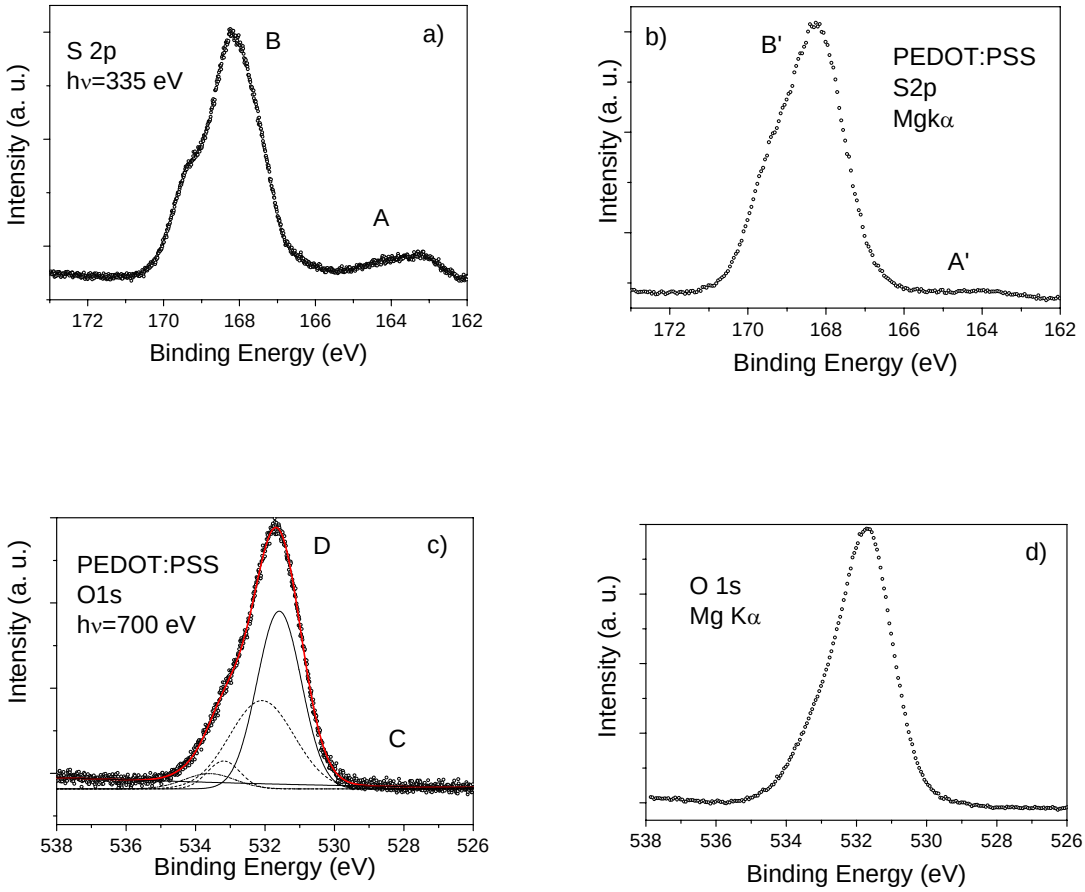

Figure 4.1: XPS spectra of PEDOT:PSS: S 2p, (a) and (b), and O 1s edges, (c) and (d), for two different incident photon energies, as indicated. The fit analysis (black bold curve), including the four obtained fit contributions (straight and dot curves), is also shown in (c) together with the experimental data (open circles).

In order to investigate the molecular order of the PEDOT:PSS deposited film, we analyse the sample by using NEXAFS. With this technique it is possible to irradiate the sample by using two different polarizations. As can be clearly seen in Figure 4.2(a), where the C 1s edge is shown, there is no significant difference in the spectra taken in s-pol and p-pol, meaning that the film is amorphous. Both spectra are characterised by a single very sharp (0.65 eV full width at half maximum) and pronounced resonance around 250 eV. This resonance

is due to transitions from C 1s to π* states. This spectrum presents strong similarities with the NEXAFS C 1s edge spectrum of EDOT [22, 23], a well-defined trimer, recently studied as model system for PEDOT, that forms the basis for the PEDOT:PSS used in the presently investigated blend. In PEDOT:PSS the π *-resonances are much more intense (with respect the σ*-region) indicating a strong influence of the dopant PSS in the electronic structure of PEDOT:PSS.

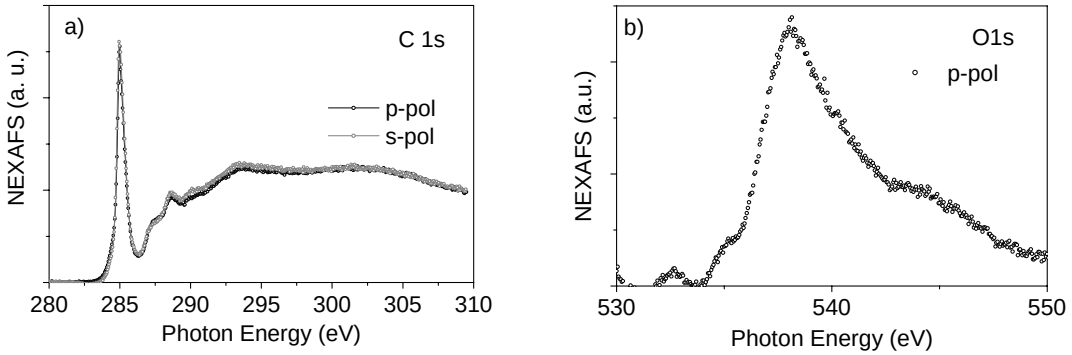

Figure 4.2: a) C 1s NEXAFS spectra of PEDOT:PSS. The spectra were taken in grazing incidence for p- (black curve) and s- (grey curve) polarisation; b) O 1s NEXAFS spectrum of PEDOT:PSS. The spectrum was taken in grazing incidence for p-polarisation.

Also the PEDOT:PSS NEXAFS O 1s edge (Fig. 4.2(b), p-pol) is very similar to the relative edge in EDOT. However, also in this case the details are different. The π* feature at around 532 eV it is not a simple shoulder, but it has a higher relative intensity with respect to the σ* feature at 538 eV, due to a larger overlap of the lowest unoccupied π* states with the O atoms in the blend and indicating again an active influence of the PSS presence in the spectra.

4.1.3 XPS and NEXAFS on Pentacene/PEDOT:PSS

On the characterised PEDOT:PSS substrates, we deposited several pentacene films by using OMBD with a constant evaporation range of ~3 Å/min. It is worth to underline that the XPS C 1s edge data cannot be used for a qualitative or for a quantitative discussion, since this XPS edge, already very broad in PEDOT:PSS, does not differ in a sensible way upon pentacene deposition, with the exception of the increase of the intensity signal due to the increase of the carbon amount. On the contrary, the investigation of the PEDOT:PSS XPS signal attenuation at the S 2p and O 1s edges gives a wealth of information about the film growth and morphology.

A point that is still not completely clear regards the possibility that, due to the high PEDOT:PSS roughness, pentacene islands could grow embedded in the matrix formed by PEDOT:PSS at least up to a certain nominal thickness, or form a mixed region, characterised by interaction and charge transfer with PEDOT:PSS like in case of phthalocyanine [24].

This aspect is important not only for the obvious importance of a basic characterisation of this system, but also because of its technological relevance. As a matter of fact, the device characteristics depend also on the respective charge injection barriers at the interfaces. This can be influenced by the interface morphology in terms of intermixing of the two organic materials.

In Figure 4.3 we report the XPS attenuation signal for S 2p and O 1s edges measured for different incident radiations. Therefore, the collected photoelectrons are characterized by a different inelastic mean path for different incident photon energies, i.e., different kinetic energies. If we analyse the S 2p and C 1s signals, we can clearly notice that while the first one is decreasing in intensity the latter is increasing; it is possible therefore to estimate that the PEDOT:PSS photoelectrons travel through pentacene with a kinetic energy of 167 eV and they have

λ=-6Å. The attenuation curve seems to follow a Frank-van der Merwe behaviour, which predicts a layer by layer growth of the organic material. This is clearly indicated by the fact that the S 2p attenuation signal is decreasing almost linearly as function of the film thickness. In contrast to this, the analysis of the O 1s signal for 700 eV (λ = ~ 24), and for Mg Kα (λ = ~ 11 Å) shows a rapid attenuation in both cases and is most indicating a Stranski-Krastanov behaviour, characterized by a layer plus island growth, which predicts a quick wetting of the substrate, resulting in the rapid formation of an almost complete first monolayer that should therefore lead to a significant attenuation of the signal also for very thin deposited films.

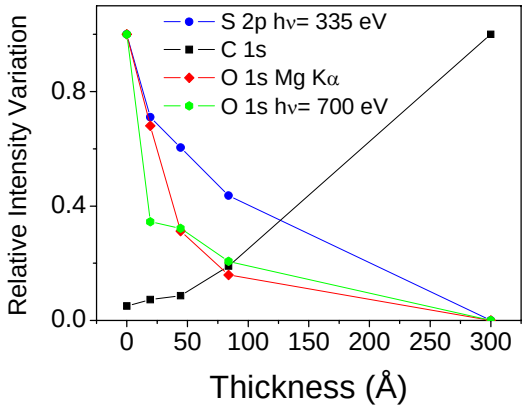

Figure 4.3: O 1s and S 2p XPS signal attenuations and C 1s XPS signal variation as a function of the film thickness. The O 1s signal attenuations is shown for two different incident photon energies, as indicated. Solid lines are intended as a guide to the eyes.

As a consequence, we can deduce that pentacene molecules start growing on the PEDOT:PSS surface forming a layered structure. After, island nucleation occurs thus leading to a complete attenuation of the substrate signal for higher nominal thicknesses, up to 300Å. Moreover, we can indirectly gain some information concerning the PEDOT:PSS/pentacene interface by analysing the attenuation of the O 1s signal. It seems that such interface does not present a large intermixing area. If it was the case, the attenuation of the substrate

signal would strongly slowed down, leading to obtain an evident signal reduction only at very high thicknesses, higher than the one reported in Figure 4.3 where a drop of the O 1s signal below 40% already occurs at 20Å.

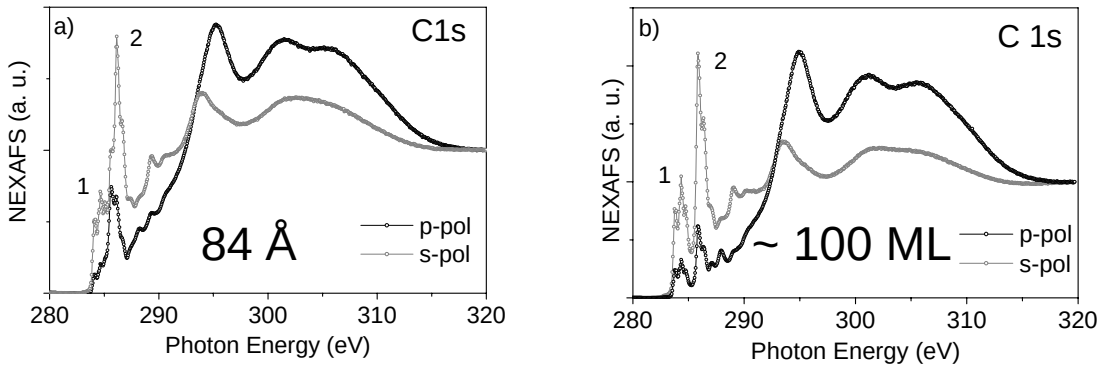

Figure 4.4: C 1s NEXAFS spectra obtained from a 84 Å film (a) and ~100 ML (b) of pentacene on PEDOT:PSS. The spectra were taken in grazing incidence for p- (black curves) and s- grey curves) polarisation. The numbers, 1 and 2, assign the main features as discussed in the text.

Further information concerning the molecular orientation of pentacene upon deposition onto the PEDOT:PSS surface can be gained by the analysis of the NEXAFS spectra taken in grazing incident for p- and s-polarization. The data are reported in Figure 4.4 where the evolution of the C 1s edge obtained from 84Å and 100 ML is shown. Two main groups of π^*-resonances, 1 and 2, dominate the 282-288 eV photon energy range. These features are due to transitions from C 1s levels of non-equivalent carbon atoms into the lowest unoccupied molecular orbital (LUMO) and LUMO+1 [25]. It is worth to mention that the energy resolving power of the UE52 beamline gives the opportunity to perform highly resolved measurements. Thus the spectra exhibit the presence of features that were not resolved in previous works. Figure 4.5 shows the high-resolved π^*-region of the C 1s NEXAFS spectra

taken for the 100 ML film. It is possible to observe the clear presence of two components in feature A (Figure 4.5), due to contributions from two different carbon sites in the pentacene molecule [25]. This spectrum shows strong similarities, with that from the gas phase in ref. 25, suggesting a van der Waals character of the molecule-molecule interaction in these films.

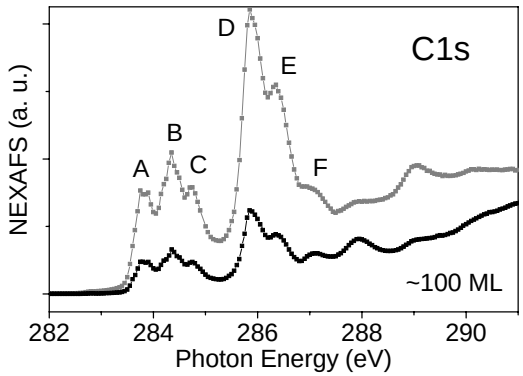

Figure 4.5: High-resolved π*-region of the C 1s NEXAFS spectra taken for the 100 ML film, for p- (black curves) and s- grey curves) polarisation. The capital letters assign the main features as discussed in the text.

The spectral features exhibit strong polarisation dependence, indicating a high degree of orientation order in the films, and allowing us to determine the molecular orientation from the observed dichroic behaviour [20]. In both cases the molecules adopt an upright standing position of their axis with respect to the substrate. This can be clearly seen since the π*-resonances show their strongest intensities for the spectra taken for s-polarisation of the incident radiation (i.e. *E* vector parallel to surface). The π*- or the σ*-resonances are largest when the electric field vector of the incident radiation is along the π* or the σ* orbitals, respectively. It can be shown directly from the dipole selection rules that for a plane-type orbital, i.e. an orbital that points in a specific direction like the π* orbital in an aromatic ring, the resonances intensity is given by:

$$I \propto \left(\cos^2\theta \sin^2\alpha + 2\sin^2\theta \cos^2\alpha\right) \qquad (4.1)$$

where we assume perfect polarisation, (this condition was satisfied during our measurements at the UE52-PGM beamline) being α the angle between the normal to the surface and the orbital and θ the angle between the incident radiation and the normal to the surface. Measuring the intensity for two different polarization directions with respect to the surface, s-pol and p-pol, it is possible to determine the angle α from the following equation:

$$\frac{1}{\tan^2\alpha} = \frac{1}{2}\left(1 - \frac{1-q}{\sin^2\theta_{\text{p-pol}} - q\sin^2\theta_{\text{s-pol}}}\right) \qquad (4.2)$$

where q is the ratio between the intensities of the chosen resonances for the two different polarisations:

$$q = \frac{I(\theta_{\text{s-pol}})}{I(\theta_{\text{p-pol}})} \qquad (4.3)$$

In this work, $\theta_{\text{s-pol}}=0°$ and $\theta_{\text{p-pol}}=60°$. Eq. 4.2 can be rewritten as:

$$\frac{1}{\tan^2\alpha} = \frac{1}{2}\left(1 - \frac{1-q}{\sin^2 60^\circ}\right) \qquad (4.4)$$

We performed molecular orientation calculations by using only the π*-resonances intensities because of the fact that in our spectra they are very sharp. In particular, the values given in this work are calculated on the resonance 2 and cross checked on the others. The calculated molecular orientation is 80° for the 84 Å film, while it is very

close to a perfect upright position for the thicker film. However, from the morphological point of view the two situations are different. Taking the calculated molecular orientation into account, and assuming that the molecules are standing with their long axis perpendicular to the substrate (a pentacene molecule is 16.577 Å long [26]), 84 Å are equivalent to nominal ~ 5 ML. For this film thickness, the XPS substrate signal should be completely attenuated by the pentacene deposition, but, as already discussed, the substrate signal is still clearly visible, while for the 100 ML film the XPS signal from the substrate is not visible (see Figure 4.3). This is not the only difference with thickness; comparing the spectra obtained from the two films, we can observe a change of the spectral shape and of the ratio of the relative intensities when looking at the two main groups of π*-resonances, 1 and 2. First, this clearly indicates that pentacene molecules interact with PEDOT:PSS. Second, this interaction with the substrate seems to induce different short range order in the film and to influence the mutual molecular interaction. In addition, the mutual molecular interaction obviously changes in the two cases due to the different film morphology and to the environment seen from the molecules. However, the interpretation of these effects cannot be deduced without a detailed comparison with appropriate calculations, in order to link every single spectral feature with a specific transition and to understand how these transitions vary with thickness and therefore with the environmental influence (i.e. substrate-molecules versus molecules-molecules interaction, distortion of the molecular skeleton, etc). This aspect will be addressed in detail in our future work.

A consequent crucial point is: do the molecules also stand upright in the first layer? To give an answer to this question we have performed NEXAFS measurements on a pentacene monolayer in order to investigate the molecular orientation of the first pentacene layer when deposited on PEDOT:PSS. The spectra are shown in Fig 4.6. According

to the previous discussion, it is immediately clear that the molecules, also in this case, take a position such that their axis is perpendicular to the substrate. The dichroism is very pronounced indicating once more a high order in the molecular orientation already at the monolayer level. The calculated molecular orientation is 77°.

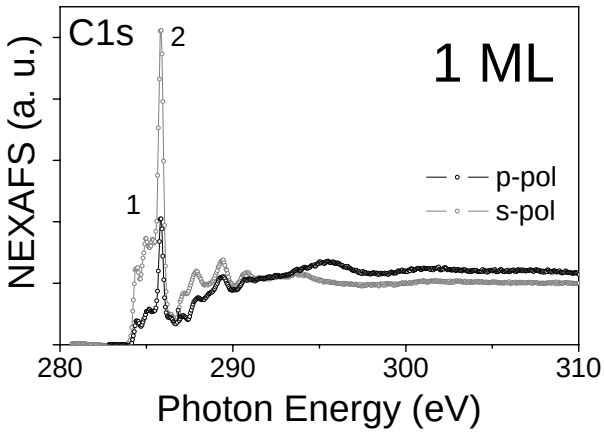

Figure 4.6: C 1s NEXAFS spectra obtained from a monolayer of pentacene on PEDOT:PSS.

Thus also a monolayer of pentacene deposited on PEDOT:PSS is characterised by molecules with a molecular orientation toward the upright standing position. Similarly to the thicker films, the monolayer spectra are characterised by the two main groups of π*-resonances in the 282 -288 eV photon energy range (1 and 2 in Figure 4.6), but their relative intensities and shapes are dramatically changed in comparison. This undoubtedly proves the occurrence of a charge transfer at the interface PEDOT:PSS/pentacene. As a matter of fact, this drastic intensity decrease of the π*-resonances is not observed for pure van der Waals bonding between substrate and adsorbate layer, because this bond does not involve π* orbitals like, for example, the LUMO or the LUMO+1, thus there is no any effect on the transitions from C 1s levels to those same orbitals [27].

4.1.4 Thermal stability of Pentacene on PEDOT:PSS

With the purpose of testing the thermal stability of the pentacene films deposited on PEDOT:PSS, we annealed the thicker samples up to 365 K and we checked them after annealing by using XPS and NEXAFS. Each annealing was 30 minutes long. We show here the results for a ~100 ML film. It has been sequentially annealed at 330 and 365 K. Figure 4.7 shows the C1s NEXAFS s-pol spectrum, focused on the π*-region, after the last annealing cycle, in comparison with the as prepared spectrum. The molecular orientation basically remains unchanged, not affected by the annealing. But the electronic structure is dramatically influenced.

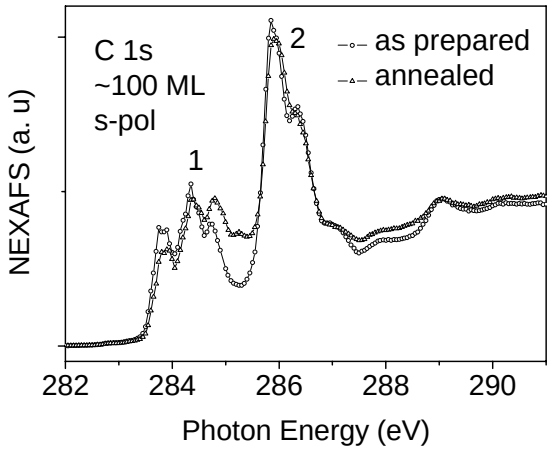

Figure 4.7: C 1s NEXAFS spectra (s-pol) for a 100 ML film before and after annealing up to 365 K.

The intensity ratio of the main group of π*-resonances, 1 in the figure, are changed indicating a strong influence of the annealing treatment mainly on the contributions due to transitions from C 1s levels to the LUMO or the LUMO+1. We can deduce from this observation that a different intermolecular interaction characterises the annealed films in comparison with the as prepared ones. Also in this

case, a detailed comparison with appropriate calculations will help to understand how these transitions vary depending on the annealing.

4.2 All Organic FETs on Mylar®: assembling procedures

Assembling all organic FETs on Mylar® requires a very careful processing. The first step is the assembling of the Mylar foil; in order to realize a flat surface it is glued onto a circular frame, as depicted in Figure 4.8.

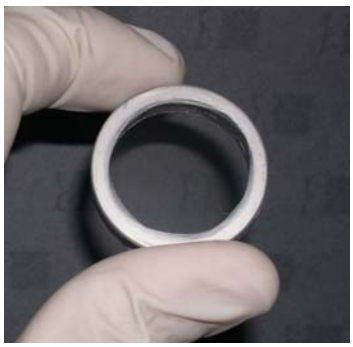

Figure 4.8: A Mylar® foil glued onto a circular frame.

After that, prior organic semiconductor deposition and electrodes patterning, Mylar® surface is carefully cleaned with ethanol, isopropanol, washed with deionised water, and dried in nitrogen flux. Once the substrate is cleaned, we can start with the printing process, the step by step procedure is shown in Figure 4.10. The PDMS stamp, which reproduces the Source and Drain pattern, is put in the spin coater sample holder with the relieves exposed upwards and covered with few drops of PEDOT:PSS. After a resting time of 5 minutes before spin coating, in order to help solvent evaporation and to increase the adhesion between PEDOT:PSS and PDMS surface, the sample is spun for 1 minute at 1000 Root per Minute (RPM), this spinning rate resulted to be optimal for obtaining homogeneous PEDOT:PSS films with a nominal thickness around 100nm. After the stamp preparation, contacts are transferred onto the substrate by realizing a conformal

contact between stamp and substrate, without any external pressure, for about 5 min. Then, the stamp can be carefully removed resulting in a transfer of contacts with a pretty high yield (90%). The final result is a completely flexible and transparent structure as can be clearly noticed from Figure 4.9, where the features of the printed electrodes and the final assembled structure are shown.

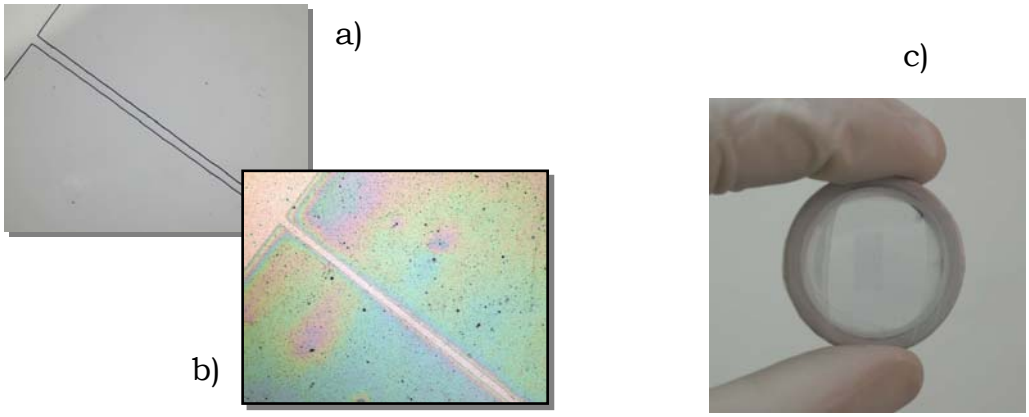

Figure 4.9: pictures showing the features of the PDMS stamp (a) compared to the printed electrodes ones (b), and the structure of the final assembled device (c). As can be seen, the final structure is almost transparent.

As Mylar® does not tolerate thermal treatment over 40 °C, no annealing step was performed on the PEDT/PSS thin film after deposition, a step generally made to increase PEDT to PSS ratio. Indeed, a pre-deposition annealing was realized at 120 °C, producing an increase of PEDT/PSS conductivity by a factor of 2 with respect to untreated PEDT/PSS films. Electrodes with W= 5 mm and L=75μm (where W and L are the channel width and length respectively) were used. It is worth to note that electrode dimensions can be easily lowered due to the high resolution of the PDMS, which is able to reproduce features in the order of 100nm. The only limit for this purpose concerns the realization of a high-resolution master used for the stamp

fabrication. The realization of master for soft lithography with less than 1 µm. feature sizes is very common.

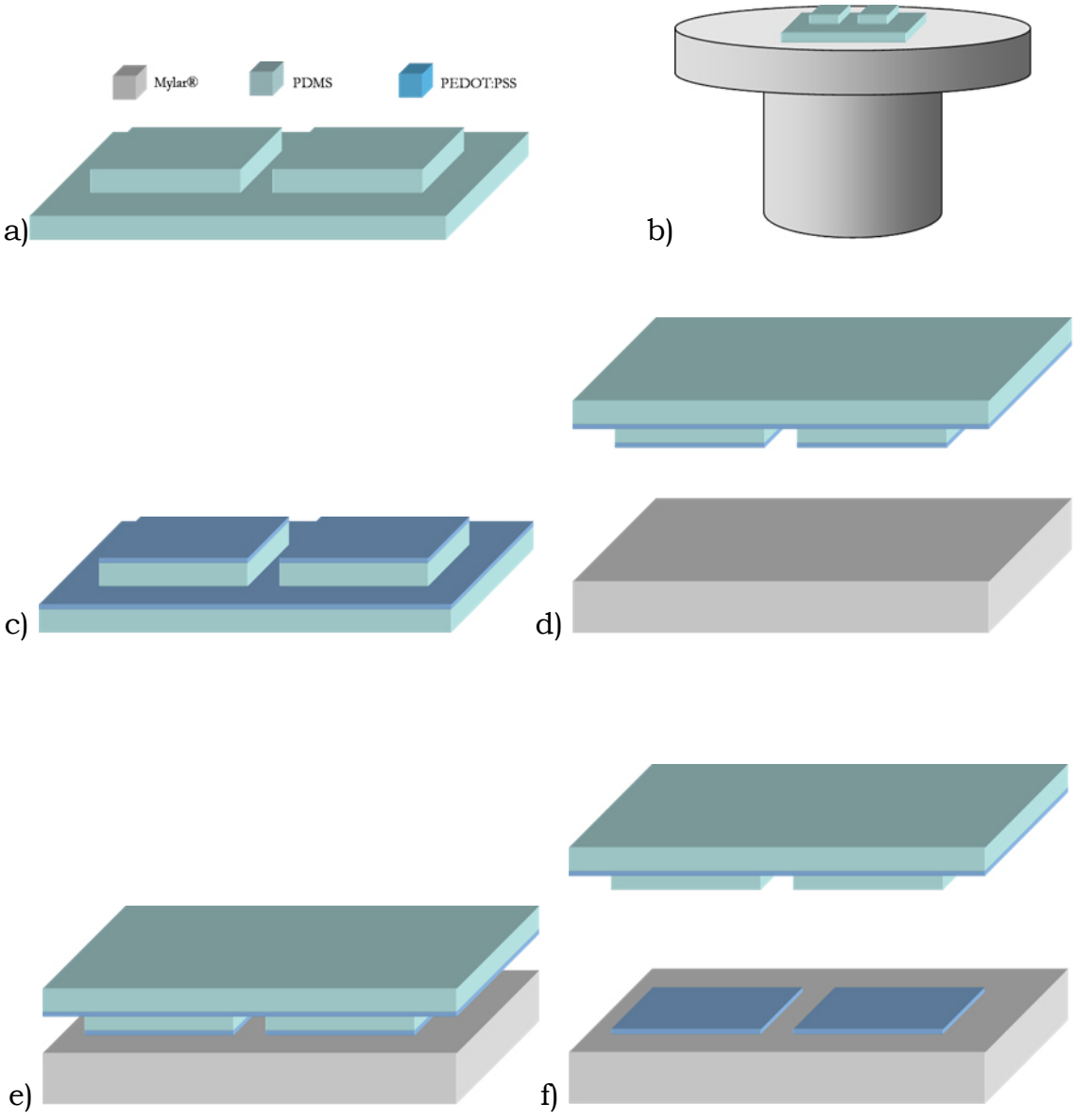

Figure 4.10: Schematic representation of the steps required for patterning the electrodes by means of µCP.

The last two steps concerns the deposition of the gate electrodes, which was realized by spin coating a thin PEDOT:PSS film

on the opposite side of the Mylar® foil, and the deposition of the organic semiconductor layer. In this section we will discuss about All Organic FETs realized with pentacene (Sigma Aldrich, 98%) as organic active layer. In this case, pentacene was used as received and deposited by thermal evaporation at a nominal deposition rate around 0.5-1Å/s for a thickness of 50nm. This rate resulted to be optimal for obtaining homogeneous and continuous pentacene films on Mylar®. During deposition, the pentacene layer was patterned by interposing a shadow mask between the crucible and the sample. This was done with the aim of leaving a portion of the electrode area not superposed to the semiconductor, where the probe tips were put during the electrical measurements. In this way, any risk of contact between the tips and the semiconductor is prevented, see Figure 4.11. It is worth to underline that with this technique it is possible to realize both bottom contact and top contact devices just by printing the electrodes before or after the organic semiconductor deposition respectively.

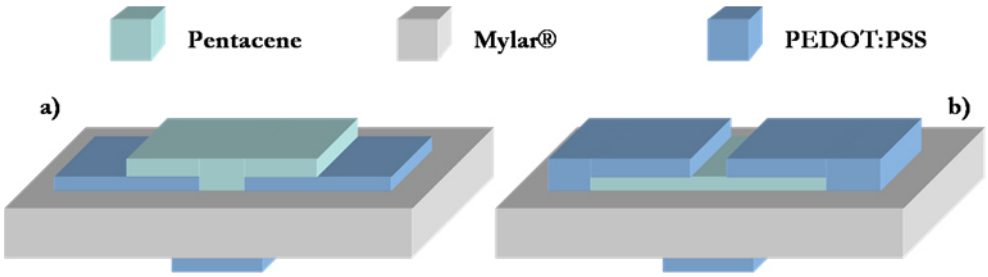

Figure 4.11: Bottom Contact and Top Contact devices structure.

4.3 A comparison between Bottom Contact and Top Contact All Organic FETs

All-organic FETs were realized on a flexible plastic PET foil (Mylar®, DuPont), as described in the previous section, allowing to fabricate in a very easy and efficient way devices in both Bottom Contact and Top Contact configuration. The electrical characterization of the devices was carried out at room temperature in air. All devices

worked as unipolar p-type FETs working in accumulation regime, as can be noticed from Figure 4.12 where the output characteristics of both kind of devices are shown, with mobilities up to 2 x 10^{-1} cm^2/Vs and I_{on}/I_{off} ratio up to 10^5. In order to make a reliable comparison

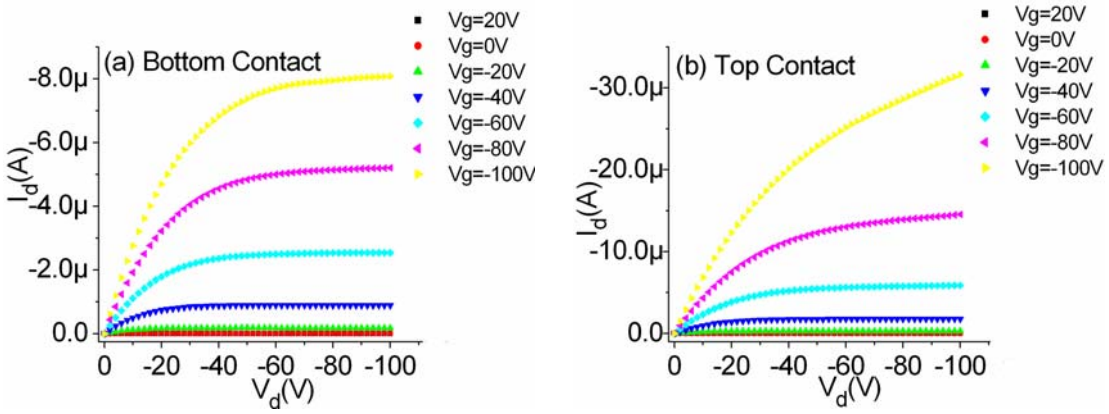

Figure 4.12: Output characteristic of all organic FETs in BC (a) and TC (b) configurations.

between the two different configurations, we fabricate BC and TC devices on the same substrate. The first step, after the cleaning procedure of the Mylar® surface, was the pattering of the source and drain electrodes for the BC device, then the active layer was deposited following the procedure described in the previous section. Finally TC device electrodes were printed beside the BC ones. In this way, the organic semiconductor film was deposited at the same time for both devices allowing to have the same thickness and quality within the channel of each device. From the analysis of the most meaningful parameters some interesting marked differences can be clearly pointed out. First of all, from the analysis of the curves reported in Figure 4.12 it is pretty clear that T-C devices showed the best performances with recorded currents higher by a factor of 4-5 than B-C devices realized on the same semiconductor layer and this trend was reproducible over tens of couple of devices. The shed light into this phenomenon, we took into account the equivalent circuit suggested by Horowitz and previously introduced in chapter 2. In this model a resistance is inserted in series

with the device channel. According to this, both mobility and contact series resistance can be estimated directly from the electrical measurements. This is particularly meaningful in this case since the two structures should have similar channel characteristics (so they should have similar channel mobility values) but they differ for the way in which the contact-semiconductor interface was formed. In fact, for BC devices, pentacene is deposited onto the already patterned PEDOT:PSS contacts, so there is a direct charge carrier injection from the electrodes to the device channel (according to the idea that the channel is a very thin layer formed at the interface between semiconductor and insulator), whereas in TC devices, the current injected from the electrodes must vertically travel through the pentacene layer before reaching the channel, and this should imply that the effective voltage across the channel is lower that the voltage applied between source and drain by a quantity $R_S I_D$, where R_S is the equivalent resistance of the vertical current path in the pentacene layer and I_D is the drain current. In addition, a contribution to R_S may derive from the different interface between contact electrodes and semiconductor, due to the different structure of the devices. So, together, these two phenomena should produce in the electrical measurements the effect of a resistance in series with the device channel.

$$I_D = Z / L \mu C_{ins} (V_G - V_{th})(V_D - R_S I_D) \qquad (4.5)$$

$$R_{total} = R_s + \frac{L}{W \mu C_{ins} \left| (V_G - V_{th}) \right|} \qquad (4.6)$$

where R_s is the Contact Series Resistance, μ is the hole mobility, C_{ins} the capacitance of the insulator, and all the other parameters are given by the conventional notations. As a matter of fact, there is a very meaningful difference in the Rs *vs* V_G curve recorded for both kind of

devices, as can be clearly notice from Figure 4.13, and this trend is reproducible over tens of couple of devices.

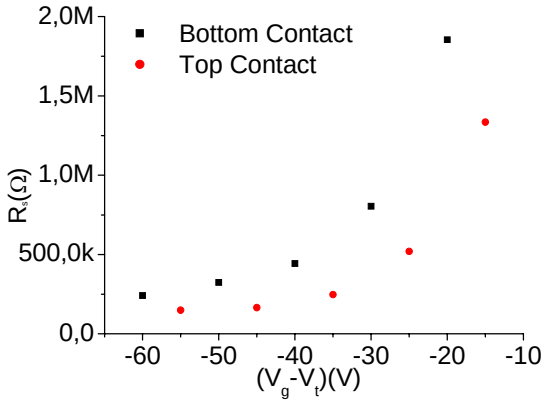

Figure 4.13: Comparison between the Rs vs (V_G-V_T) curves of a TC and a BC device.

On the other hand, also the mobility is different in the two cases; indeed, in all the couple of devices characterised, the recorded mobility is always higher in TC OFETs. According to Horowitz model, it is possible to evaluate the channel mobility subtracting the effect of the contact resistance effects. In principle, mobility values should be equal, since the semiconductor was deposited for both devices at the same time, but as it is reported in table 4.I, there is a significant difference between the two different devices, meaning that a simple model which includes only one parasitic contact series resistance cannot explain all the characteristics recorded from the experiments. In order to shed more light into these phenomena, we investigated, by means of Atomic Force Microscopy (AFM), the morphology of the active layer for both devices, focussing in particular to the interface between electrodes and channel. All images reported in Figure 4.14 are height images and were taken in semi-contact mode.

	V_{th} (V)	μ (cm^2/Vs)	R_s (Ohm) ($V_G - V_T$= -40V)	I_{on}/I_{off}	S (V/dec)	N_{max} ($cm^{-2}eV^{-1}$)
Bottom Contact	-30	4×10^{-2}	$4{,}43 \times 10^5$	10^5	14,5	3×10^{12}
Top Contact	-32	1×10^{-1}	$2{,}47 \times 10^5$	10^5	7,2	$1{,}4 \times 10^{12}$

Table 4.I: Tabulation of threshold voltage (V_{th}), field effect mobility (μ), I_{on}/I_{off} ratio, sub-threshold slope (S), and trap states density (N_{max}) for T-C and B-C devices.

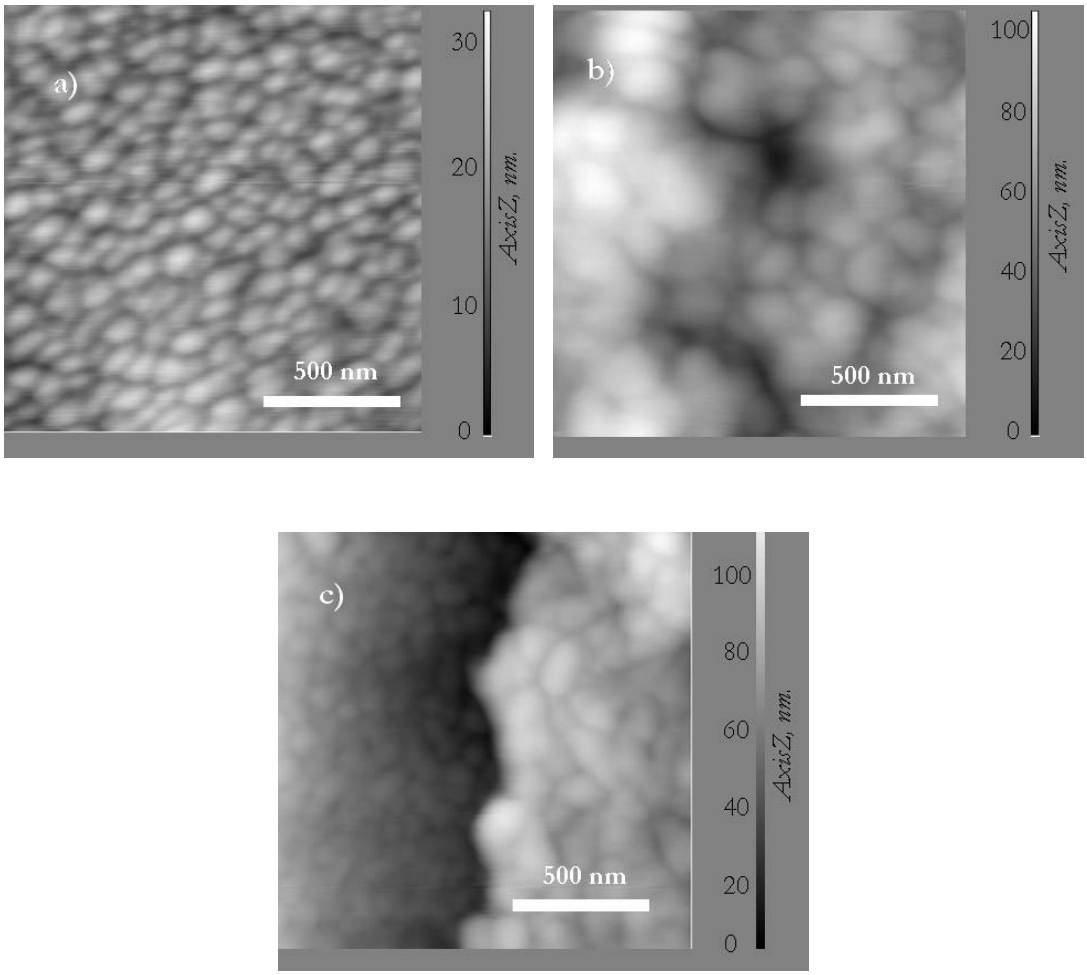

Figure 4.14: AFM images of: pentacene layer in the middle of the channel (a); pentacene layer over a PEDOT:PSS contact (b); and the transiotion area between channel and contact in a BC device (c).

It is worth to underline that in the case of TC devices the organic semiconductor was deposited in advance onto the bare Mylar® substrate, and therefore it must grow almost uniformly everywhere, since the electrodes were printed afterwards. For BC devices the situation is very different. In fact, the organic layer was deposited over the already patterned Mylar® substrate (Source and Drain electrodes were printed prior semiconductor deposition) which could affect the growth mechanism of the organic layer, in particular in the transition area between contacts and channel. As can be seen in Figure 4.14, there is a relevant difference in the pentacene film deposited in different regions of the BC device. It is almost uniform in the middle of the channel, whereas it is very inhomogeneous at the interface between contact and channel. In particular, in this region we can see an abrupt change in the morphology of the active layer passing from the area over the PEDOT:PSS electrode and the area into the channel.

This led to an accumulation of defects in this transition interfacial area thus leading to a dramatic increase in the density of traps that strongly limits charge injection into the channel. This discontinuity obviously does not exist in TC devices where, since the organic semiconductor was deposited prior the electrodes printing, it should be uniform everywhere. The higher density of traps at the interface between electrodes and channel seems therefore to be the main reason for the increase in the contact series resistance and also for the decrease in the channel mobility estimated for BC devices.

4.3.1 Analysis of the hysteresis effects

Another clear difference in the electrical behaviour of BC and TC devices can be pointed out by analysing the transfer characteristics in the saturation region. In this case the electrical measurements were recorded by keeping the V_{DS} constant at -100V in order to be in saturation region, and sweeping the V_{GS} from +100 to -100V and from -

100 to +100V. As can be clearly noticed in Figure 4.15, both devices are affected by hysteresis, but while in the case of TC this behaviour is almost negligible, it is definitely more pronounced for BC once.

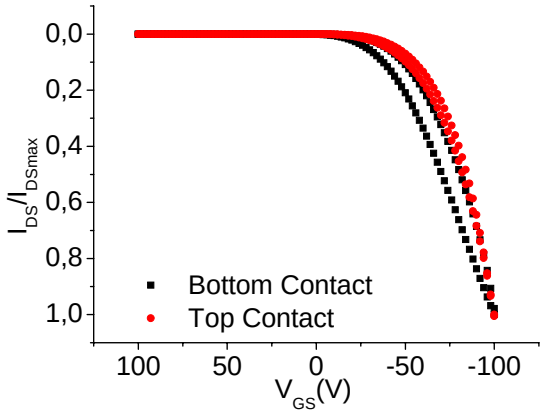

Figure 4.15: Comparison between the normalized transfer characteristics in saturation regime (V_{DS}=-100V) of B-C and T-C devices.

This behaviour is a clear indication that BC devices are affected by higher parasitic capacitance phenomena, most probably correlated to charge trapping within the active layer. In order to shed some light into this issue, we calculated the inverse sub-threshold slope S, for both devices, since it is directly correlated to the number of trap states at the interface between insulator and semiconductor (as we previously reported in section 2.1.2). We herein remind that the inverse sub-threshold slope is given by:

$$S = \left[\frac{d \log(I_d)}{dV_g} \right]^{-1} \quad (4.6)$$

we obtained values around S= 6 V/dec and S= 11 V/dec for T-C and B-C devices respectively. In Figure 4.16 we report an example. Further analysis is possible from the sub-threshold slope calculation. The maximum number of interface traps can be estimated using equation

(4.7), assuming that densities of deep bulk states and interface states are independent of energy:

$$N_{SS}^{\max} = \left[\frac{S \cdot \log(e)}{kT/q} - 1 \right] \frac{C_i}{q} \qquad (4.7)$$

where $N_{SS}^{\max}$ is the maximum number of interface traps states, k is the Boltzmann's constant, T the absolute temperature and q the electronic charge. As reported in Table 4.I, we obtained an average $N_{SS}^{\max}$ = 1.5 x 10^{12} $cm^{-2}eV^{-1}$ and $N_{SS}^{\max}$ = 2.5 x 10^{12} $cm^{-2}eV^{-1}$, for T-C and B-C devices respectively. As a result, depositing the organic semiconductor layer after the patterning of the Source and Drain electrodes leads not only to an increase in the density of defects at the interface between the semiconductor Source and Drain electrodes, but also to an increase in the insulator/semiconductor interface trap states if compared to T-C structures, this higher density of charge traps can be therefore considered the main reason for the increase of the hysteresis effect in the recorded electrical characteristics.

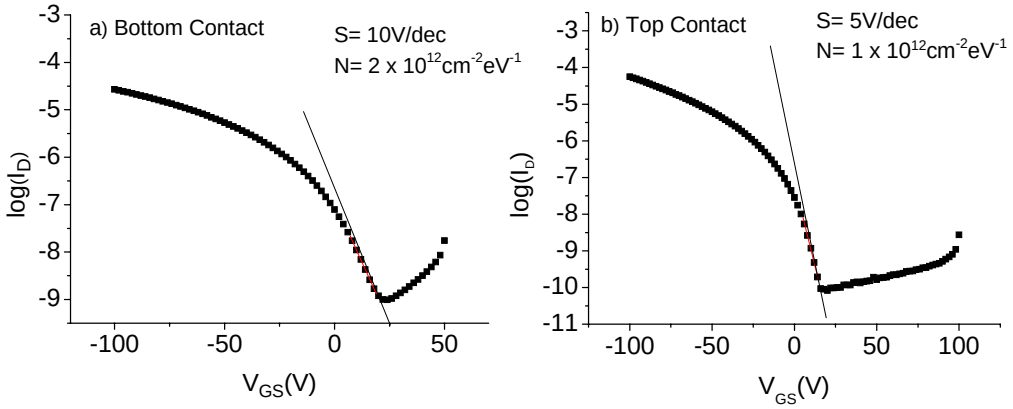

Figure 4.16: Comparison between the sub-threshold slope of BC (a) and TC (b) devices.

It is worth to note that gate electrodes were patterned for both devices (BC and TC) in order to have the same overlapping are with the Source and drain electrodes printed on the opposite side of the Mylar® foil. In fact, having an overlapping between Source and Drain electrodes and the Gate, would lead to have a parasitic capacitor which can be considered as an additional contribute for increasing the electrical hysteresis.

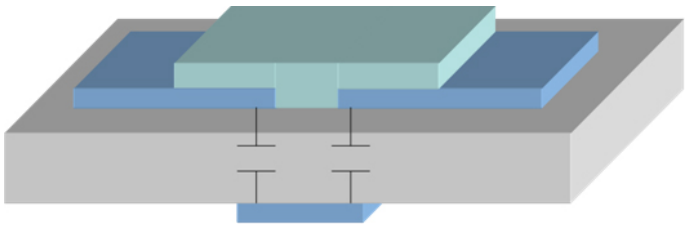

Figure 4.17: Schematic representation of the parasitic capacitors due to the overlapping of Source and Drain electrodes with the gate electrode.

In this case, since the overlapping area is the same for both devices, its contribute should be equal for BC and TC OFETs; any detected difference in the hysteresis can be therefore only be attributed to charge trapping within the active layer.

4.3.2 Gate electrode role in devices behaviour

Interestingly, we investigated the role played by the gate electrode in the electrical behaviour of the assembled devices. Is it important to underline that changing the gate electrodes for these kinds of devices is very simple, since it has been assembled on the back side of the plastic foil. Therefore, it can be easily removed and re-deposited without affecting and polluting the semiconductor film that lies on the opposite side of the foil. As a result, with this technique, it is possible to investigate the effective gate role on the device performances, since the active part of the device is exactly the same (the active layer and the Source and Drain electrodes are the same). For this purpose, we used

three different kinds of gate electrodes: i) a PEDOT: PSS spin-coated film; ii) a PEDOT: PSS drop-cast film. In Figure 4.18 and 4.19 we report the electrical characteristic of BC and TC transistors respectively, characterized with both kind of PEDOT:PSS Gate electrode. As can be clearly noticed, the devices worked perfectly in all configurations. Nevertheless, some interesting differences can be pointed out from this comparison.

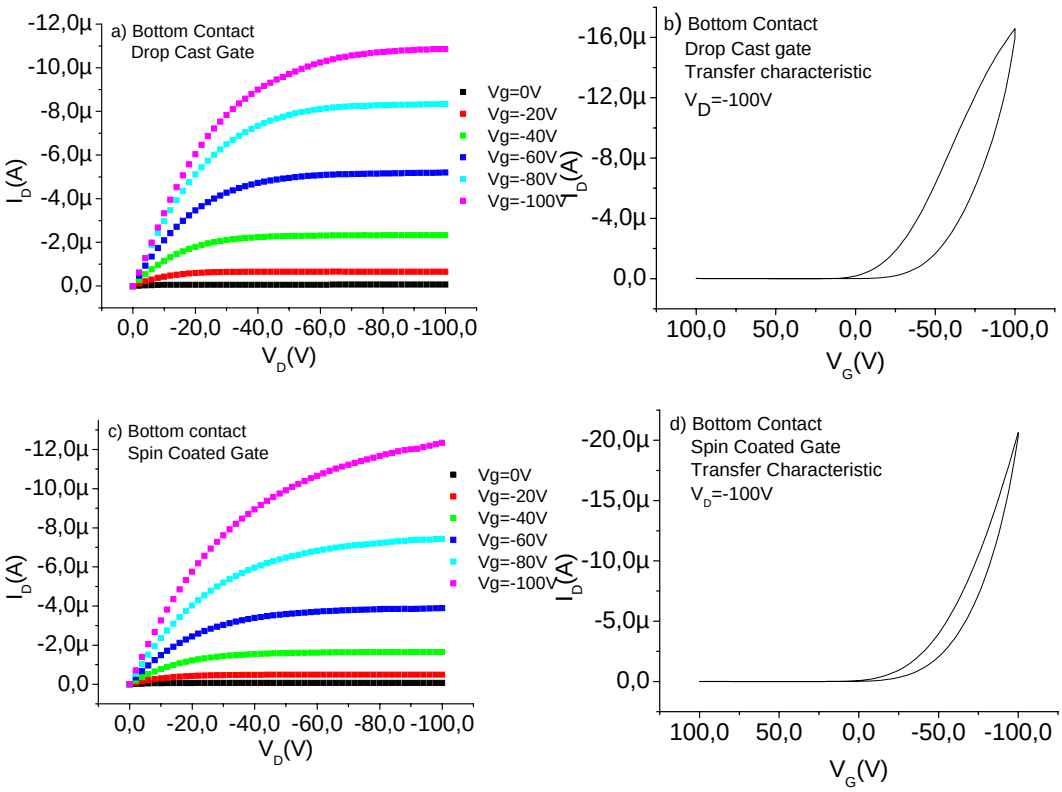

Figure 4.18: Comparison between the electrical behaviour of a BC device with PEDOT:PSS drop cast (a and b) or spin coated (c and d) gate electrodes.

First of all, if we consider in particular the transfer characteristics, it is noticeable a significant increase in the recorded drain current when using a spin coated gate instead of a drop cast one, and this can be seen both in BC and in TC devices. Moreover, it is worth to notice that the hysteresis effect changes by changing the gate structure. This behaviour is more evident in Figure 4.20 where we plot a

comparison between the normalized transfer characteristics. As can be seen, both for spin coated and drop-cast gate devices, hysteresis is more pronounced in BC devices, confirming what already observed in the previous section.

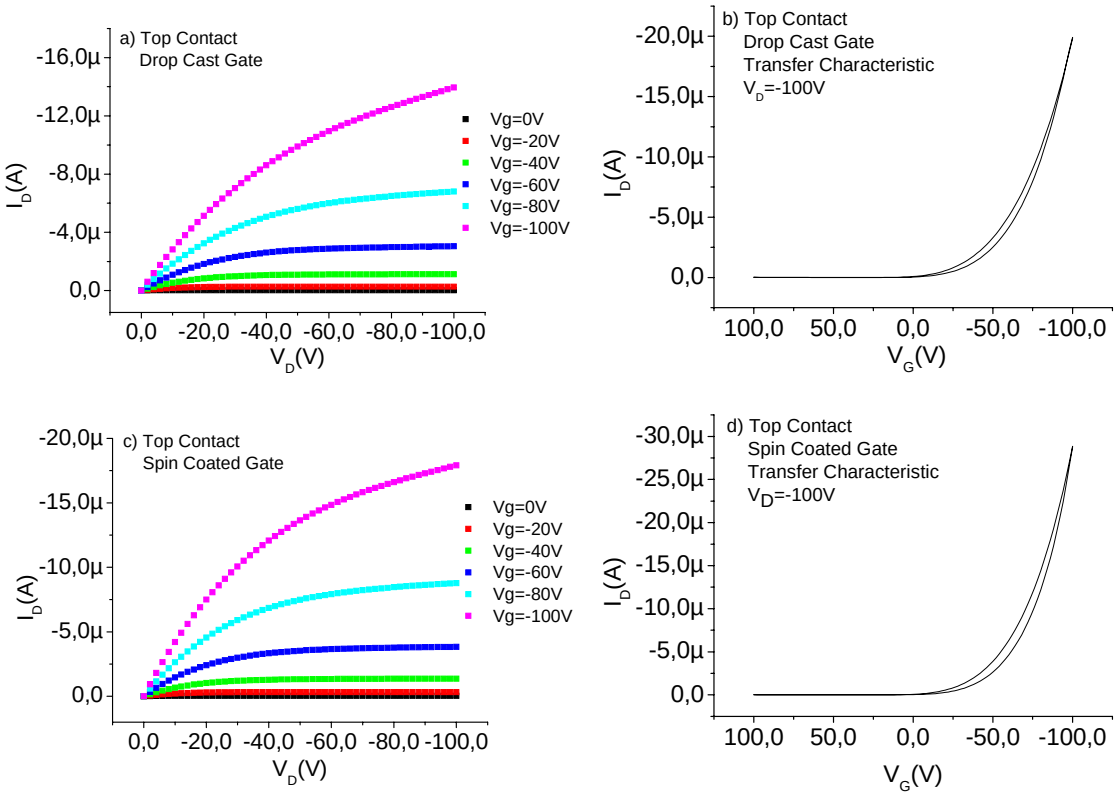

Figure 4.19: Comparison between the electrical behaviour of a TC device with PEDOT:PSS drop cast (a and b) or spin coated (c and d) gate electrodes.

Moreover, hysteresis increases when using a drop cast gate electrode instead of a spin coated one, and this is significant in BC devices whereas is almost negligible in TC ones. As a result, effect is correlated not only to a charge trapping at the organic semiconductor/insulator interface, but also to some parasitic phenomena taking place within the PEDOT: PSS film employed as gate electrode. In fact, PEDOT: PSS is a conductive polymer formed by two

different parts: PEDOT is the conductive part, while the PSS is a non conductive insulating part allows the polymer to be soluble.

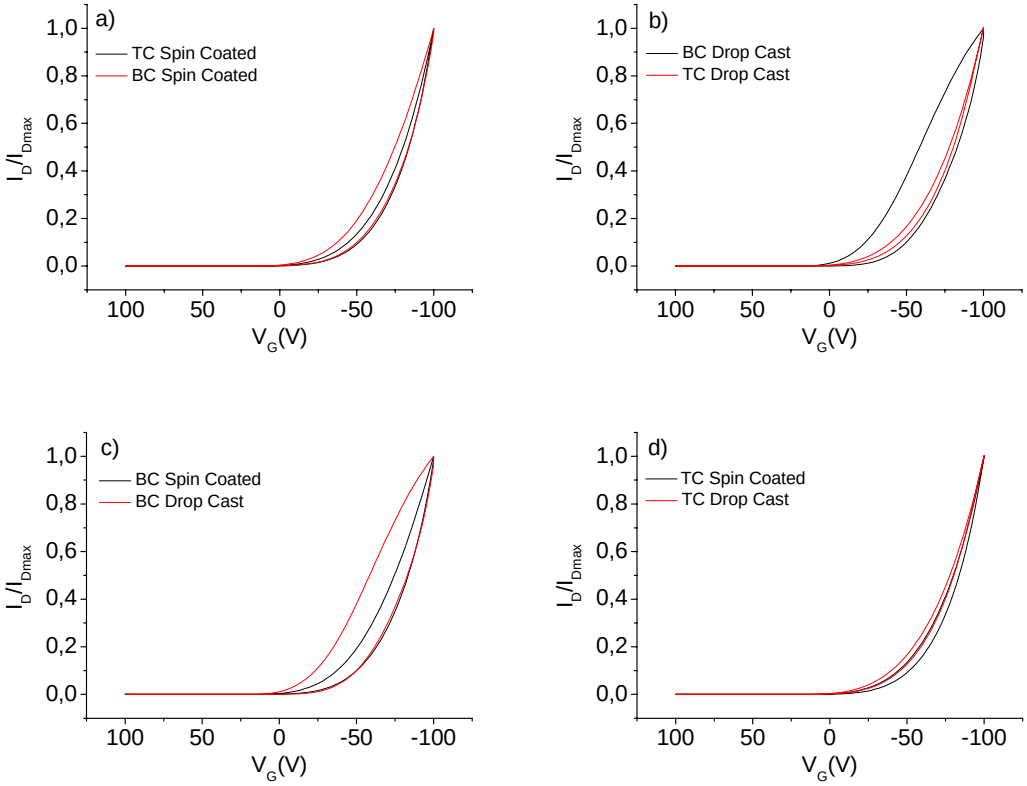

Figure 4.20: Comparison of the hysteresis effect between: B-C Vs T-C devices with spin-coated gate (a); B-C Vs T-C devices with drop-cast gate (b); B-C spin-coated gate Vs B-C drop-cast gate (c); T-C spin-coated gate Vs T-C drop-cast gate (d);

It is well known that after deposition, the PEDOT: PSS film consists of a matrix of a granular structure, namely PEDOT conducting grains, surrounded by islands of PSS, which is insulating. Therefore, the electrical behaviour of a PEDOT: PSS film strongly depends on the PEDOT to PSS ratio within the layer. We speculate that in the case of spin coated films, the excess of PSS is cleaned off from the surface of the PEDOT: PSS grains in the film, creating a better connection between the conducting PEDOT grains and hence better percolation pathways for charge transport. The higher concentration of PSS on the surface for drop-cast films could be, therefore, the main reason for the increase in

the parasitic hysteresis phenomena we observed. This could on one side influence the overall conductivity of the deposited film and, on the other side, can lead to parasitic phenomena such as polarization of PSS islands during the electrical measurements, which can be at the base of the decrease of the recorded current and the increase of the hysteresis behaviour for PEDOT: PSS observed in drop-cast gate devices.

In conclusion, we fabricated fully flexible and transparent all organic FETs on plastic, using a very simple and inexpensive technique that can be a valuable alternative to printing for the mass production of all organic devices for large area electronics. Furthermore, we demonstrated, supported by XPS and AFM investigations, that the devices performances are strongly influenced on one side by the architecture of the devices themselves, and, on the other hand, by structural and morphological properties of the employed materials. In particular different semiconductor/electrodes and semiconductor/insulator interfaces, lead to pronounced differences in the electrical behaviour of these devices. As a matter of fact, T-C devices showed the best performances for the most meaningful electrical parameters, with higher mobility, higher on/off current ratios, and rather lower contact resistance and hysteresis parasitic phenomena.

References

[1] C. D. Dimitrakopoulos and P. R. L. Malenfant, Adv. Mater., 14, 99 (2002).

[2] R. G. Nuzzo, Proc. Natl. Acad. Sci. U.S.A. 98, 4827 (2001).

[3] G. Blanchet and J. Rogers, J. Imaging Sci. Technol. 47, 303 (2003).

[4] M. Lefenfeld, G. Blanchet, and J. Rogers, Adv. Mater., 15, 1188 (2003).

[5] P. Calvert, Chem. Mater. 13, 3299 (2001).

[6] Y. Xia and G. M. Whitesides, Annu. Rev. Mater. Sci. 28, 153 (1998).

[7] V. C. Sundar, J. Zaumseil, V. Podzorov, E. Menard, R. L. Willett, T. Someya, M. E. Gershenson, and J. A. Rogers, Science 303, 1644 (2004).

[8] Y.-L. Loo, R. W. Willett, K. Baldwin, and J. A. Rogers, Appl. Phys. Lett. 81, 562 (2002).

[9] M.M.de Kok, M.Buechel, S.I.E.Vulto, P.van de Weijer, E.A.Meulenkamp, S.H.P.M.de Winter, A.J.G.Mank, H.J.M.Vorstenbosch, C.H.L.Weijtens, and V.van Elsbergen, Phys.Stat.Sol.(a) 201, 1342 (2004).

[10] H.B.Akkerman, P.W.M.Blom, D.M.de Leeuw, and B.de Boer, Nature 441, 69 (2006).

[11] G.Zotti, S.Zecchin, G.Schiavon, F.Louwet, L.Groenendaal, X.Crispin, W.Osikowicz, W.R.Salaneck, and M.Fahlman, Macromolecules 36, 3337 (2003).

[12] G.Greczynski, Th.Kugler, M.Keil, W.Osikowicz, M.Fahlman, and W.R.Salaneck, J.Electron.Spectrosc. 121, 1 (2001).

[13] X.Crispin, S.Marciniak, W.Osikowicz, G.Zotti, A.W.Denier van der Gon, F.Louwet, M.Fahlman, L.Groenendaal, F.De Schryver, and W.R.Salaneck, J. Polym. Sci. B Pol. Phys. 41, 2561 (2003).

[14] T.P.Nguyen and S.A.de Vos, Appl.Surf.Sci 221, 330 (2004).

[15] K.L.Mulfort, J.Ryu, and Q.Zhou, Polymer 44, 3185 (2003).

[16] T. Kawase, T. Shimoda, C. Newsome, H. Sirringhaus and R. H. Friend Thin Solid Films 438, 279 (2003).

[17] G. B. Blanchet, Y.-L. Loo, J. A. Rogers, F. Gao and C. R. Fincher Appl. Phys. Lett. 82, 463 (2003).

[18] E. Becker, R. Parashkov, G. Ginev, D. Schnider, S. Hartmann, F. Brunetti, T. Dobbertin, D. Metzdorf, T. Riedl, H. H. Johannes and W. Kowalsky Appl. Phys. Lett. 83, 4044 (2003).

[19] F.Garnier, A.Yassar, R.Hajlaoui, G.Horowitz, F.Dloffre, B.Servet, S.Ries, and P.Alnot, J.Am.Chem.Soc. 115, 8716 (1993).

[20] J.Stöhr and D.A.Outka, Phys.Rev.B 36, 7891 (1987).

[21] A.Schöll, Y.Zou, Th.Schmidt, R.Fink, and E.Umbach, J.Electron.Spectrosc. 129, 1 (2003).

[22] M.P.de Jong, A.W.Denier van der Gon, X.Crispin, W.Osikowicz, W.R.Salaneck, and L.Groenendaal, J.Chem.Phys. 118, 6495 (2003).

[23] W.Osikowicz, R.Friedlein, P.P.de Jong, S.L.Sorensen, L.Groenendaal, and W.R.Salaneck, New J. Phys. 7, 104 (2005).

[24] H. Peisert, X. Liu, D. Olligs, A. Petr, L. Dunsch, T. Schmidt, T. Chassé, M. Knupfer, J. Appl. Phys. 96, 4009 (2004).

[25] M. Alagia, C. Baldacchini, M. G. Betti, F. Bussolotti, V. Carravetta, U. Ekström, C. Mariani, and S. Stranges, J. Chem. Phys. 122, 124305 (2005).

[26] http://ois.nist.gov/pah.

[27] E. Umbach, M. Sokolowski, and R. Fink, Appl. Phys. A 63, 565 (1996).

Chapter 5

All Organic Ambipolar Field Effect Transistors

In the previous chapter we introduced a novel low cost technique for the realization of all organic FETs. All the characterised devices behaved as unipolar p-type FETs working in accumulation mode. We herein show that it is possible, by employing the same fabrication technique, to obtain also all organic n-type and ambipolar FETs by using a double layer bulk heterojunction as organic semiconductor layer.

5.1 Introduction

One of the main characteristics of almost all organic semiconductors is that, despite their undoped state, often only a single carrier transport, either holes (in most cases) [1, 2] or electrons [3-5], can be realized. In several cases, the work function of metals employed for contact fabrication dictated the polarity of charge transport [6]. As a consequence, still today the realization of ambipolar OFETs remains a challenge. The simultaneous transport of both types of carriers could lead to a simplification in the design of complementary logic circuits, allowing at the same time to reduce power dissipation and to increase noise margins. The main problem for the realization of ambipolar

OFETs seems to be the choice of right materials to be employed in the devices assembly.

In principle, most organic semiconductors may allow both kinds of charge carriers transport [7]. Therefore, in OFETs, achieving n-type or p-type conduction should mainly depend on the metal employed as source and drain electrodes, which should enable the injection of one type of charge carriers into the semiconductor layer. In fact, charge injection strongly depends on the energy level matching between the Fermi-level of the source and drain electrodes and the organic semiconductor energy levels, *i.e*, the transport levels derived from the lowest unoccupied molecular orbital (LUMO) and highest occupied molecular orbital (HOMO). Very recently Takenobu et al. [6] showed that the choice of an appropriate pair of high and low work function metals as source and drain electrodes can lead to an improvement and balance of carrier injection into the channel.

Nevertheless, there exist reports on efficient n-type OFETs employing gold electrodes, despite rather high electron injection barriers [8, 9]. On the contrary, it is difficult to obtain n-type conduction even in devices with low work function electrodes [10].

In these cases, it seems that the cause for the lack of n-type conduction could be electron trapping at the interface between the gate dielectric and the organic semiconductor. Chua et al. have suggested that, in most cases, electron conduction in organic devices is inhibited by electron trapping at the interface due to a high concentration of hydroxyl groups that act as traps for electrons [11]. Therefore, it seems that the quality of the substrate used for the growth of an n-type material is the critical point for obtaining this type of conduction.

5.2 Achieving n-type transport by means of bulk heterojunctions

The appealing possibility to use different structures as active layers, such as polymer blends and bulk hetero-junctions has attracted

great interest recently. They have been extensively employed for optimizing the electrical and optoelectronic properties in organic solar cells and light emitting diodes, but in the last years a lot of effort has been addressed also in the filed of OFETs and OLETs. Combining together a suitable couple of organic semiconductor could in principle allow to obtain both kind of charge carrier transport (holes and electrons). We already demonstrated (see the previous chapter) the possibility of fabricate all organic FETs by a very easy and flexible low cost technique, namely μCP. This technique allowed to realized unipolar p-type OFETs working in accumulation mode. In this section we demonstrate that it is possible to achieve n-type conduction in OFETs also employing polymeric Source and Drain electrodes made out with PEDOT:PSS and patterned by μCP. We choose Fullerene C_{60} as suitable n-type organic semiconductor. The main characteristics of this compound were already introduced in the first chapter of this thesis. In fact, C_{60} is one of the most employed n-type organic materials, due to its relatively high electron affinity which allow to minimize the electron injection barrier even when high work function metals (such as Au and Al) are used for the fabrication of Source and Drain electrodes. C_{60} unfortunately has also some drawbacks, first of all, as the major of n-type organic semiconductors, it is very unstable and it quickly oxidised upon exposure to air. Moreover, it shows poor orientation control and a small grain size (around 50nm.), even when deposited under very strict conditions onto very flat surface, such as SiO_2. As a consequence, the resulting low crystallinity of the deposited films seriously degrades the performances of C_{60} OFETs. Nevertheless, very recently Itaka et al. [12] demonstrated that controlling the wetting of a substrate by a molecular overlayer can improve the crystal quality of organic semiconductor films, which in turn is favorable for efficient charge transport, see Figure 5.1. They showed that depositing a thin pentacene layer (1 or 2

monolayers) prior to the deposition of a C_{60} layer leads to an increase of the n-type mobility if compared to a single C_{60} layer device.

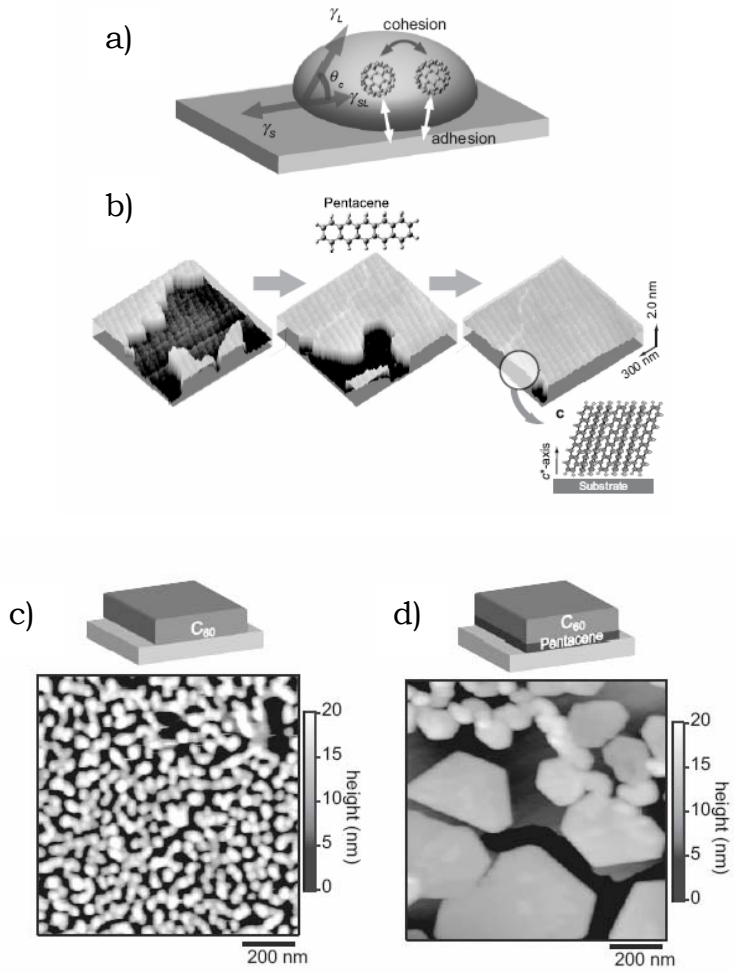

Figure 5.1: a) Schematic representation of organic compounds on a substrate with poor wettability; b) AFM images of a thickness-gradient pentacene thin film library with layer thickness varying from 0.5 to 1 monolayer, grown on atomically flat sapphire (0001) substrate. c) AFM images of C60 thin films grown on a sapphire substrate without and with (d) a thin pentacene buffer layer [12].

We fabricated two sets of devices; in the first case we used a single layer structure by employing C_{60} as organic semiconductor. In the second case, following the considerations drawn by Itaka et al. we employed a double layer structure, using a very thin pentacene buffer

layer (nominal thickness 3nm.) in order to improve the quality of the C_{60} film subsequently deposited. Pentacene and C_{60} were evaporated from resistively heated Al_2O_3 crucibles in a custom-made vacuum chamber (base pressure 5×10^{-8} mbar). The amount of deposit and the evaporation rate (typically 5 Å/min) were monitored by a quartz crystal microbalance placed next to the substrate. As can be clearly noticed from Figure 5.2 where the device structure is depicted, a fully flexible and transparent (see inset) structure was finally obtained. All devices were realized in "top contact" configuration by printing the source and drain electrodes after the organic semiconductor deposition, since this structure already allowed to obtain unipolar p-type OFETs with mobilities up to 0.1 cm^2/Vs and I_{on}/I_{off} ratios around 10^5, see Figure 5.2.

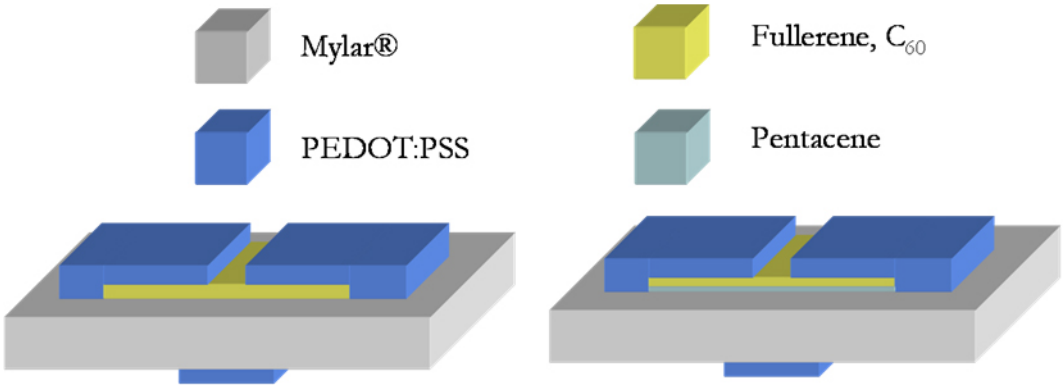

Figure 5.2: Schematic representation of the devices assembled in TC configuration, without (left) and with (right) a thin pentacene buffer layer.

The first set of devices, realized by employing a single layer C_{60} structure, did not show n-type conduction. One possible reason for this could be the rather large electron injection barrier at the PEDOT:PSS/C_{60} interface, which could be estimated to be ca. 1.9 eV under ultrahigh-vacuum conditions [13]. Note that in our case the C_{60} layer was exposed to air prior to PEDOT:PSS printing, and therefore the value for the electron injection barrier may vary. In addition, a poor

structural and morphological quality of the C_{60} layer on bare Mylar® could also be invoked as a cause for device failure. In fact, the high surface roughness of Mylar® (Root Mean Square Roughness = 1.2 nm), can cause a high concentration of defects (i.e. charge traps) within the active layer, thus inhibiting electron transport through the channel. Interestingly, when a 3 nm pentacene buffer-layer (ca. 2 layers of vertically inclined pentacene molecules) is used, the C_{60} layer grows much more uniform and it is even crystalline, as it will be shown in the XRD data reported in the following section. Electrical measurements performed on the devices obtained with the 3 nm Pentacene buffer layer, have shown that the improvement in C_{60} film crystallinity immediately resulted in a clear n-type device behavior, as can be seen in Fig. 5.3. Despite the possibly high electron injection barrier (see above) a clear field effect is visible, and the electron mobility (estimated from the transfer characteristics in the saturation regime) was *ca.* 3.2×10^{-5} cm^2/Vs.

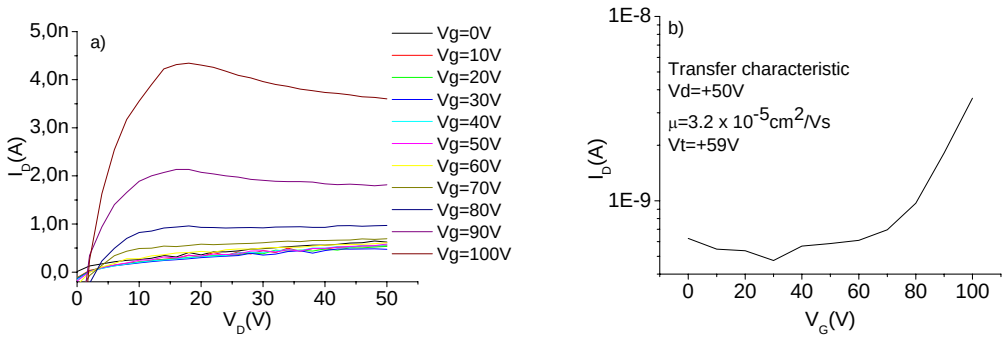

Figure 5.3: Typical Output (a) and transfer (b) characteristics of Top Contact FETs realized with a 3nm pentacene buffer layer and 30nm C_{60} layer. The device works as a unipolar n-type FET.

Interestingly, this may indicate that the structural quality of the semiconductor film, and as a consequence, charge trapping in the channel, is more important than the barrier height for achieving n-type charge transport. In addition, using Pentacene as buffer-layer allowed

to obtain, an all organic n-type FET also with polymeric contacts. Note that despite the presence of a thin Pentacene layer, no p-type conduction was measured in this type of devices. Since Pentacene exhibits pronounced island growth on rough substrates such as Mylar®, no complete monolayer over the entire gate dielectric surface could probably be formed. Thus, the absence of a continuous percolation path is assumed to be the main reason for the lack of hole conduction within the channel.

5.3 Ambipolar Transport in All Organic FETs

Since the absence of a continuous percolation path seems to be the main reason for the lack of hole carrier transport within the channel, we fabricated devices with thicker Pentacene buffer-layers (nominal thickness 20 nm) in order to ensure the formation of a percolation path and, consequently, to obtain also hole transport across the device channel. As can be seen in Figure 5.4, this strategy led to ambipolar behavior, which can be noticed both from the output and transfer characteristics of the devices. It is worth to note that having a complete and continuous Pentacene layer at the interface with the gate dielectric led not only to obtain hole transport across the channel, but also to a clear improvement in the electron mobility. This implies that C_{60} can grow even more uniformly and crystalline when the Pentacene buffer-layer is thick enough to cover the whole insulator surface, forming a complete and continuous film. Despite the very high electron injection barrier, and the fact that all devices were measured in air, we obtained hole mobilities up to $1x10^{-2}$ cm^2/Vs and electron mobilities up to $3.5x10^{-4}$ cm^2/Vs.

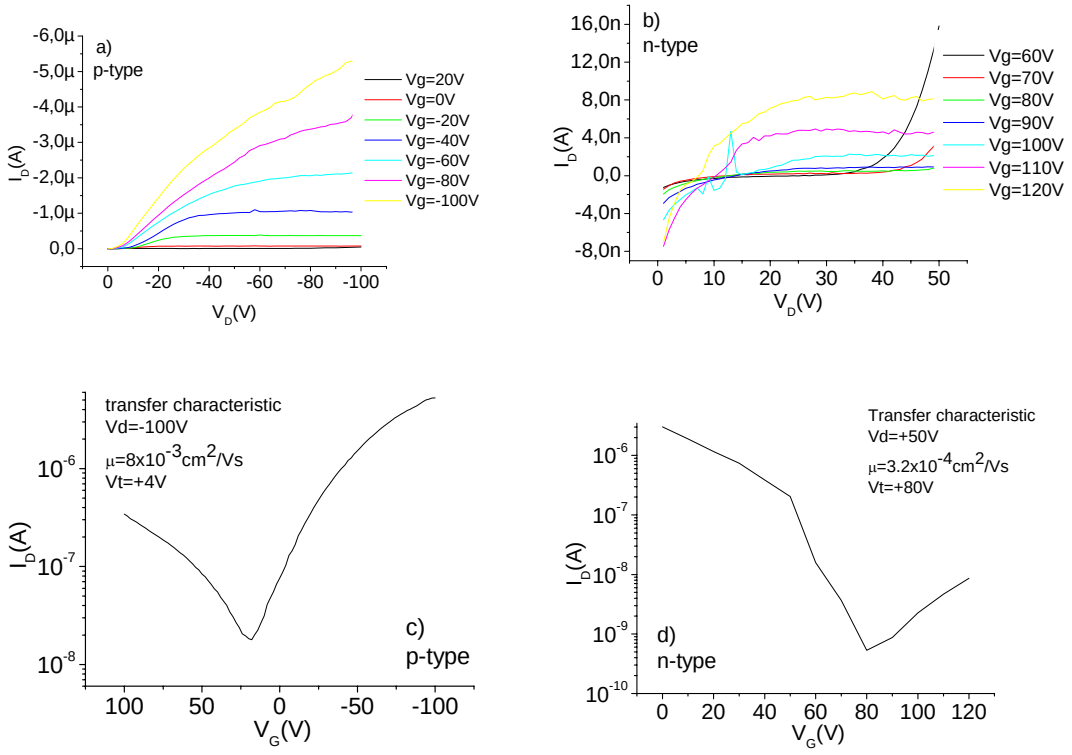

Figure 5.4: Electrical characteristics of a Top Contact all organic ambipolar FET realized with 20nm pentacene buffer layer and 30 nm C_{60} layer. a) Output characteristic of the device working in p-type mode; b) Output characteristic of the device working in n-type mode; c) transfer characteristic of the device working in p-type mode; d) transfer characteristic of the device working in n-type mode.

These results are further supported by X-Ray diffraction analysis which are reported in the following section.

5.3.1 XRD and AFM Characterization

Experimental

X-ray diffraction measurements have been performed at the beamline W1.1 at the synchrotron radiation source HASYLAB (Hamburg, Germany) using a wavelength of 1.1808 nm. In order to achieve a flat substrate surface, Mylar® foil was fixed on quartz coupons (area 1cm^2)

using double-sided adhesive tape. The vacuum-deposition process was identical to the case of OFET preparation as described above.

Atomic Force Microscopy (AFM) measurements were performed in Tapping Mode™ with a Nanoscope III device (Veeco Instruments).

Structural investigations

We performed specular x-ray diffraction scans on both 60nm thick C_{60} films deposited on the pure Mylar® substrate (spectrum (e) in Figure 5.5) as well as on Mylar pre-covered with a layer of nominally 10nm Pentacene (curve (d)). A 20nm thick Pentacene film was investigated as reference for the underlayer (curve (b)). Within the pure Pentacene film, the peak at a value of the momentum transfer (q_z) of 0.4085 $Å^{-1}$ (lattice spacing d=1.538 nm) and its weak second order peak at 0.813$Å^{-1}$ can be assigned to reflections of the (001) and (002) net planes of a well known P polymorph that is usually referred to as *Pentacene thin film phase* [10, 14, 15]. The 60nm thick film of C_{60} deposited directly on Mylar® does not show any Bragg peaks, in contrast to the film of equal nominal thickness deposited on a 10nm thick Pentacene underlayer. We find a peak at q_z=0.7720 $Å^{-1}$ (lattice spacing d=0.814nm) that can be assigned to the (111) reflection of cubic C_{60} polymorphs [16, 17] as well as to the (002) reflection of hexagonally grown C_{60} [17], which cannot be distinguished from our data. This result is in accordance to previous findings for C_{60} vacuum-deposition on sapphire, where crystalline growth of C_{60} took place exclusively after pre-coverage of the substrate with a monolayer of Pentacene [12]. However, a film of 30nm C_{60} on 3nm Pentacene, which corresponds to nominally two monolayers of Pentacene, did not exhibit any indication of crystalline C_{60} growth in x-ray diffraction (not shown). We attribute this to the pronounced island growth of Pentacene on Mylar® due to the high surface roughness of the substrate. Hence, the nominally 20nm thick film of Pentacene (Figure

5.5 curve (b)) exhibits an out-of-plane crystalline coherence length of 30±5nm as estimated from the (001) reflection under the use of the Scherrer formula [18]. Therefore the 3nm Pentacene film can be regarded as far from being closed, leaving areas uncovered for the subsequent C_{60} deposition and thus increasing its amorphous ratio, which can explain the worse ambipolar performance of devices based on that structure.

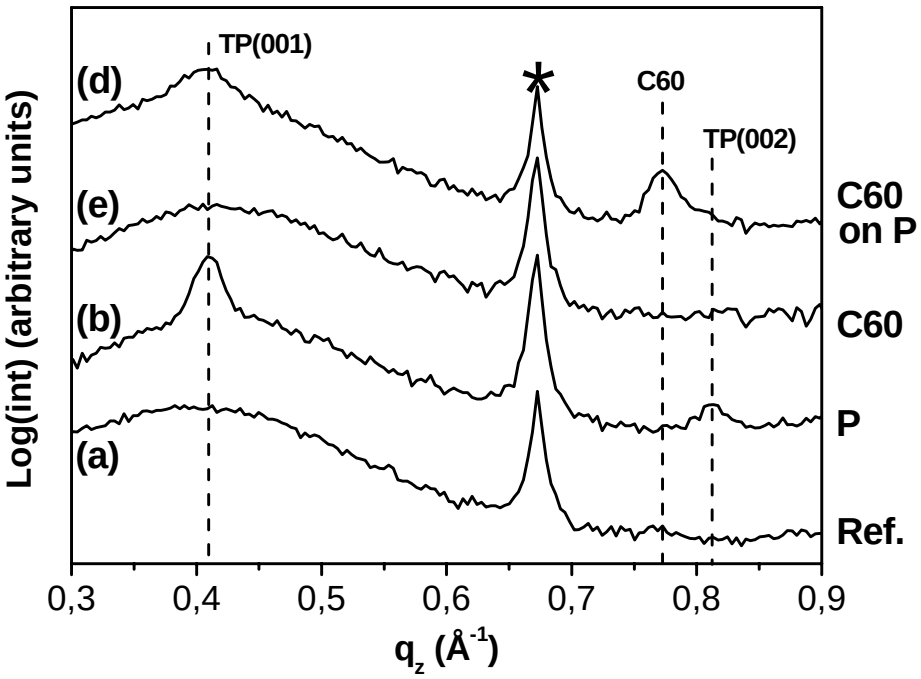

Figure 5.5: Specular x-ray diffraction scans on the Mylar/tape/quartz substrate as reference (a), a film of 20nm Pentacene (b), a layer of 60nm C_{60} (c) and a film of 60nm C_{60} on 10nm Pentacene (d). Precoverage of the substrate with P leads to crystalline growth of C_{60}. TP(hkl) denotes reflections of planes (hkl) originating from the Pentacene thin film phase (see text). The star marks a substrate contribution.

Moreover, by the analysis of the AFM micrographs reported in Figure 5.6, some other interesting conclusions can be drawn. C_{60} grown on bare Mylar® (b) is characterised by a granular structure with an grain density of 3000 μm^{-2} (grain diameter < 30nm). From Figure 5.6 (c)

we can clearly notice that under the use of a pentacene buffer layer, C_{60} grains nucleate over the underlying pentacene islands, which leads to a reduction of the island density by a factor of 3 (see Figure 5.6 (c)). Together with our finding of crystalline C_{60} growth from XRD, this explains the enhancement in the electron mobility we observed in the OFETs characteristics.

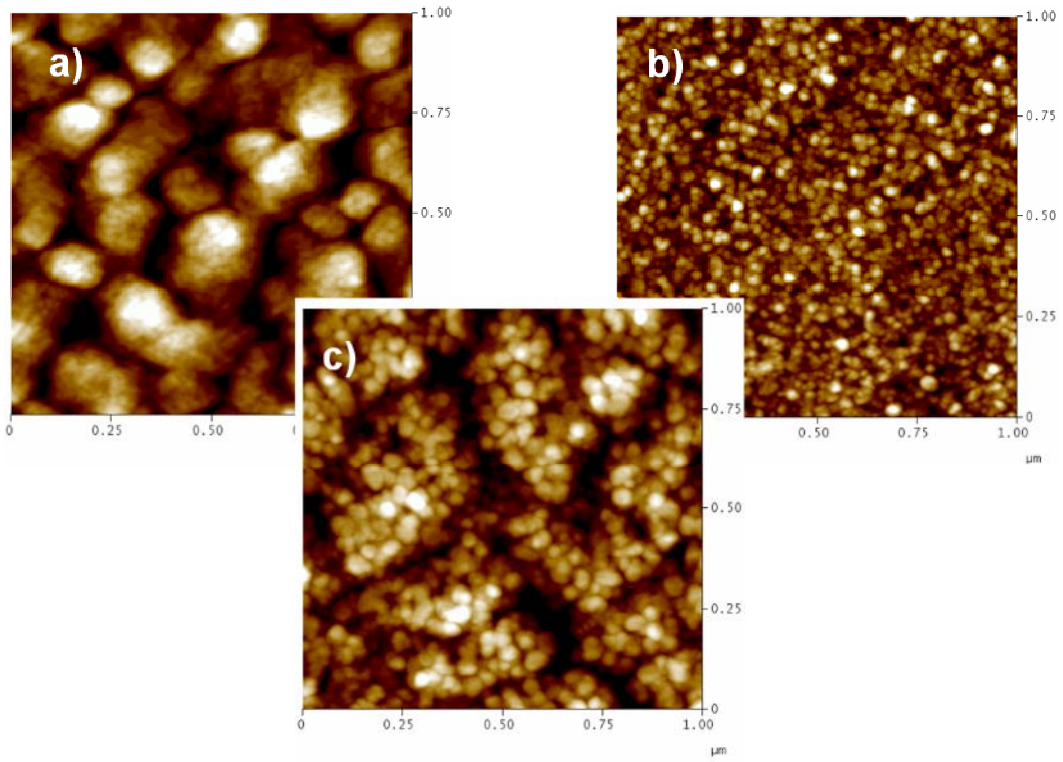

Figure 5.6: Atomic Force Microscopy (AFM) micrographs of 1x1□m showing: 20 nm. pentacene on bare Mylar® (a); 60 nm C_{60} on bare Mylar® (b); and a film of 60nm C_{60} on 10 nm pentacene. The precoverage of the substrate with pentacene leads to an increase in the average grain dimension. The color range represents 0-20 nm in (a), (c) and 0-10 nm in (b).

5.4 A comparison between all organic ambipolar FETs with different architectures

In order to have a comparison between different OFETs architectures, we realized all organic FETs both in Bottom Contact and

Top Contact configurations and we employed Pentacene/C_{60} heterojunctions realized by double layer structures and also by a blend phase obtained by co-evaporating both organic semiconductors at the same time and at the same nominal rate, in order to have an equal percentage of both materials. We herein report the obtained results.

As can be seen from the Figures 5.7 and 5.8 reported in the following pages, all devices worked as ambipolar FETs. Nevertheless, some interesting differences can be pointed out.

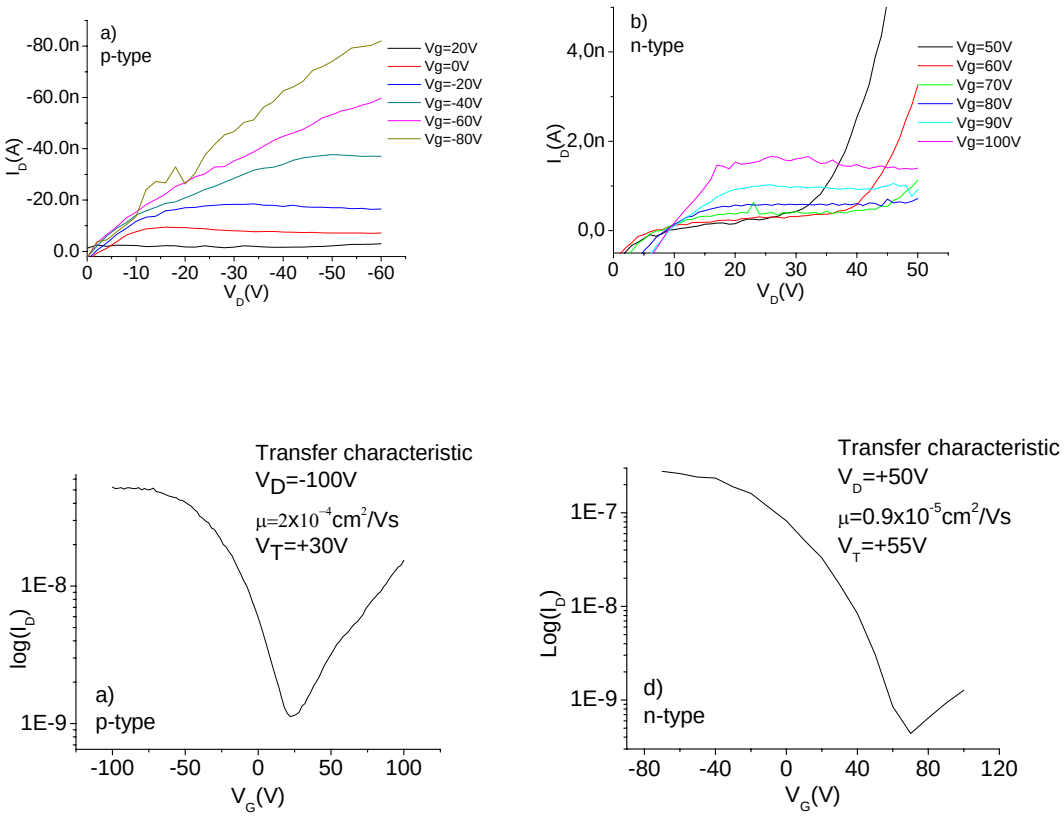

Figure 5.7: Electrical characteristics of a Bottom Contact all organic ambipolar FET realized with 20nm pentacene buffer layer and 30 nm C_{60} layer. a) Output characteristic of the device working in p-type mode; b) Output characteristic of the device working in n-type mode; c) transfer characteristic of the device working in p-type mode; d) transfer characteristic of the device working in n-type mode.

For example, even though the field effect behaviour is clearly visible, BC device in the double layer configurations are characterized by mobilities that are almost one order of magnitude lower than those recorded for the same kind of devices in TC transistors, and this is visible either for hole and electron mobility. It is worth to note that for both type of devices, BC and TC, the organic semiconductor deposition was performed in the same conditions, same chamber pressure, and deposition rate and thicknesses for both the employed organic semiconductors. Therefore, as we already stated in the previous chapter, the structure of the device itself strongly influence its electrical performances.

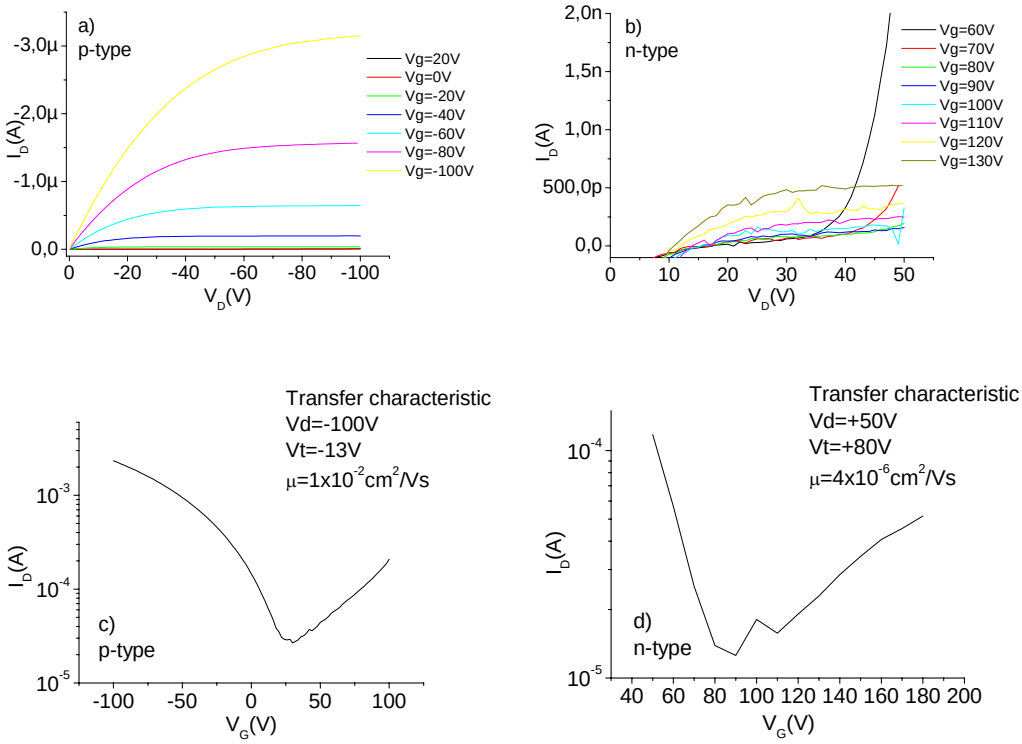

Figure 5.8: Electrical characteristics of a Top Contact all organic ambipolar FET realized by co-evaporating a 30 nm Pentacene/C60. a) Output characteristic of the device working in p-type mode; b) Output characteristic of the device working in n-type mode; c) transfer characteristic of the device working in p-type mode; d) transfer characteristic of the device working in n-type mode.

Other interesting differences can be seen by analysing the behaviour of BC and TC OFETs realized with a co-evaporated film as active layer. In this case we did not noticed any significant difference between BC and TC devices in the electron mobility, whereas the difference is much more evident in the case of hole mobility. In fact, electron mobility is almost equal while hole mobility is one order of magnitude higher for TC transistors. Indeed, this could be an indication that charge traps for holes are mostly localized at the electrode/semiconductor interface, whereas charge traps for electrons at the interface between dielectric and semiconductor.

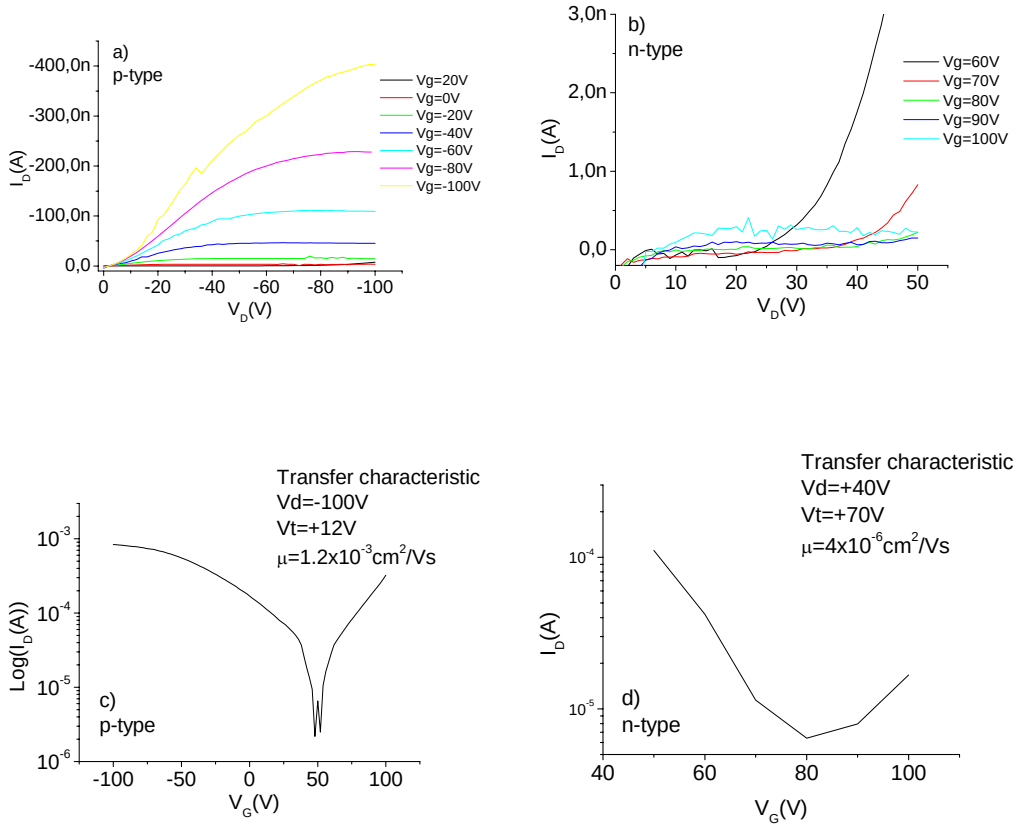

Figure 5.9: Electrical characteristics of a Bottom Contact all organic ambipolar FET realized by co-evaporating a 30 nm Pentacene/C60. a) Output characteristic of the device working in p-type mode; b) Output characteristic of the device working in n-type mode; c) transfer characteristic of the device working in p-type mode; d) transfer characteristic of the device working in n-type mode.

Interestingly, if we compare the electrical performance of the co-evaporated FETs (both BC and TC) with those recorded in the double layer devices, it is clear that while hole mobility does not change significantly, electron mobility drops down by orders of magnitude for both configurations, BC and TC. This behaviour can be easily explained if we consider the morphological characteristics of the active layer in the co-evaporated films. In fact, the co-deposition at the same time of both materials is not sufficient to let C_{60} grow in a crystalline phase. While Pentacene films are characterized by the same crystal structure obtained for thin films deposited onto bare Mylar® substrate, C_{60} films are almost amorphous or show very poor grade of crystallinity upon co-evaporations. This can explain why we did not see any significant difference in the mobility measured for BC or TC devices; we assume that the density of defects induced by the co-deposition is higher than that induced by the discontinuity of the pre-patterned source and drain electrodes. Nevertheless, a clear difference is still visible when we consider the hole mobility; in fact, since the deposited film (even in the co-evaporated phase) still shows a crystalline structure, in this case the defects induced by the pre-patterned electrodes can strongly influenced charge carrier transport as underlined in the previous chapter.

In conclusion, in this chapter we demonstrated the possibility of fabricating fully flexible and transparent all-organic n-type and ambipolar OFETs on plastic substrates by employing a double layer architecture comprising Pentacene and C_{60} as active layer. It was shown that the use of a Pentacene buffer-layer on the rough dielectric polymer led to an improvement of the crystallinty in the C_{60} active layer, allowing to obtain n-type conduction. Moreover, it was also shown that by completing the Pentacene buffer-layer to form a continuous layer, ambipolar device behavior could be obtained. In addition, this further increased the electron mobility in C_{60} by one order on magnitude. These results confirm the importance of the substrate quality for controlling

transport properties and even the type of charge carrier in organic semiconductor thin films.

References

[1] S.F Collins, G. W. Baxter, S. A. Wade, T. Sun, K. T. V. Grattan, Z. Y. Zhang, and A. W. Palmer, J. of Appl. Phys. 84, 4649 (1998)

[2] Y.-Y. Lin, D. J. Gundlach, S. F. Nelson, and T. J. Jackson, IEEE Electron Device Lett., 18, 606 (1997).

[3] N. Tessler, N. T. Harrison, D. S. Thomas, R. H. Friend, Appl. Phys. Lett., 73, 732 (1998).

[4] S. Kobayashi, T. Takenobu, S. Mori, A. Fujiwara, and Y. Isawa, Appl. Phys. Lett. 82, 4581 (2003).

[5] S. A. Wade, S. F. Collins, G. W. Baxter, J. of Appl. Phys., 94, 4743 (2003).

[6] T. Takenobu, T. Takahashi, J. Takeya, and Y. Iwasa, Appl. Phys. Lett. 90, 013507 (2007).

[7] E. C. P. Smits, T. D. Anthopoulos, S. Setayesh, E. van Veenendaal, R. Coehoorn, P. W. Blom, B. de Boer, and D. M. de Leeuw, Phys. Rev. B, 73, 205316 (2006).

[8] A. Facchetti, M. Mushrush, H. E. Katz and T. J. Marks, Adv. Mater. 15, 33 (2003).

[9] T. B. Singh, F. Meghdadi, S. Gunes, N. Marjanovic, G. Horowitz, P. Lang, S. Bauer, N. S. Sariciftci, Adv. Mater. 17, 2315 (2005).

[10] C. D. Dimitrakopoulos, P. R. L. Malenfant, Adv. Mat. 14, 99 (2002).

[11] L.-L. Chua, J. Zaumseil, J.-F. Chang, E. C.-W. Ou, P. K.-H. Ho, H. Sirringhaus and R. H. Friend, Nature, 434, 194 (2005).

[12] K. Itaka, M. Yamashiro, J. Yamaguchi, M. Haemori, S. Yaginuma, Y. Matsumoto, M. Kondo, and H. Koinuma, Adv. Mater. 18, 1713 (2006).

[13] F. J. Zhang, A. Vollmer, J. Zhang, Z. Xu, J. P. Rabe, N. Koch, Org. Electron., submitted.

[14] S. Fritz, S. Martin, C. Frisbie, M. Ward, and M. Toney, J. Am. Chem. Soc. 126, 4084 (2004).

[15] M. Oehzelt, R. Resel, C. Suess, R. Friedlein, and W. R. Salaneck, J. Chem. Phys. 124, 054711 (2006).

[16] S. Liu, Y.J. Lu, M. M. Kappes, J. A. Ibers, Science 254, 408 (1991).

[17] J. L. de Boer, S. van Smaalen, V. Petricek, M. Dusek, M. A. Verheijen, G. Meijer, Chem. Phys. Lett. 219, 469 (1994).

[18] P. Scherrer, Nachr. Ges. Wiss. Göttingen, 98 (26. Sept. 1918).

Chapter 6

Tuning the electrical properties in OFETs by means of organic bulk heterojunctions

Organic bulk heterojunctions represent indeed a very powerful tool for tuning and optimizing the optoelectronic properties in organic devices. In particular they have been extensively employed for the realization of Organic Solar Cells, and OLEDs with the aim of improving exciton dissociation or charge recombination by combining a suitable couple of n-type and p-type organic semiconductors [1-6]. Very recently, they have been also employed in the field of OFETs and OLETs for obtaining ambipolar conduction [7-10]; for example, in the previous chapter we demonstrated that by using a suitable couple of materials it is possible to realize all organic ambipolar FETs. In this chapter we show that bulk heterojunction can be employed also for tuning other electrical parameters in OFETs. We fabricated OFETs on Mylar® plastic substrates, starting from the structures we introduced in the previous chapters, and we present a comparative study using the same basic device structure but employing different organic semiconductor materials and morphologies. Morphology variation is achieved by

controlled co-evaporation of two dissimilar materials. The electrical device performances were investigated, focusing, in particular, on the extraction of parameters that can be correlated to the insulator/organic semiconductor interface. As active organic material forming the channel we chose α-sexithiophene (6T: Sigma Aldrich) and α,ω-dihexylsexithiophene (DH6T: H. C. Stark GmbH) and the following sample notation will be used: pure 6T (A), pure DH6T (B). All organic molecular layers were deposited by thermal evaporation at pressure below $2x10^{-7}$mbar, at a constant rate around 4Å/min; the film thickness was monitored by a quartz crystal microbalance.

6.1 α-sexithiophene (6T) and α,ω-dihexylsexithiophene (DH6T) OFETs

All devices characterised in these sections were realized on Mylar® using two different configurations: i) Bottom Contact with Au electrodes; ii) top contact with PEDOT:PSS electrodes. In figure 6.1 we show the schematic of the assembled devices. Since DH6T showed a very poor adhesion onto Mylar® surface, it was not possible to print the PEDOT:PSS electrodes by employing μCP.

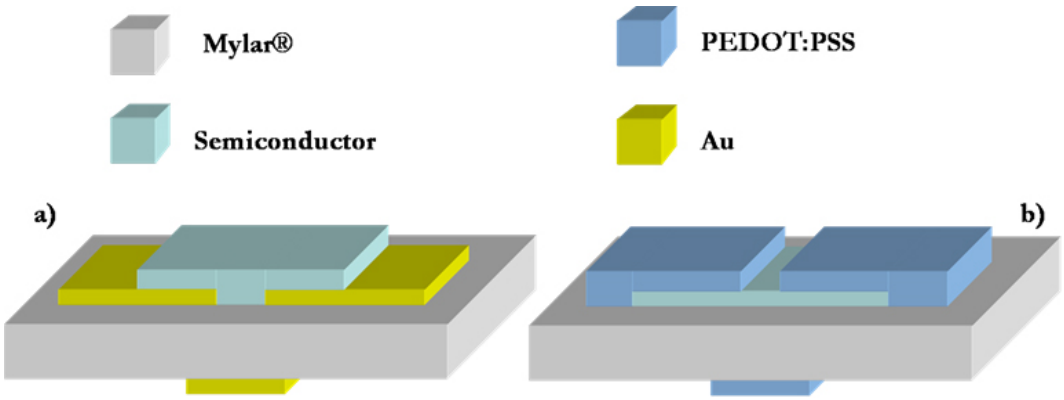

Figure 6.1: Schematic representation of Bottom Contact devices with Au electrodes (a); and Top Contact devices with PEDOT:PSS electrodes (b).

In fact, upon removing the PDMS stamp from the surface after the printing process, in most cases we observed a transfer of the DH6T from Mylar® surface to the PDMS stamp. All organic FETs with DH6T were therefore realized by means of a lamination process. First, two thin Au pads were patterned onto Mylar® surface vie deposition through a shadow mask; after this, the organic semiconductor was deposited on the free Mylar® surface. In the last step we put the patterned PDMS stamp (were we already spun a thin PEDOT:PSS film) in contact with the sample surface in order to realise a contact between the Source and Drain electrodes with the two previously deposited Au pads, see Figure 6.2. In this way it is possible to have an indirect access to Source and Drain electrodes by connecting the microprobe station tips to the gold pads.

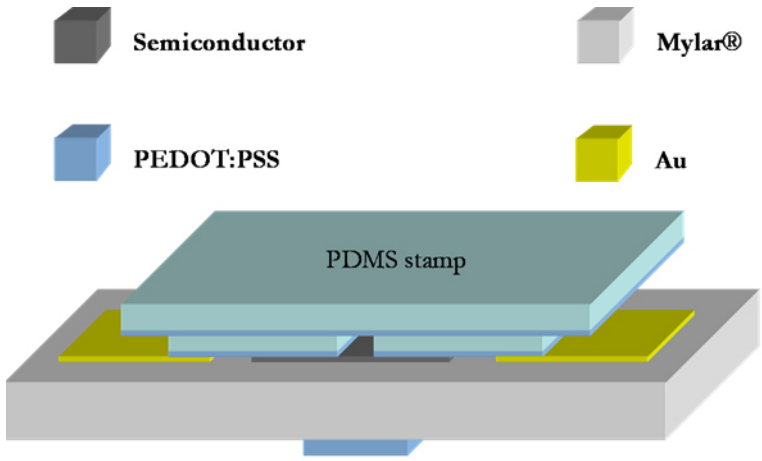

Figure 6.2: Lamination process employed for contacting DH6T OFETs.

As can be noticed from the output and transfer characteristics reported in the following Figure 6.3 and 6.4 all devices worked perfectly as unipolar p-type FETs. However, some interesting differences can be pointed out. First of all, DH6T samples showed channel mobility higher by one order of magnitude if compared to 6T samples. The average

mobilities for 6T samples are around $8x10^{-3}cm^2/Vs$ whereas mobilities up to $5x10^{-2}cm^2/Vs$ were estimated for DH6T devices, and these data are in full agreement to what has been reported in literature for 6T and DH6T FETs.

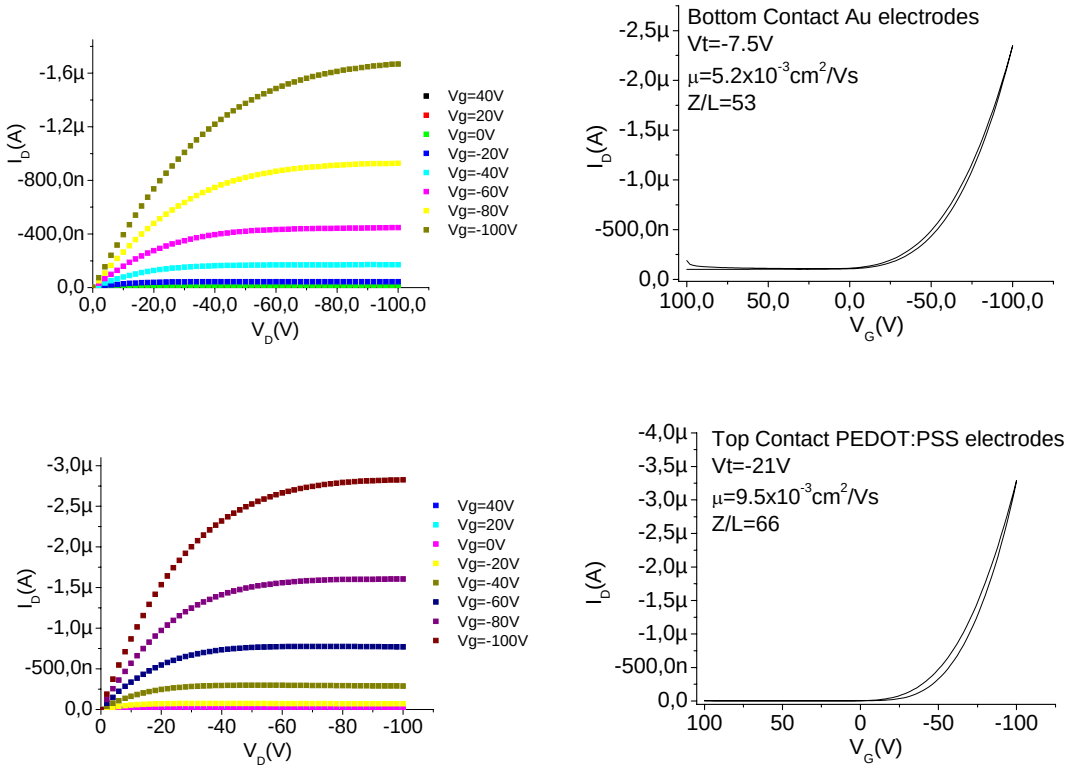

Figure 6.3: Output and Transfer characteristics of 6T OFETs.

One more point which need to be empathized is that 6T samples are characterised by a threshold voltage ranging form -7V to -20V for BC Au electrodes and TC PEDOT:PSS electrodes respectively, therefore they are turned off for gate voltages around zero and, as typical transistors working in accumulation regime, they can be switched on by applying a negative gate voltage sufficient to collect a number of hole high enough to form a complete channel. On the contrary, DH6T samples show a very high positive threshold voltage. This means that the channel is already formed without applying any gate voltage, therefore they are in their ON state even when the gate voltage is equal

to zero. A high positive gate voltage is required in order to repel hole from the channel and turn the device off.

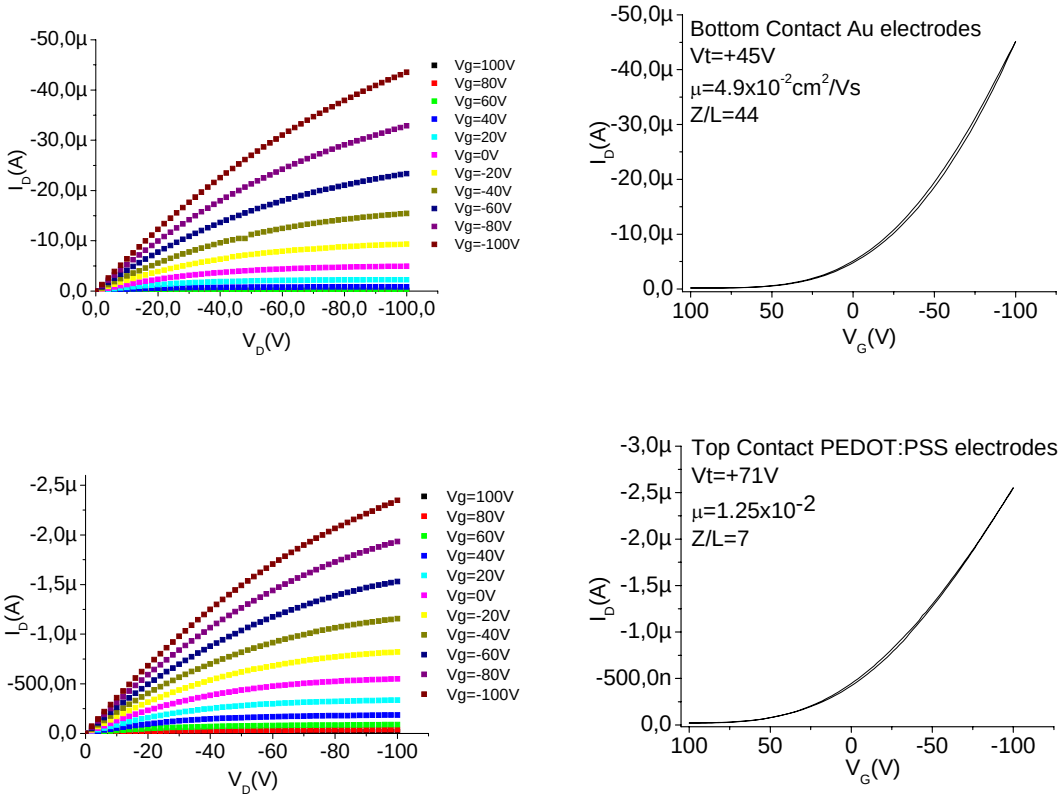

Figure 6.4: Output and Transfer characteristics of DH6T OFETs.

Despite their very similar chemical structure, 6T and DH6T semiconductor lead to a very different electrical behaviour. Very recently, Duhm et al. [11] reported a different hole injection barrier for DH6T (with respect to 6T) in a monolayer device (ΔE=0.15eV) and in a multilayer device (ΔE=0.80eV) deposited on a metal, Ag (111) substrate. They attribute the origin of the unexpected lower BE of a multilayer DH6T film compared to the ML to the hexyl substitution, and to an associated abrupt change in molecular orientation in the thin film after ML completion. In fact, a defined transition from lying to vertically inclined molecules was observed for DH6T/Ag, see Figure 6.5. Therefore, the reported difference in hole injection barrier for the two

materials, has been ascribed to differences in the growth mode and in the insulating properties of the hexyl substituents, leading to different electronic properties with respect to 6T [11]. When 6T and derivatives are deposited on insulating materials the formation of a first layer with the molecule long axis parallel to the substrate is not observed (there's no affinity between π-structure and insulator). As a consequence, the molecules fully adopt the closed-packed structure from the first layer at the interface with the insulator. Presumably, the shift of the work function between 6T and DH6T that is to be considered in the case of the samples we realized on Mylar® should be ΔE=0.80eV.

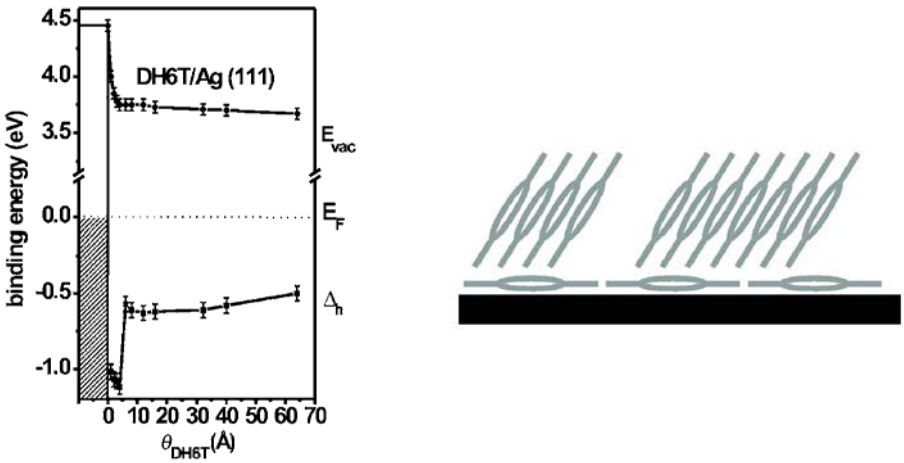

Figure 6.5: Schematic energy level diagram (derived from UPS) for DH6T on Ag(111).θ_{DH6T} denotes the DH6T thickness, E_{vac} the vacuum level, and Δ_h the hole injection barrier (HOMO onset). E_F is the Fermi level of the metal substrate (a). Sketch of the proposed growth model of DH6T/Ag(111), with lying monolayer and almost standing multilayer.

Moreover, we assume that the presence of the alkyl chains as substituents has an inductive effect on the distribution of charge in the molecule. This effect is amplified when the orientation of the dipole is parallel to the direction of charge delocalization (i.e. the conjugation direction). This dipole generates a non-uniform potential in the molecule

(qualitatively reported in Figure 6.6) which possibly increases the average energy of the electrons in the π-orbitals, thus rigidly shifting towards higher energies the energy levels of the unsubstituted molecule.

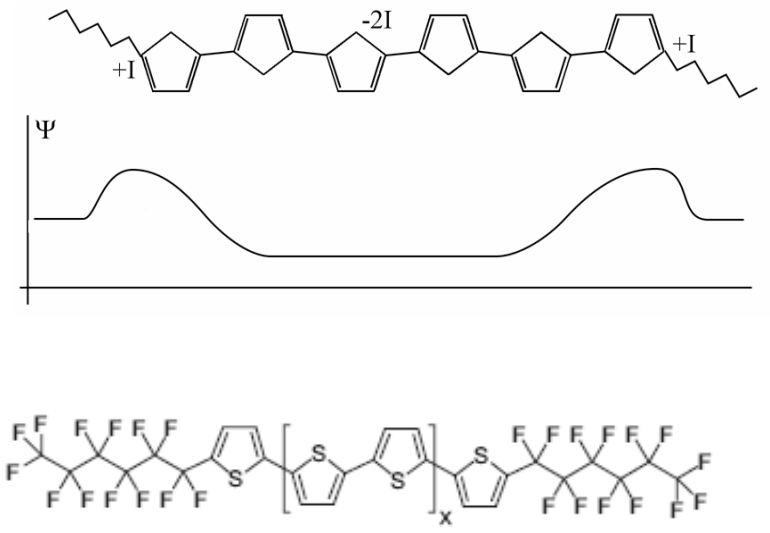

Figure 6.6: Qualitative sketch of the dipole induced by the alkyl chains substituents (upper); DFH6T molecule (lower).

As a matter of fact, the tiophene ring is electron-rich and all known unsubstituted tiophene oligomers are p-type. A σ-electron donating alkyl substitution is an effect that enhances this properties (using the inductive effect notation =+I). Moreover, very recently, Facchetti et al. [12] reported the functionalization of 6T with perfluoro alkyl chains (see Figure 6.6). They show that OFETs realized with DFH6T as the active material are characterised by n-type behaviour, whereas, with the same device structure, DH6T shows p-type behaviour. Since the crystalline structure is very similar to DH6T close-packed structure, the different behaviour between 6T, DH6T and DFH6T cannot be only ascribed to differences in morphology or crystalline structure.

In the case of DFH6T, it can be that the fluoralkyl substituents may impart sufficient σ-electron-withdrawing capacity (using the

inductive effect notation =-I) to lower the HOMO-LUMO core energies allowing electron injection to exceed hole injection, thus allowing to obtain n-type behaviour.

As a matter of fact, in light of what above reported the following conclusions can be suggested. If we assume the presence of aligned and interacting molecular dipoles, the increase in mobility observed for DH6T can be understood as an effect of the electrostatic potential generated inside the material. The very small differences in the packing, orientation and electronic structure of the two materials can only impart small perturbations to their electronic transport properties. Moreover, it is well known that FET behaviour is based upon the difference between the Fermi level difference of the gate contact and the semiconductor. If we consider the Metal Insulator Semiconductor (MIS) structure, the Fermi level must be the same for the whole structure. If the metal and the semiconductor Fermi levels are equal, the junction should not change the band structure of the semiconductor. If there is a difference between the Fermi levels of the two materials, an electron transfer from the higher energy Fermi level to the lower one will take place, until equilibrium is reached, thus resulting in a continuum Fermi level. Since a metal has generally a higher electron density if compared to organic semiconductors, the Fermi level shift will be more pronounced for these rather than for the metal. As a consequence, when considering the MIS junction band diagram, we can take a fixed metal Fermi level and consider only the Fermi level shift in the organic semiconductor. Therefore, when $E_F^s > E_F^m$ an upwards band banding will take place, and if the difference is high enough an accumulation of positive charges (holes) at the interface with the insulator can occur.

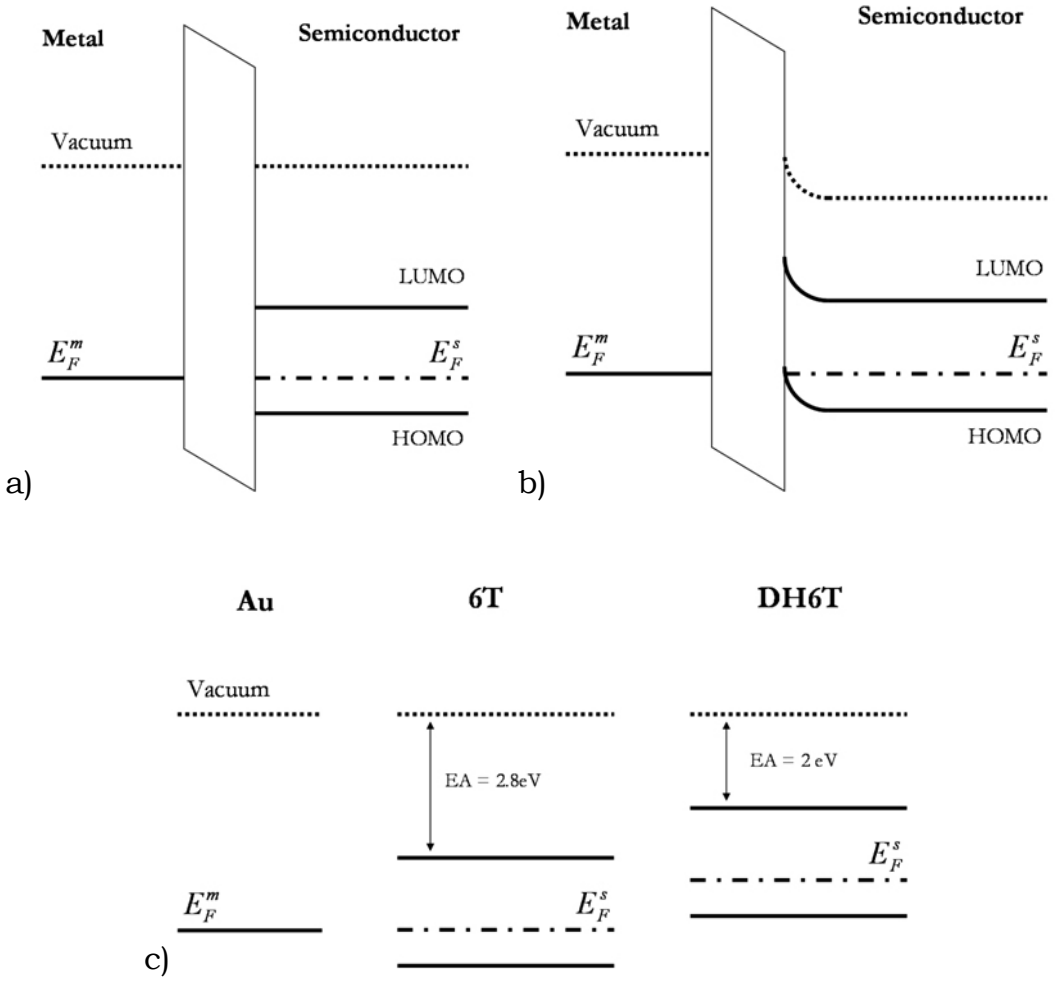

Figure 6.7: MIS representation for $E_F^s \approx E_F^m$ (a) and $E_F^s > E_F^m$ (b); Au, 6T and DH6T band diagrams (c).

In light of these considerations, the observed shift in the threshold voltage towards positive voltages (depletion OFET) suggests a higher Fermi level energy for DH6T than that for 6T. Very interestingly the work function shift reported by Duhm when DH6T molecules are arranged in a close packed structure (ΔE=0.80eV) could thus account for the observed formation of an accumulation layer in the 100% DH6T FET analysed. In fact, if we assume a higher electron affinity for 6T, when realizing the MIS junction of the FET the higher energy difference between DH6T and gold (relative to the difference between 6T and gold)

causes a bending of the energy bands that creates an accumulation layer which may be responsible for the FET ON-state at 0 gate voltage.

6.2 OFETs with co-evaporated films as active layer

In the previous section we have shown that, despite their very similar chemical structure, 6T and DH6T (when used as active semiconductor layer in OFETs) lead to significant differences in the most meaningful electrical parameters (i.e. mobility, threshold voltage). In this section we want to demonstrate that it is possible to modulate the electrical behaviour of the final devices by using the same materials in a mixed phase. For this purpose, we fabricated a set of samples by depositing both organic semiconductors at the same time upon a co-evaporation process, and we employed different ratios of the two compounds. In the specific, we realized co-evaporated OFETs with the following blend ratios: 75% 6T – 25% DH6T; 50% 6T – 50% DH6T; 25% 6T – 75% DH6T.

In the following pages we show the output and transfer characteristics recorded for all the assembled devices and we summarise the most meaningful parameter in order to give a clear and complete view.

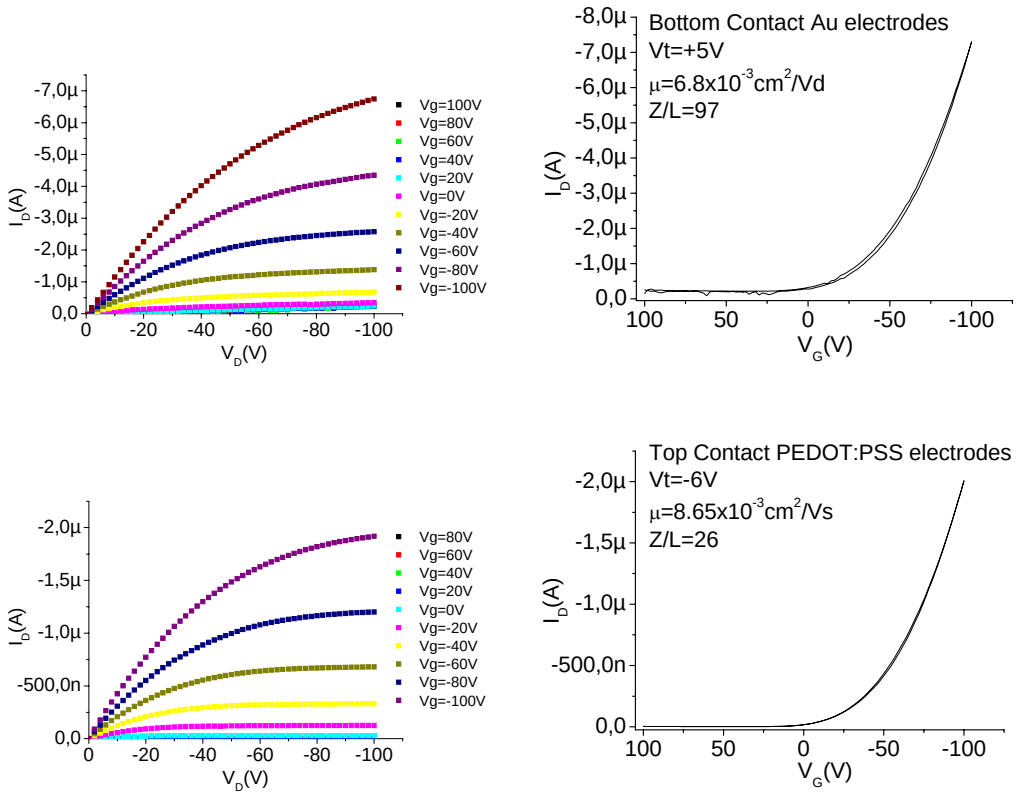

Figure 6.8: Output and Transfer characteristics recorded in co-evaporated samples with 30% DH6T – 70% 6T.

Bottom Contact Au Electrodes	**6T**	**70%6T 30%DH6T**	**50%6T 50%DH6T**	**30%6T 70%DH6T**	**DH6T**
Mobility (cm^2/Vs)	5.3 x 10^{-3}	6.8 x 10^{-3}	8.8 x 10^{-3}	8.7 x 10^{-3}	4.5 x 10^{-2}
Threshold Voltage (V)	-7.5	+5	+11	+12.5	+45

Table 6.I: Tabulation of the mobility and threshold voltages for different blend ratios.

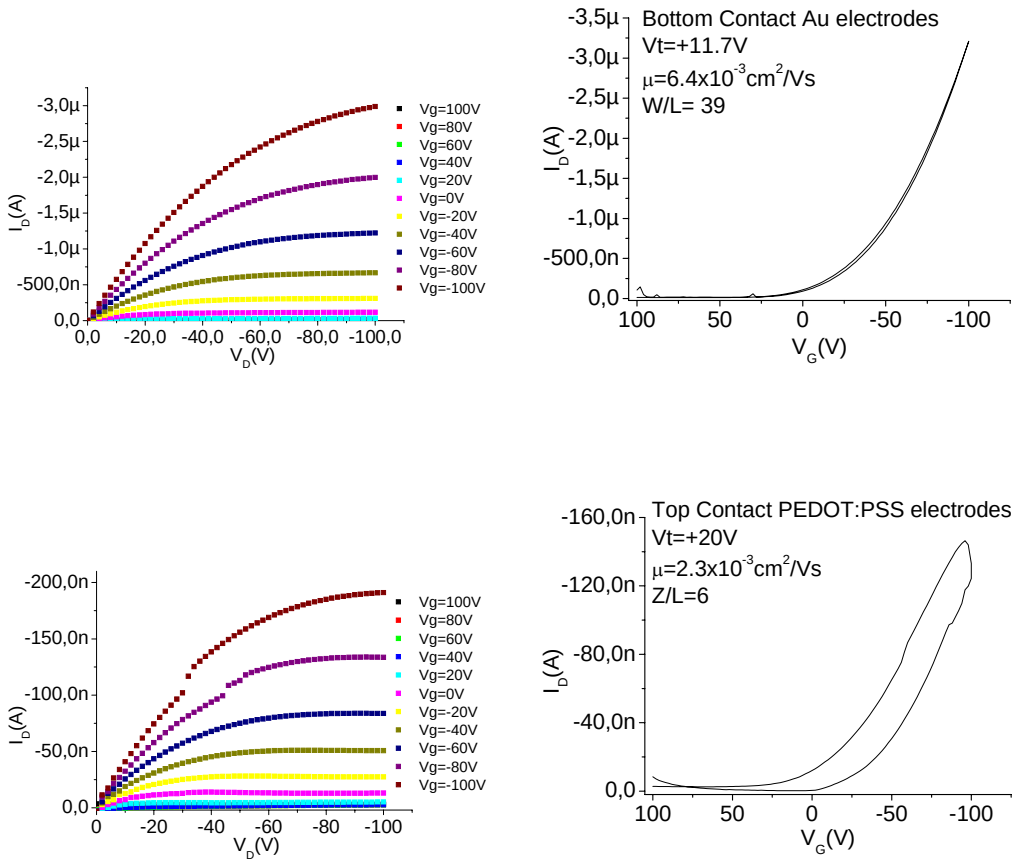

Figure 6.9: Output and Transfer characteristics recorded in co-evaporated samples with 50% DH6T – 50% 6T.

Top Contact PDT:PSS Electrodes	**6T**	**70%6T 30%DH6T**	**50%6T 50%DH6T**	**30%6T 70%DH6T**	**DH6T**
Mobility (cm^2/Vs)	9.5×10^{-3}	1.1×10^{-2}	2.3×10^{-3}	2.5×10^{-2}	5×10^{-2}
Threshold voltage (V)	-21	-6	+20	+45	+65

Table 6.II: Tabulation of the mobility and threshold voltages for different blend ratios.

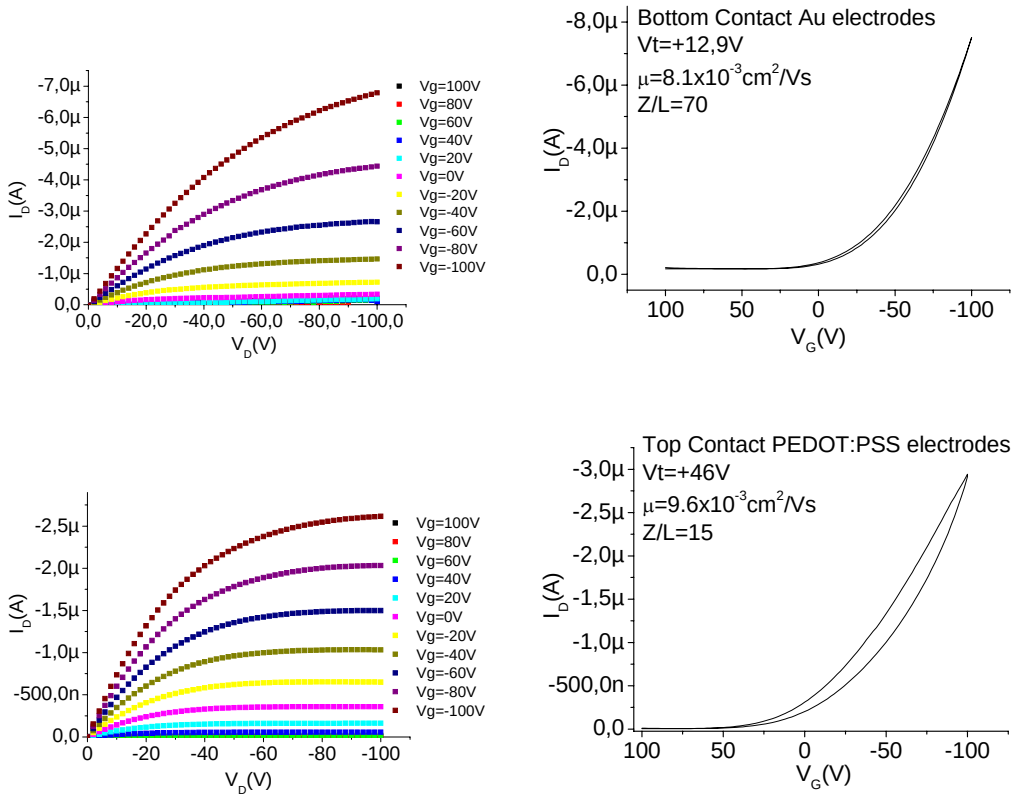

Figure 6.10: Output and Transfer characteristics recorded in co-evaporated samples with 70% DH6T – 30% 6T.

Once again, as we can clearly see from the Figures reported in this section showing the output and transfer characteristic of the assembled devices, all OFETs realized by means of co-evaporations worked as unipolar p-type transistors. Nevertheless, there are some interesting points that need to be empathised.

6.2.1 Analysis of the threshold voltage

As it can be clearly seen from Figure 6.11 we observed, both for BC Au electrodes and TC PEDOT:PSS electrodes OFETs, a clear trend in the threshold voltages by varying the relative percentage of the two compounds within the co-evaporated film. This is much more evident

for PEDOT:PSS devices where we found an almost linear dependence of the threshold voltage from the 6T percentage in the mixed film.

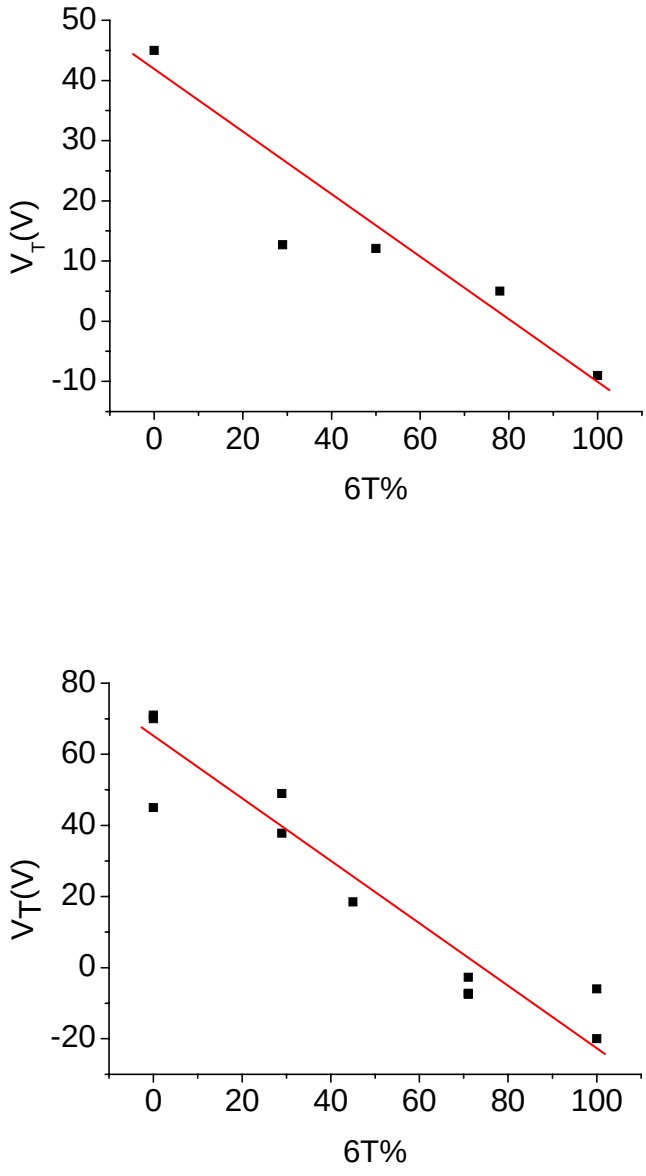

Figure 6.11: Threshold voltage as function of 6T percentage within the co-evaporated film. Bottom contact Au electrodes (upper) and Top Contact PEDOT:PSS electrodes (lower).

In the previous section we motivated the DH6T samples behaviour with the possibility of a "cross-talking" between molecular dipoles

present on the alkyl substituted molecules (DH6T) that strengthens its intensity in a close packed structure and that thus depends on the packing of the molecules. We can assume an averaging of the dipole strength over the nearest neighbours of a DH6T molecule in the case of 6T-DH6T blends. This could in part explain the reason for the shift of the threshold voltage as a function of the percentage of DH6T we observed. However, further investigations will be addressed in the early future in order to better understand the physical process at the basis of this behaviour.

6.2.2 Analysis of the mobility

It is worth underlying that co-depositing two dissimilar organic materials should lead to the "artificial" introduction of structural defects simultaneously, thus giving place to an increase of the density of defects within the active layer. As a consequence a dramatic decrease (even by orders of magnitude) of the mobilities recorded in the co-evaporated samples should to be expected. As we can notice from Table 6.I and 6.II this was not the case, and mobilities in the co-evaporated samples are comprised in the range defined by the two extreme value of composition (100% 6T or 100% DH6T)

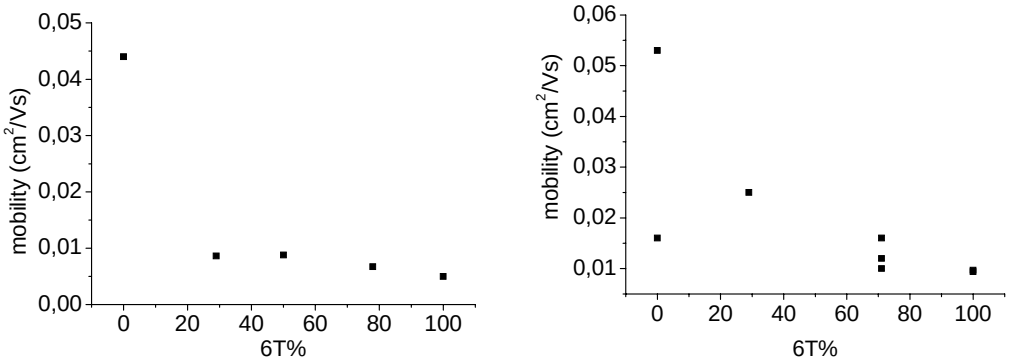

Figure 6.12: Channel mobility as function of 6T percentage within the co-evaporated film. Bottom contact Au electrodes (left) and Top Contact PEDOT:PSS electrodes (right).

In order to enlighten such phenomenon, we performed Atomic Force Microscopy investigations on all the deposited active layers, both in the single and in the blend phase.

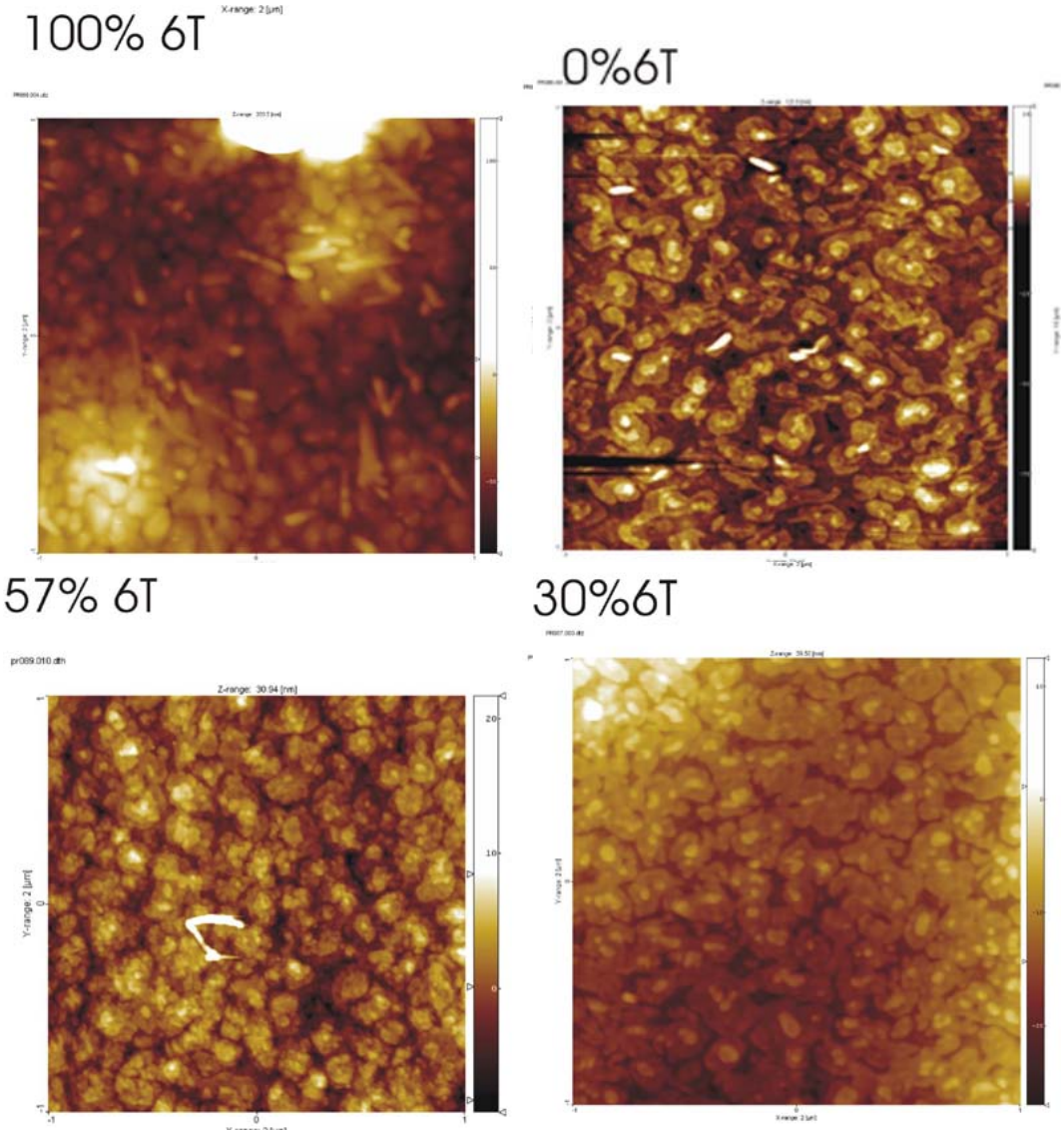

Figure 6.13: AFM micrographs for different 6T-DH6T ratios films. The relative percentage of the two compounds is reported in the pictures.

As can be clearly seen in Figure 6.13, no phase separation occurs upon co-evaporating the two dissimilar materials. Therefore, the density of structural defects (as grain boundaries for instance) should not

change too much and the two species seems to be well intercalated within the deposited film, where DH6T molecules seem to adapt their orientation to the surrounding environment. The co-evaporated films show a typical layer by layer growth where terraces are still visible, even though the roughness of the terraces within the blend film seems to be higher than the one obtained for single materials.

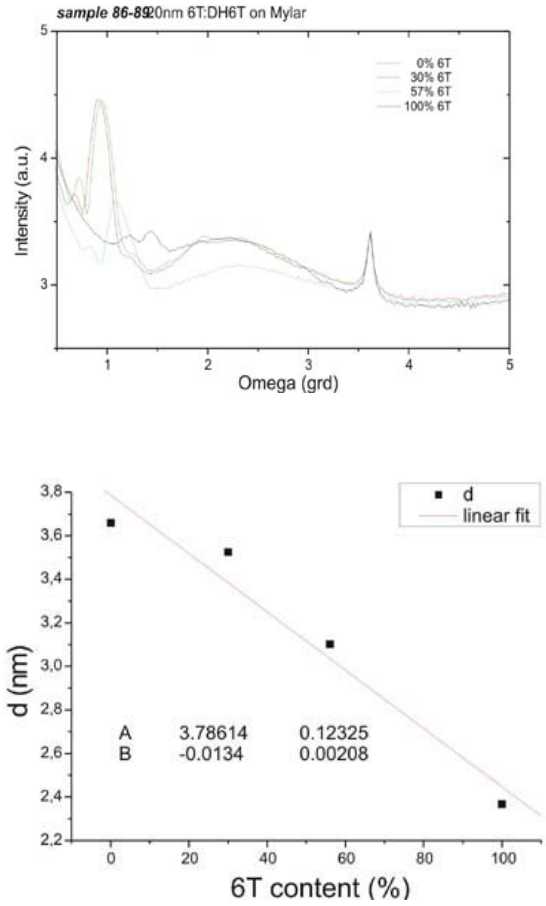

Figure 6.14: XRD spectra (upper) and interlayer d spacing as function of 6T percentage (lower).

These last observations are supported by XRD analysis performed on the same samples and shown in Figure 6.14. From these data it is possible to note a linear shift of the first monolayer d-spacing from 2.2

nm. to 3.8 nm. upon increasing the percentage of DH6T in the film (Note that the reported values correspond to the molecule length of 6T and DH6T respectively). As a result, DH6T molecules change their molecular inclination as a function of the density of 6T molecules within the film.

6.3 Photocurrent Measurements

All photocurrent measurements were performed on the devices fabricated in Bottom Contact configuration with Au Source and Drain electrodes. The measurements were realized keeping the gate electrode floating and applying a nominal 9V voltage between Source and Drain electrodes. As can be seen from Figure 6.15 where we report the recorded photocurrent spectra, no significant difference can be noticed upon changing the blend composition. The only difference that can be pointed out is the dependence of the signal/noise ratio from the percentage of DH6T within the co-evaporated film. In fact, the photocurrent signal is given by the ratio between the increment in the measured current induced by photo-generation and the bulk current of the material ($\Delta I_{ph}/I_0$). If the I_0 value is too high, the amount of photo-generated carriers could not be enough to obtain a significant value of the $\Delta I_{ph}/I_0$ ratio, thus resulting in a rather noisy signal. Therefore, this is in accordance with the data we obtained in OFETs measurements. In fact DH6T samples are characterized by a very high positive threshold voltage, as a result there is charge accumulation at the interface with the gate dielectric even without applying any gate bias. Moreover, in the previous sections we demonstrated that the threshold voltage shift almost linearly as function of the DH6T percentage. If this is true, it is expectable to obtain an almost regular noise increase in the recorded photocurrent spectra upon increasing the percentage of DH6T within the active layer, as can be seen in Figure 6.15.

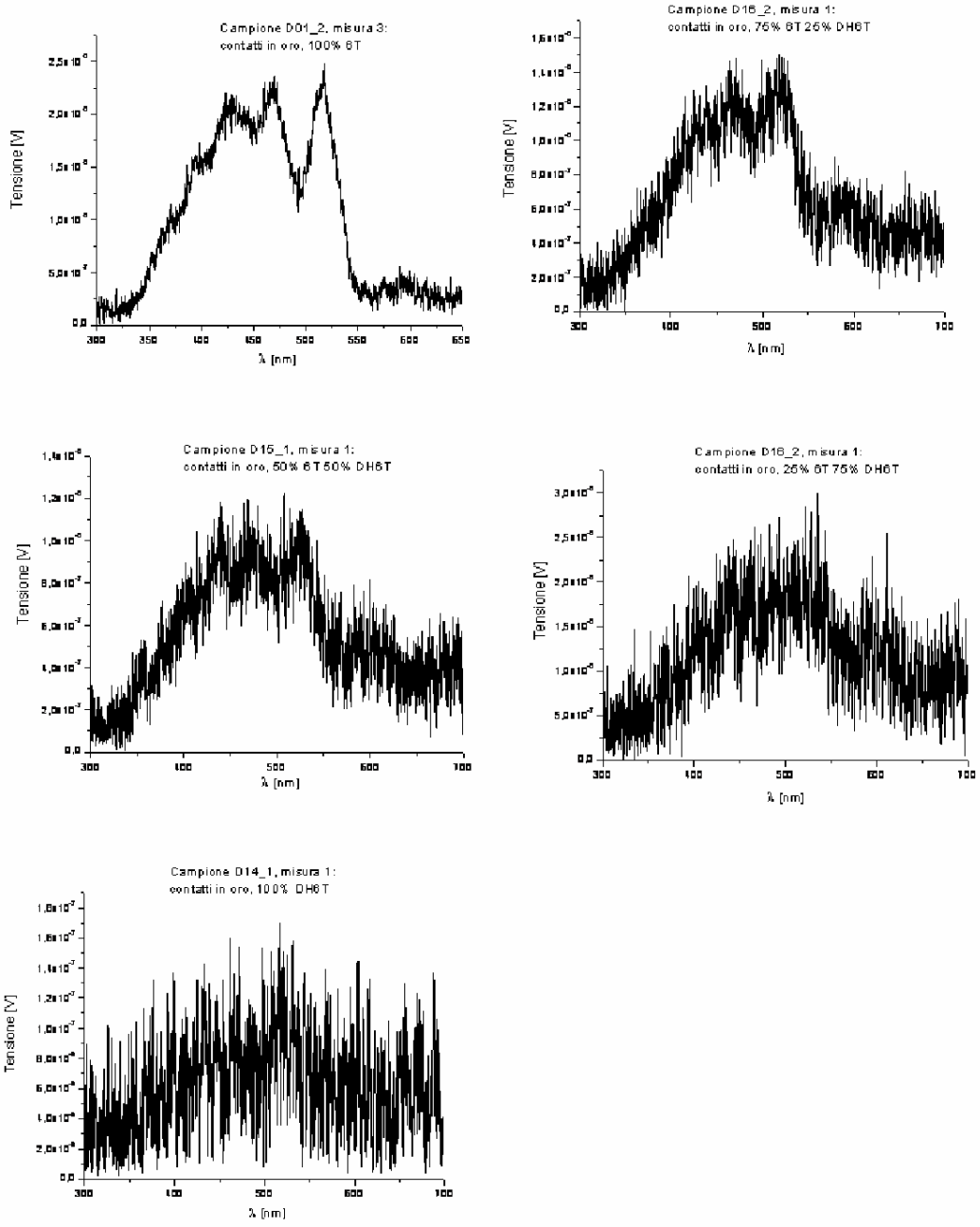

Figure 6.15: A comparison between the photocurrent spectra recorded for all devices.

It is interesting to notice that the relative position of the energy bands is not affected by the presence of the alkyl chains as substituents; we can clearly see 5 different peaks which can be

correlated different energetic transitions. We have compared the recorded spectra with the ones we found in the literature [13, 14].

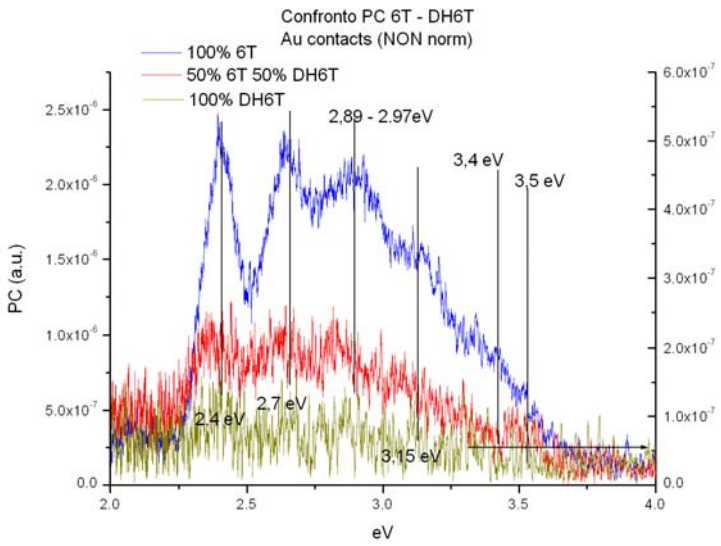

Figure 6.16: A comparison between the photocurrent spectra recorded for all devices.

In Figure 6.17 we show the spectra obtained for the materials we employed in our study, whereas in Figure 6.17 we show the absorption spectrum of β,β'-DH6T (with alkyl chains in β,β' instead of α,ω). As can be seen, no significant difference can be noticed in the reported spectra, and all the recorded peaks seems to be almost in the same positions. What it is interesting is a difference in the relative intensity of the reported peaks compared to the one we obtained. This can be due to the different crystal structure of the investigated films. In α,ω-DH6T molecules are standing almost perpendicular to the substrate whereas in β,β'-DH6T molecules are inclined by 20° angle [14]. These data, therefore, confirm what we previously stated; the presence of alkyl chain substituents does not change the energetic structure (difference between the energetic bands) either if they are use as lateral (β,β'-DH6T) or terminal substituents (α,ω-DH6T).

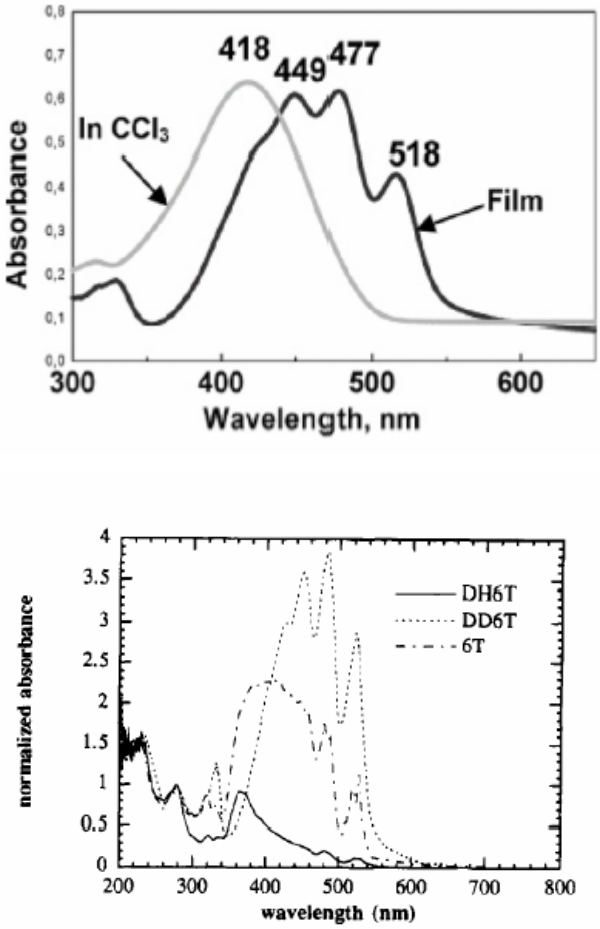

Figure 6.17: Absorption spectra of β,β'-DH6T in solution and in thin film (upper). Absorption spectra of 6T, α,ω-DH6T, and β,β'-DH6T. [13, 14]

In conclusion, in this chapter we demonstrate that using organic semiconductor heterojunctions is a very powerful method for modulating the electrical performances of OFETs. In particular we showed that employing controlled co-evaporations of two dissimilar materials as 6T and DH6T allowed tuning the threshold voltage of the devices without negatively affecting the other electrical parameters. This is particularly interesting, because 6T and DH6T OFETs usually need very high voltages to be turned in their on state (6T devices are characterised by a threshold voltage ranging from -10 to -20V whereas DH6T ones by very high positive voltages, around +50V). Tuning the

threshold voltage upon co-evaporating the two materials with the appropriate ratios, can, therefore, lead to obtain OFETs working in accumulation and/or in depletion regime with threshold voltages approaching zero. This is even more interesting as we observed that the recorded channel mobility measured seems not to be negatively affected by the co-deposition process, and its value is comparable to the values reported in literature for OFETs fabricated with the same materials in a single layer configuration.

References

[1] P. Peumans, S. Uchida and S. R. Forrest, Nature, 425, 158 (2003).

[2] Christoph Waldauf, Marcus C. Scharber, Pavel Schilinsky, Jens A. Hauch, and Christoph J. Brabec, J. Appl. Phys. 99, 104503 (2006).

[3] H. Hoppe and N. S. Sariciftci, J. Mater. Chem. 16, 45 (2006).

[4] S. Yoo, B. Domercq, and B. Kippelen, Appl. Phys. Lett. 85, 5427 (2004).

[5] V. Shrotriya, Y. Y., G. Li, and Y. Yang, Appl. Phys. Lett. 89, 063505 (2006).

[6] J. Drechsel, B. Männig, F. Kozlowski, M. Pfeiffer, K. Leo, H. Hoppe, Appl. Phys. Lett. 86, 244102 (2005).

[7] R Capelli, F Dinelli, M A Loi, M Murgia, R Zamboni and M Muccini, J. Phys.: Condens. Matter 18, 2127 (2006).

[8] J. Wang, H. Wang, X. Yan, H. Huang, D. Jin, J. Shi, Y. Tang, D. Yan, Adv. Funt. Mater. 16, 824 (2006).

[9] J. W. Shi, H. B. Wang, D. Song, H. K. Tian, Y. H. Geng, D. H. Yan, Adv. Funct. Mater. 17, 397 (2007).

[10] F. Dinelli, R. Capelli, M. A. Loi, M. Murgia, M. Muccini, A. Facchetti, T. J. Marks, Adv. Mater. 18, 1416 (2006).

[11] Duhm, S., H. Glowatzki, J. P. Rabe, N. Koch and R. L. Johnson. Appl. Phys. Lett. 88 203109 (2006).

[12] Facchetti, A., M. Mushroom, H. E. Katz, T.J. Marks, Adv. Mater. 15, 33 (2003).

[13] Kiriy, N., A. Kiriy, V. Bocharova, M. Stamm, S. Richter, M. Plöttner, W.-J. Fischer, F. C. Krebs, I. Senkovska and H.-J. Adler Chem. Mater., 16, 4757 (2004).

[14] Yassar, A., G. Horowitz, P. Valat, V. Wintgens, M. Hmyene, F. Deloffre, P. Srivastava, P. Lang e F. Gamier J. Phys. Chem. 99, 9155 (1995).

Chapter 7

Improving charge injection in organic light emitting transistors using a molecular adhesion layer

Recently a new class of organic optoelectronic devices has attracted a huge attention, namely Organic Light Emitting Transistors (OLETs) [1-8]. These new devices combine the switching functions of a common transistor with the light emission, and, moreover, they are excellent test systems to investigate physical processes such as charge injection, transport and electroluminescence in organic materials.

The first part of this chapter is dedicated to the description of the working principles of OLETs and the description of the examples reported so far in literature. In the second part we introduce a novel technique employed for the realization of an adhesion layer for the patterning of metal Source and Drain electrodes. OFETs as well as OLETs usually employ Au electrodes realized on SiO_2 which acts as gate dielectric. Unfortunately Au adhesion on SiO_2 is very poor; therefore, a thin adhesion layer deposition is required. Typically a thin metal film (e.g. Ti or Cr) is used as adhesion layer before Au deposition. This process introduced a second metal/semiconductor interface along the electrode wall influencing both the growth of the organic film and the

charge injection from the metal electrodes into the channel of the device. To avoid the metallic adhesion layer a low-cost and straightforward approach to promote Au adhesion on SiO_2 can be used, based on a self-assembled monolayer (SAM) of [HS–$(CH_2)_3$–Si–$(OCH_3)_3$], 3-mercaptopropyltrimethoxysilane (MPTMS) [9-12]. MPTMS reacts with the silanols groups at SiO_2 surface via the -OCH_3 functionalities, by formation of Si-O-Si bonds and elimination of CH_3OH. This results in a -SH terminated surface with a chemical affinity for Au, enabling the deposition of very thin Au layers. The presence of the MPTMS layer is of great benefit for device operation since it allows a lower contact resistance with the organic film, resulting in a more efficient carrier injection.

7.1 Organic Light Emitting Transistor (OLET)

Organic Light Emitting Diodes and Organic Field Effect Transistors, have attracted a great interest over these decades for their applications to future plastic optoelectronics devices such as flexible displays or sheet computers etc… OLETs represent a relevant novel opportunity, since it combines in one device both the switching properties of OFETs and the optoelectronic properties of OLEDs. Moreover, it is a very powerful instrument to investigate physical processes such as charge injection, transport, and electroluminescence in organic films, and to overcome some constrains posed by the existing vertically-stacked light-emitting devices. The higher charge carrier mobility for OTFTs, if compared to organic and polymer LEDs (of the order of 10^{-5} cm^2/Vs under dc operation), should result in lower exciton quenching by charge carriers in OLETs than in OLEDs. The three electrodes device structure of OLETs allows, in principle, to better control injection and currents of electrons and holes to minimize unbalanced mobility and enhance exciton density. Furthermore, taking

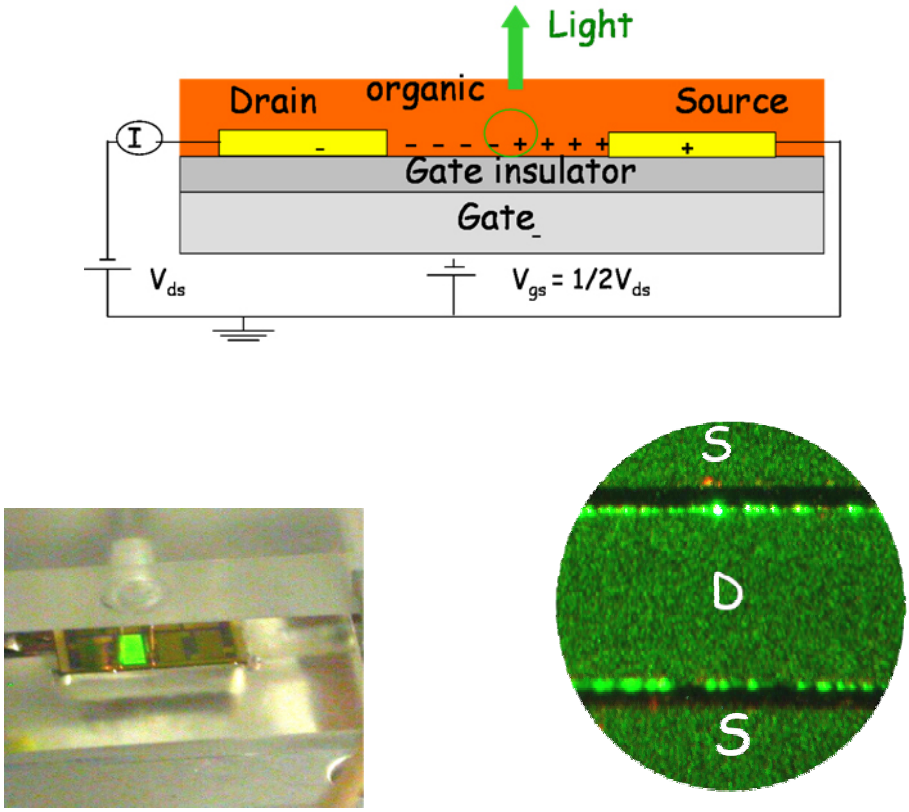

Figure 7.1: Structure of the organic light-emitting transistors fabricated on SiO2/*n*-Si substrates (top). Light is generated by recombination of holes and electrons injected into the transistor channel by source and drain contacts, respectively. Example of a working OLET (bottom).

advantage of the gate electrode bias, the location of the exciton recombination region can be controlled.

7.2 Procedural steps

We realized bottom contact tetracene OLETs employing concentric Au interdigitated source and drain (S/D) electrodes, where a MPTMS SAM is used to promote Au adhesion on SiO_2. A dedicated interdigitated electrode layout was designed, since this geometry is particularly suitable for OLETs characterization as it maximizes the electroluminescence intensity. The concentric geometry allows circumventing parasitic currents due to the unpatterned organic

semiconducting film, [13] enabling an unambiguous interpretation of the (opto-) electronic characteristics, see Figure 7.2 (a). Tetracene has been used for these studies as it is a valid model system for OLETs based on small molecules [1, 2].

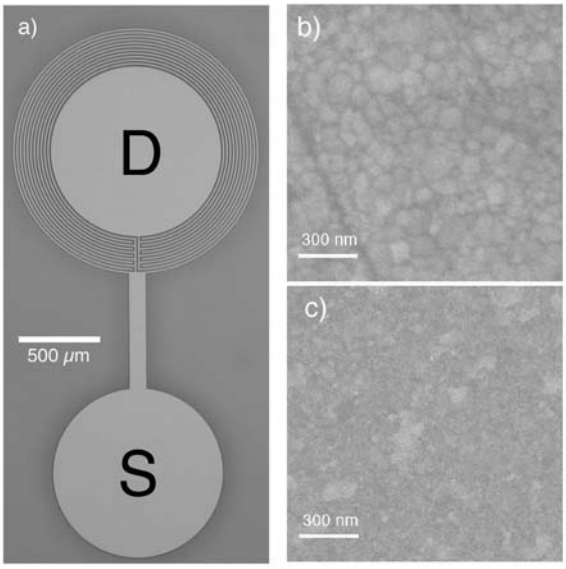

Figure 7.2: Interdigitated concentric Au source and drain (S/D) electrodes with W = 18800 μm and L = 40 μm (a). Two more geometries were used, with, *L*= 6 μm and *W* = 41800 μm and *L*= 10 μm and *W* = 41000 μm. Scanning Electron Microscopy micrographs of Au films on MPTMS (b) and on Cr (c). SEM images were acquired using a JEOL SEM.

Heavily doped (0.01-0.02 μcm) n-Si wafers (gate electrode), covered with a thermal SiO_2 layer (gate dielectric), went through a silylation [14]. The reaction was performed in the gas phase rather than in solution, to achieve a reproducible growth of the SAM [15]. Silylation was followed by deposition (by electron beam evaporation) of a 30 nm-thick Au film and definition of the S/D by photolithography. For comparison, we fabricated standard substrates using the same layout. In this case the wafers went through the deposition of a 6 nm-thick Cr layer, followed by a 55 nm-thick Au film. This high Au thickness was required to avoid the problem of Cr diffusion in the Au film occurring during the 30' annealing in N_2 at 190°C performed to stabilize the Au/Cr contact.

Chemical wet etching was performed using a solution of $Na_2S_2O_3$, $CS(NH_2)_2$ and $K_3[Fe(CN)_6]$ for Au and a solution of $(NH_4)_2Ce(NO_3)_6$ and acetic acid for Cr. Prior to organic film deposition, the substrates were cleaned by O_2 plasma (100W for 5 minutes), which ensures the removal of residuals MPTMS traces. Tetracene (TCI, 98%) was used as the source material. Tetracene films, with nominal thickness in the range from 30 to 50 nm and deposition rate ranging from 3 to 5 Å/s, were sublimed in high vacuum conditions with the substrate kept at room temperature.

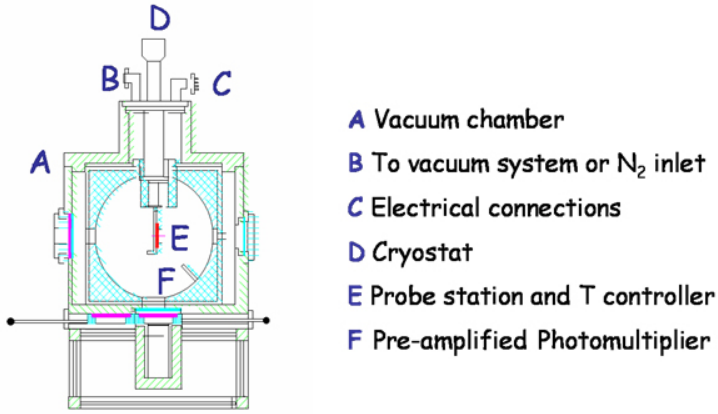

Figure 7.3: Scheme of the integrating sphere for electroluminescence measurements.

OLETs were then placed in a probe station inside a calibrated integrating sphere, where light detection was achieved through a pre-amplified photomultiplier. Simultaneous current and electroluminescence measurements were systematically performed in vacuum at room temperature both in dc and pulsed mode.

7.3 Morphological characterization

As can be clearly noticed both from the SEM and AFM micrographs reported in Figure 7.2 and 7.4 the procedural steps strongly influenced not only the morphological characteristics of the

gold electrodes but also the growth mechanism of the tetracene film both on the channel region and at the top of the electrodes themselves. Figures 7.2 (b) and (c) display Scanning Electron Microscopy (SEM) micrographs of the Au electrodes grown on MPTMS and Cr, respectively. The films have different surface morphologies. On MPTMS, there are Au grains exhibiting an inhomogeneous size distribution. On Cr, Au grains are easily observable and they are typically 100 nm in size. Figures 7.4 (a) and (b) show 6 μm x 6 μm AFM micrographs of tetracene films grown during the same deposition run on substrates employing MPTMS and Cr adhesion layers, respectively. Interestingly, the micrographs show that the two substrates lead to significantly different growth scenarios. In the channel region, the grain size is larger for films deposited on the substrate employing the MPTMS adhesion layer. These films are also more continuous at the electrode interface, with better interconnected grains, probably because of the lower electrode step, see Figure 7.5.

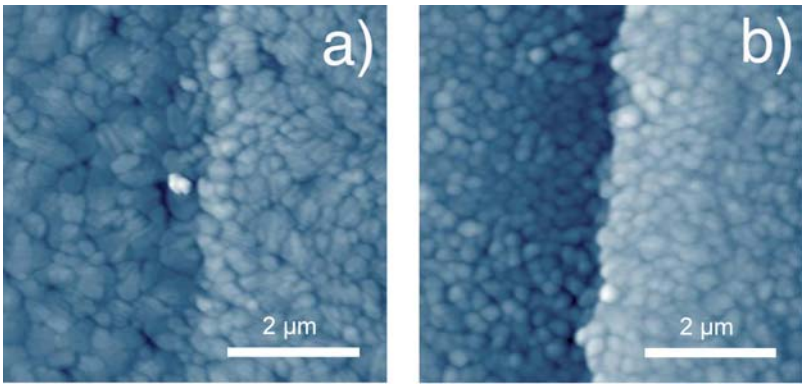

Figure 7.4: 6x6 μm Atomic Force Microscopy micrographs of tetracene active films grown during the same deposition run on substrates employing MPTMS (a) and Cr (b) adhesion layers between source/drain Au electrodes and SiO_2 dielectric. The transistor channel (SiO_2 gate dielectric) and the contact (Au) are shown on the left and right regions of the figure, respectively. The RMS roughness is about 10.5 nm for both films. The images were acquired with a Scanning Probe Microscopy (SPM) Solver Pro Atomic Force Microscopy (AFM) (NT-MDT) in semi-contact mode using NSG-01 Si cantilevers (NT-MDT).

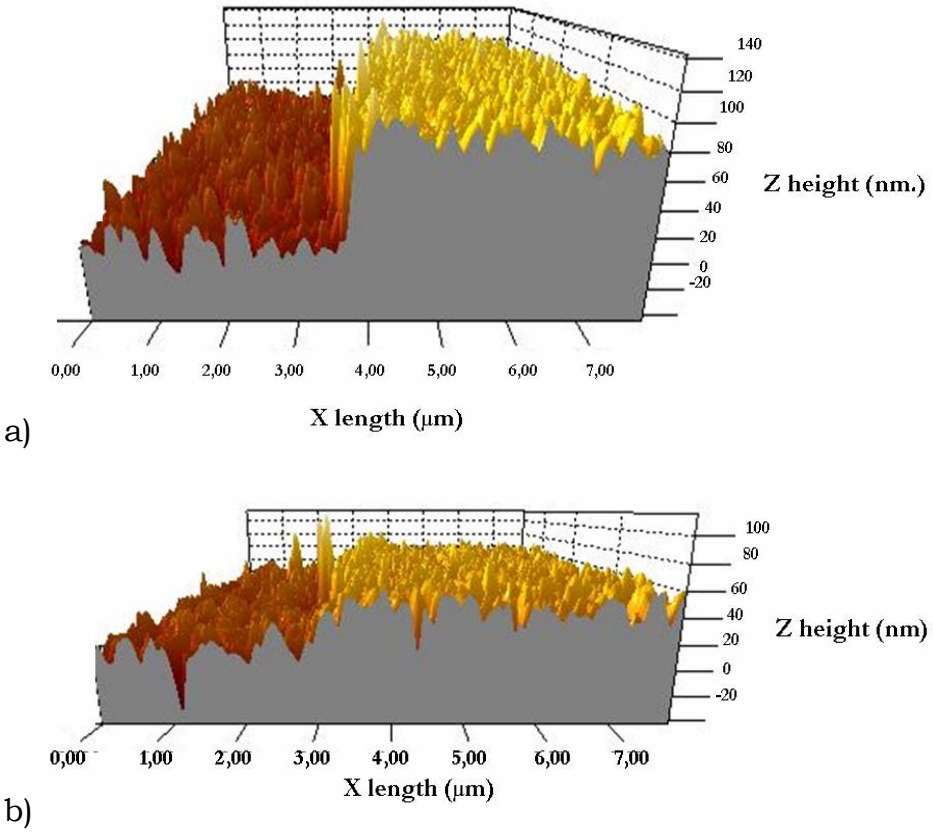

Figure 7.5: AFM 3D micrographs of showing the better interconnection of the tetracene grains at the channel/electrode interface for films grown during the same deposition run on substrates employing Cr (a) and MPTMS (b) adhesion layers between source/drain Au electrodes and SiO_2 dielectric.

Since the micrographs in Figures 7.4 and 7.5 were obtained from films grown during the same deposition run, the different morphologies are related to substrate properties. To go deeper into this aspect, we measured the Root Mean Square (RMS) roughness in the transistor channel region of the two SiO_2 substrates. AFM reveals that substrates employing MPTMS as adhesion layer have a RMS roughness of 0.2 nm whereas substrates employing Cr as adhesion layer have a higher RMS roughness, i.e. 0.6 nm. This last value is attributable to a local redox reaction of Cr on SiO_2 occurring during the annealing. As can be observed from AFM micrographs previously reported, it seems that the

surface roughness of the SiO_2 dielectric strongly influences the morphology of the organic film. Smoother surfaces favour the nucleation of larger islands, leading to films made up of larger grains, as can be seen by the grain area analysis reported in Figure 7.6. Larger domains within the channel would imply a lower number of grain boundaries, possibly acting as charge carrier traps that contribute to lower the hole FET mobility. The larger size of the tetracene grains together with their improved interconnection at the electrode interface should increase the number of charge carriers injected and transported through the transistor channel. This would in turn increase the number of excitons available to emit light after electron-hole recombination.

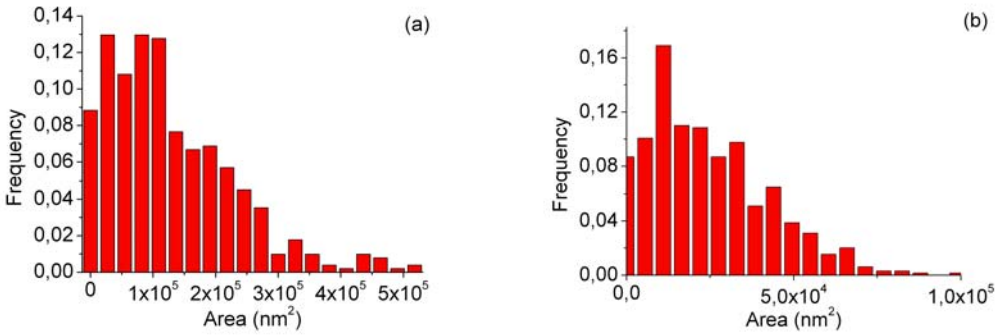

Figure 7.6: grain area distribution for tetracene films grown during the same deposition run on substrates employing MPTMS (a) and Cr (b) adhesion layers between source/drain Au electrodes and SiO_2 dielectric.

7.4 Optoelectronic Characterization

The analysis of the electrical behaviour of the two different kinds of devices show very interesting results. The typical optoelectronic output characteristics are depicted in Figure 7.7. The plots report drain-source current (I_{ds}) and electroluminescence (EL), simultaneously collected, versus drain-source voltage (V_{ds}) at increasing gate-source voltages (V_{gs}). Both devices behaved as p-type transistors working in

accumulation regime. The hole FET mobility, μ, was calculated at the saturation using the following relationship:

$$\left|I_{ds,sat}\right| = \frac{W}{2L}\mu C_i (V_{gs} - V_T)^2 \qquad (7.1)$$

where W and L are the transistor channel width and length respectively, C_i is the dielectric capacitance per unit area ($1.7 \cdot 10^{-8}$ Fcm^{-2} for 190 nm-thick SiO_2) and V_T is the threshold voltage. V_T typically ranges between –7 and –10 V for both devices. The highest μ values observed from several samples, prepared in different deposition runs, were 1×10^{-2} and 10^{-3} cm^2/Vs in LETs employing MPTMS and Cr adhesion layers, respectively, whereas the typical I_{on}/I_{off} (from transfer curves at V_{ds}= -40 V taking I_{off} at V_{gs}= 20 V and I_{on} at V_{gs}= -50V) is around 10^6 for both devices. As a result, the better quality of the organic semiconductor film grown on samples where the MPTMS adhesion layer was used, as described in the previous section, led to optimize charge transport across the channel in order to obtain higher field effect mobility. Moreover, Figures 7.7 (a) and (b) reveal that, under the same bias conditions (V_{ds} = -40 and V_{gs} =-30 V), LETs employing MPTMS give an *EL* signal one order of magnitude more intense than those employing Cr. In addition, with MPTMS, *EL* generation requires lower $|V_{gs}|$ and $|V_{ds}|$ biases (about 10 V). The larger size of the tetracene grains together with their improved interconnection at the electrode interface should increase the number of charge carriers injected and transported through the transistor channel. This would in turn increase the number of excitons available to emit light after electron-hole recombination. This is a plausible explanation of the increased *EL* intensity observed when MPTMS is employed as adhesion layer. The improvement in charge injection from S/D electrodes into the channel for samples realised employing MPTMS is also confirmed by the analysis of the contact

resistance depicted in Figure 7.7 (c). In this case we used the transfer line method in order to estimate the contact resistance for both devices.

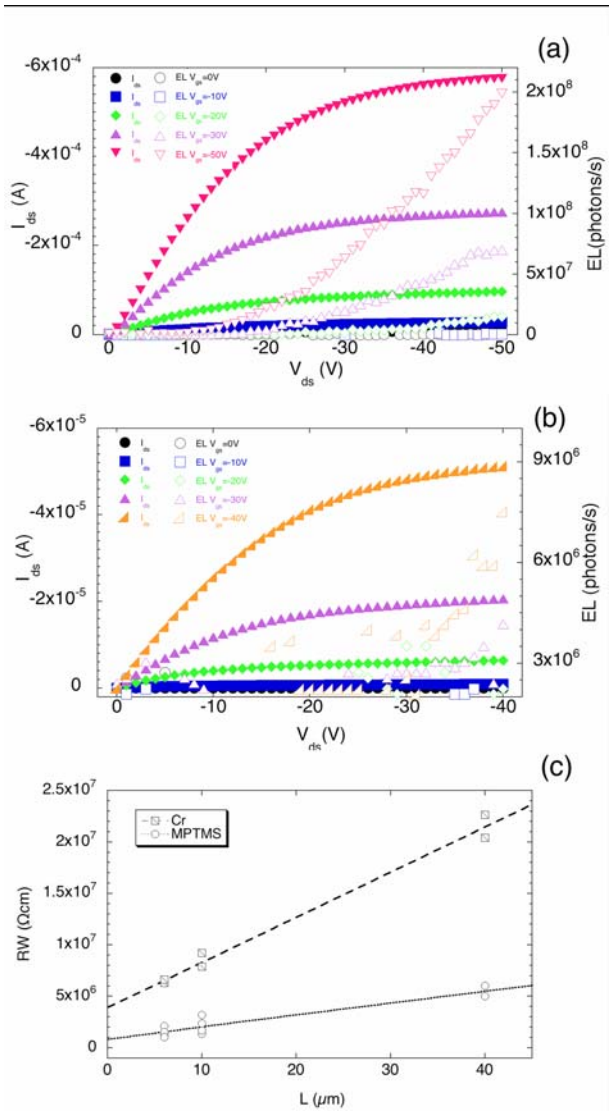

Figure 7.7: Optoelectronic output characteristics of tetracene LETs employing Au/MPTMS (a) and Au/Cr (b) electrodes. Drain-source current (I_{ds}), on the left y axis, and electroluminescence (EL), on the right y axis, vs drain-source voltage (V_{ds}), recorded at increasing gate-source voltages (V_{gs}). W/L = 41800/6 μm/μm. (c) Width normalized device resistance (RW) as a function of the channel length L (at V_{gs}=-40V) for tetracene OLETs fabricated on Au/Cr and Au/MPTMS substrates during the same deposition run. Deposition flux of the active films: 4 Å/s. Nominal thickness: 30 nm.

The graphs depicted in Figure 7.7 (c) reports the width normalized device resistance (*RW*) as a function of the channel length (*L*) for Au/Cr and Au/MPTMS substrates, as deduced from the inverse slope of linear region of the output curves of devices having L=6, 10 and 40 μm. The intercept with the *y* axis for *L*=0 gives the specific contact resistance R_c, which is ≈ 2 MΩcm for Au/Cr and ≈ 0.5 MΩcm for Au/MPTMS. The MPTMS adhesion layer, enabling the minimization of electrodes thickness, reduces the influence of the pre-patterned substrate on the growth of the organic active film, thus leading to better interconnected tetracene grains at the semiconductor/electrode interface. Moreover, the use of the molecular adhesion layer results in a smoother gate dielectric surface leading to increased tetracene grain size. Tetracene LETs employing as adhesion layer a MPTMS SAM exhibit significantly higher hole mobility and electroluminescence intensity and lower contact resistance compared to standard substrates.

In conclusion, in this chapter we demonstrated that the optoelectronic performances in OFETs and in particular in OLETs strongly depend from the triple interface between organic semiconductor/insulator/metal contacts. The use of the molecular adhesion layer results in a smoother gate dielectric surface leading to increased tetracene grain size. Tetracene LETs employing as adhesion layer a MPTMS SAM exhibit significantly higher hole mobility and electroluminescence intensity. Moreover, it led also to a pronounced improvement of charge injection into the channel, resulting in the lowering of contact resistance compared to standard substrates.

References

[1] A. Hepp, H. Heil, W. Weise, M. Ahles, R. Schmechel, and H. von Seggern, Phys. Rev. Lett. 91, 157406 (2003).

[2] C. Rost, S. Karg, W. Riess, M. A. Loi, M. Murgia, and M. Muccini, Appl. Phys. Lett. 85, 1613 (2004).

[3] C. Santato, I. Manunza, A. Bonfiglio, F. Cicoira, P. Cosseddu, R. Zamboni, and M. Muccini, Appl. Phys. Lett. 86, 141106 (2005).

[4] T. Sakanoue, E. Fujiwara, R. Yamada, and H. Tada, Appl. Phys. Lett. 84, 3037 (2004).

[5] T. Oyamada, H. Sasabe, C. Adachi, S. Okuyama, N. Shimoji, and K. Matsushige, Appl. Phys. Lett. 86, 093505 (2005).

[6] F. Cicoira, C. Santato, M. Melucci, L. Favaretto, M. Gazzano, M. Muccini, and G. Barbarella, Adv. Mater. 18, 169 (2006).

[7] J. S. Swensen, C. Soci, and A. J. Heeger, Appl. Phys. Lett. 87, 253511 (2005).

[8] J. Zaumseil, R. H. Friend, and H. Sirringhaus, Nat. Mater. 5, 69 (2006).

[9] C. A. Goss, D. H. Charych, and M. Majda, Anal. Chem. 63, 85 (1991).

[10] I. Doron-Mor, Z. Barkay, N. Filip-Granit, A. Vaskevich, and I. Rubinstein, Chem. Mater. 16, 3476 (2004).

[11] Y.-L. Loo, R. L. Willett, K. W. Baldwin, and J. A. Rogers, J. Am. Chem. Soc. 124, 7654 (2002).

[12] MPTMS reacts with the silanol groups at the SiO2 surface via the –OCH3 functionalities by the formation of Si–O–Si bonds and the elimination of CH3OH. This results in a -SH terminated surface with a chemical affinity for Au, which enables the deposition of very thin Au layers.

[13] E. J. Meijer, C. Detcheverry, P. J. Baesjou, E. van Veenendaal, D. M. de Leeuw, and T. M. Klapwijk, J. Appl. Phys. 93, 4831 (2003).

[14] P. Doppelt, N. Semaltianos, C. Deville Cavellin, J. L. Pastol, and D. Ballutaud, Microelectron. Eng. 76, 113 (2004).

[15] P. Schwartz, F. Schreiber, P. Eisenberg, and G. Scoles, Surf. Sci. 423, 208 (1999).

Conclusions

In conclusion, in this thesis we demonstrated that the electrical and optoelectronic performances of organic semiconductor based devices are strongly influenced on one side by the geometry and architecture of the device itself, on the other hand, by the structural and morphological properties of the employed materials, and that the nanosized interfacial volume between the different materials layers in the device often play a key-role for determining the final properties of the device. In other words, device behaviour is more affected by material boundaries than by intrinsic properties of materials. At the light of the previous considerations, material properties derived from the device measurements must be carefully interpreted.

All Organic FETs assembled with different architectures have been analysed. The better performances obtained for Top Contact devices compared to Bottom contact ones (higher mobility, higher Ion/Ioff current ratios and lower parasitic effects) are clearly correlated to the role played by the triple interface metal/organic semiconductor/gate dielectric in the two different configurations. This was further confirmed by the results we obtained for OLETs, where, modifying the metal electrode/semiconductor interface by using a molecular adhesion layer, it was possible to significantly improve the opto-electronic performances.

The second part of the thesis work is concentrated on the study of organic bulk heterojunctions. It was shown that it is possible to tune the electrical performances of OFETs by using organic bulk heterojunctions, realized employing different organic semiconductor materials and morphologies. We used two different couples of materials: i) α-sexithiophene (6T) and α,ω-dihexylsexithiophene (DH6T); ii) pentacene and C_{60}. Morphology variation was achieved by controlled co-evaporations and double layer depositions of the two dissimilar materials. In the first case we demonstrated that it is possible to

modulate the most meaningful parameters by changing the co-evaporation ratio between 6T and DH6T within the active layer; whereas in the latter we have shown that using pentacene as buffer layer before the C_{60} deposition, it is possible to obtain both unipolar (either p-type or n-type) and ambipolar OFETs, just by controlling the thicknesses of the two deposited layers. These findings demonstrated that bulk hetero-junctions are powerful instruments and open the way for tuning and optimizing the electrical properties in OFETs by means of suitable engineering of materials.